The detection of very high energy cosmic gamma rays using the atmospheric Cerenkov technique

MacRae, John Hamish Kenneth

ABSTRACT

This thesis is concerned with the detection of very high energy cosmic gamma rays using the atmospheric Cerenkov technique. A general introduction to gamma ray detection techniques is followed by a detailed discussion of the principles of the atmospheric Cerenkov technique and the history of its use prior to this work.

The design and operation of the University of Durham facility in Dugway, Utah is described in depth.

Monte Carlo computer simulations have been developed to assist in both the understanding of the equipment and the analysis of the results for the Durham facility. The variation of the response of the array with zenith angle and detector threshold has been investigated and the aperture function of a single telescope calculated. The latter has been found to be a complicated function of both zenith angle and detector threshold.

Computer simulations have also been developed to aid in the design of a camera to record two-dimensional Cerenkov light images from small extensive air showers, and to provide a means of testing analysis routines; these are discussed. The camera is located at the F.L. Whipple Observatory in Arizona.

The techniques employed in the analysis of data recorded by the Dugway facility are discussed, and a computer package developed to aid in the routine aspects of the analysis is described.

Results of observations from two sources, Cygnus X-3 and PSR0531, are presented, with particular reference to periodicities inherent in the sources and to bursts of gamma ray emission. The

discussion of the results includes a review of the various models which have been proposed for Cygnus X-3.

THE DETECTION OF VERY HIGH ENERGY COSMIC GAMMA RAYS USING THE ATMOSPHERIC CERENKOV TECHNIQUE.

by

John Hamish Kenneth MacRae, B.Sc., A.R.C.S.

A thesis submitted to the University of Durham in accordance with the regulations for admittance to the degree of Doctor of Philosophy

Department of Physics
University of Durham

September 1985

for my parents

THE DETECTION OF VERY HIGH ENERGY COSMIC GAMMA RAYS USING THE ATMOSPHERIC CERENKOV TECHNIQUE.

CONTENTS.

PREFACE

The University of Durham Very High Energy Gamma Ray Observatory was established at Dugway, Utah in the Spring and Summer of 1981. The author was involved in the design, construction and commissioning of the equipment during 1980 and 1981, and he took part in the routine operation of the Observatory during three observing periods in 1981 and 1982.

The development and production of the computer simulations obtained for both the Dugway experiment and an independent one at the Whipple Observatory in Arizona, described in Chapters 4 and 5, were entirely the work of the author. He was totally responsible for the analysis of the simulation data obtained for the former, and played a major role in the development of analysis techniques and interpretation of results for the latter.

Along with his colleagues he shared in the analysis of data obtained at Dugway, reported in Chapters 7 and 8, and was wholly responsible for the design and development of the package for routine data analysis described in Chapter 6 and Appendix A. The execution of the routine data analysis on all 1981 and 1982 data was the work of the author.

None of the material contained in this thesis has been submitted previously for admittance to a degree in this or any other university.

CHAPTER 1.

BACKGROUND INFORMATION.

The gamma ray region of the electromagnetic spectrum has been the last to be successfully exploited as a channel for astronomical investigation. This is largely due to the small fluxes and the difficulty of the techniques involved. In recent years, however, there has been a great deal of progress following the availability of space borne detectors, leading to the detection of a diffuse gamma ray background and a number of discrete gamma ray sources.

The main interest in the study of gamma rays lies in the fact that they are produced in high energy particle interactions; the identification of a discrete source of gamma rays is an unambiguous indicator of the presence of very high energy (VHE) particles in the source because of the mechanisms by which they are produced (section 1.2). Identification of sources of cosmic rays (CR) is not possible by direct detection of the CR themselves, since most are charged and are therefore deflected by the magnetic fields permeating interstellar and intergalactic space, thus arriving from directions which bear no relation to those at which they were emitted. Gamma rays arrive undeflected making identification of their source possible.

In this chapter a brief summary of gamma ray detection techniques is followed by a short discussion of the most important production and absorption mechanisms for gamma rays.

1.1 Gamma Ray Detection Techniques.

The techniques used in detecting gamma rays may be divided

into three main categories according to gamma ray energy. The range from 10 MeV to 10 GeV is covered by balloon and satellite observations, while at energies in excess of 100 TeV particle detectors may be used. Finally, between 100 GeV and 100 TeV the atmospheric Cerenkov technique may be used. The first two of these are examined briefly here, the latter being discussed fully in the next chapter.

1.1.1 Lower Energy Observations (10 MeV-10 GeV).

Most of the experimental activity so far has been in this energy region. The predominant interaction of gamma rays with matter at these energies is pair production which has a definite signature, so enabling the particles to be readily identified. The instrument which has achieved greatest success in detecting this signature is the spark chamber. Owing to the fact that gamma rays are absorbed in the atmosphere, which has a thickness of ~30 radiation lengths at these energies, the spark chamber must be operated at balloon or satellite altitudes.

The most successful applications of this technique have been with the SAS-2 and COS-B satellites (Kniffen *et al*, 1977 and Scarsi *et al*, 1977 respectively). These have resulted in the detection of 22 possible discrete sources, 4 of which have so far been identified.

One of the problems with this technique is that as the gamma ray energy increases the angle between the electron-positron pair is reduced, and it becomes increasingly difficult to identify the signature and hence the gamma ray. Also, since the gamma ray is required to interact within the detector itself to be registered, a

large detector area is desirable, and this is not feasible with satellites (for example, the COS-B instrument has a sensitive area of 0.06 m^2); larger detectors may be used in balloons, but the problem then is one of limited exposure time. The Gamma Ray Observatory, due to be launched by NASA in 1988, is the next major experiment in the field of satellite-borne gamma ray detectors. This will incorporate four instruments, and is designed to cover a wide energy range from 30 keV to 30 GeV, but the latter would appear to be the upper limit for the technique in the forseeable future.

1.1.2 Observations Above 100 TeV.

At these energies it is possble to detect, at ground level, the particles produced in the EAS caused by the primary gamma ray. Below ~10 TeV most such secondary particles are absorbed before they reach even mountain altitudes; at sea level the technique is sensitive to energies greater than ~1000 TeV.

Several experiments have been carried out using large detectors at high altitude (Toyoda *et al*, 1965, Catz *et al*, 1970), but no conclusive detection of gamma rays was claimed by the experimenters.

Since gamma rays much above 100 TeV are strongly absorbed in interstellar space by the 3 °K microwave background, as discussed later, interest in this region waned. Recently, however, the detection of Cygnus X-3 at energies in the range 1000-10000 TeV by groups working at Kiel, West Germany, Plateau Rosa, Italy and at Haverah Park, Leeds has caused considerable renewed interest.

1.2 Gamma Ray Production Mechanisms.

Gamma ray production can occur through a wide variety of mechanisms which have been reviewed in detail by Fazio (Fazio, 1967) and Stecker (Stecker, 1971). The general form of mechanism is the interaction of a relativistic electron or nucleon with some other form of matter or magnetic field. In this section the most important mechanisms as far as the atmospheric Cerenkov technique is concerned will be discussed.

1.2.1 Meson Decay.

The collision of a relativistic proton with nuclear matter leads to the excitation of the proton, followed by the emission of π and K mesons. These decay to electrons, neutrinos and gamma rays, with energies which can be as high as 10% of that of the primary nuclei.

1.2.2 Inverse Compton Scattering.

In this process a low energy photon is accelerated to much higher energy by collision with a relativistic electron which in turn loses most of its energy. Since the spectra at radio and optical wavelengths of many active sources can best be explained by synchrotron radiation by relativistic electrons in weak magnetic fields, inverse Compton scattering is a preferred mechanism for producing gamma rays, as both relativistic electrons and low energy photons are clearly present in the source region.

1.2.3 Synchrotron Radiation.

A relativistic electron traversing a magnetic field will

radiate photons, usually at an energy many orders of magnitude below the electron energy. This usually means that gamma rays will not be produced. If, however, the electron energy exceeds $\sim 10^{17}$ eV it is possible for high energy gamma rays to be produced by this process.

1.2.4 Curvature Radiation.

Relativistic electrons following curved magnetic field lines will radiate by the curvature radiation process. The process is only important in the very intense fields found near the surfaces of pulsars ($\sim 10^{12}$ gauss). At very close distances the gamma rays produced can have energies comparable to that of the radiating electron. However, gamma rays produced under these conditions are very likely to be absorbed again, as described in section 1.3.2, so this mechanism is not expected to contribute significantly to the total flux of cosmic gamma rays.

1.3 Gamma Ray Absorption Mechanisms.

The two principal absorption mechanisms affecting gamma rays are by their interactions with low energy photons and in strong magnetic fields; interactions with matter are not important for energies greater than 100 KeV, since the collision cross-section for pair-production with the matter in interstellar and intergalactic space (atomic hydrogen) is negligible. (Obviously, when the gamma ray enters the Earth's atmosphere absorption by pair production takes place, but this is an essential part of the atmospheric Cerenkov technique, with the atmosphere being in effect part of the detector.)

1.3.1 Absorption by Photons.

Absorption of gamma rays by intergalactic star light is only important over extreme extragalactic distances. Absorption by the 3 ^{o}K microwave background, however, has been shown to be important even within the galaxy (Gould and Schreder, 1966, and Jelley, 1966) and has the greatest effect over the range 10^{14}-10^{17} eV. This was considered until recently to effectively impose a cut-off at 10^{14} eV for most sources, except those within ~10 kpc; the detection of Cygnus X-3 (at least 10 kpc distant) at energies greater than ~10^{15} eV has caused this view to be modified.

1.3.2 Absorption in Magnetic Fields.

Pair production by gamma rays in the presence of strong magnetic fields has been discussed by Erber (Erber, 1966) and Ogelman (Ogelman *et al*, 1976). The strong magnetic fields near the surfaces of neutron stars (~10^{12} gauss) make absorption of gamma rays by pair production very likely; they must be therefore be produced far removed from the surface of such stars to survive and be observable.

1.4 The Scope of the Present Work.

This thesis is mainly concerned with the description of the University of Durham Observatory in Dugway, Utah established for the detection of VHE cosmic gamma rays using the atmospheric Cerenkov technique. The theoretical background of this technique, together with a survey of previous work in the field, is given in Chapter 2, while the current experiment is described in detail in Chapter 3.

In Chapter 4 a report is made of the Monte Carlo computer simulations which have been carried out to aid the understanding of the response of this experiment. These have been useful both in experimental design and data analysis, and the results are both interesting and, in some respects, unexpected. Similar calculations were made for the response of the experiment involving the imaging technique being conducted at the Fred Whipple Observatory (FWO), Mount Hopkins, Arizona, and these are described in Chapter 5.

In Chapter 6 the analysis routines developed for the Dugway experiment are discussed, and a software package designed to handle the routine data analysis is described.

Measurements over three seasons of observation have been made on ten sources. These include Cygnus X-3 and the Crab pulsar (PSR0531), and results of measurements of these two sources are reported in Chapter 7, with a discussion following in Chapter 8.

Finally, in Chapter 9, the possibilities for future work in the field are reviewed, particularly with regard to the new and improved telescope currently being built at Durham.

CHAPTER 2.

THE DETECTION OF COSMIC GAMMA RAYS USING THE ATMOSPHERIC CERENKOV TECHNIQUE.

The atmospheric Cerenkov technique for gamma ray astronomy depends on the detection of Cerenkov light produced by the cascade of charged particles, mainly electrons and positrons, initiated by a primary high energy gamma ray entering the atmosphere. This chapter deals with the nature of Cerenkov radiation and its production in gamma ray initiated showers, and discusses previous experiments using this technique.

As mentioned in the previous chapter, the technique is most efficient in the energy range 100 GeV-100 TeV, and thus fills the gap between low energy gamma ray astronomy (10 MeV-10 GeV) covered by ballon and satellite experiments, and observations at higher energies (>100 TeV) where ground-based particle detectors may be used. It has the advantage over the techniques used at lower energies that the effective collecting area is that of the pool of light on the ground rather than the dimensions of the detector itself, a factor which can be 1000 or more at energies around 1000 GeV.

2.1 The Cerenkov Effect.

The production of coherent radiation by the passage of a relativistic charged particle through a dense medium (of refractive index η) was first detected by Cerenkov in 1934 (Cerenkov, 1934). A satisfactory explanation of the effect, based on classical electromagnetic theory, was provided by Frank and Tamm three years

later (Frank and Tamm, 1937). They suggested that the passage of such a particle causes local, transient polarisation of the medium. If the velocity (v) of the particle is greater than the phase velocity of light in the medium (c/η) the the depolarisation of the medium following the passage of the particle results in the emission of a cone of coherent radiation centred about the particle track, as shown in Figure 2.1.

A relation for the cone angle (α) may be obtained using a simple Huygen's construction (from Jelley, 1958) as illustrated in Figure 2.2 (a one-dimensional representation has been used for clarity). From this it may be seen that the Cerenkov radiation is only observed at one angle (α) to the particle track (AB), this being the angle at which the wavelets emitted from arbitrary points P_1 to P_3 along the track interfere coherently to form a plane wave front (BC); the wavelets are coherent when the time taken for the particle to traverse AB is the same as that taken for the light to travel from A to C.

The distance AB, traversed by a particle moving with velocity v in a time interval t is given by the equation

$$AB = vt \tag{2.1}$$

At the same time the light emitted at A travels a distance AC given by

$$AC = \frac{ct}{\eta} \tag{2.2}$$

From equations (2.1) and (2.2) the Cerenkov relation may be

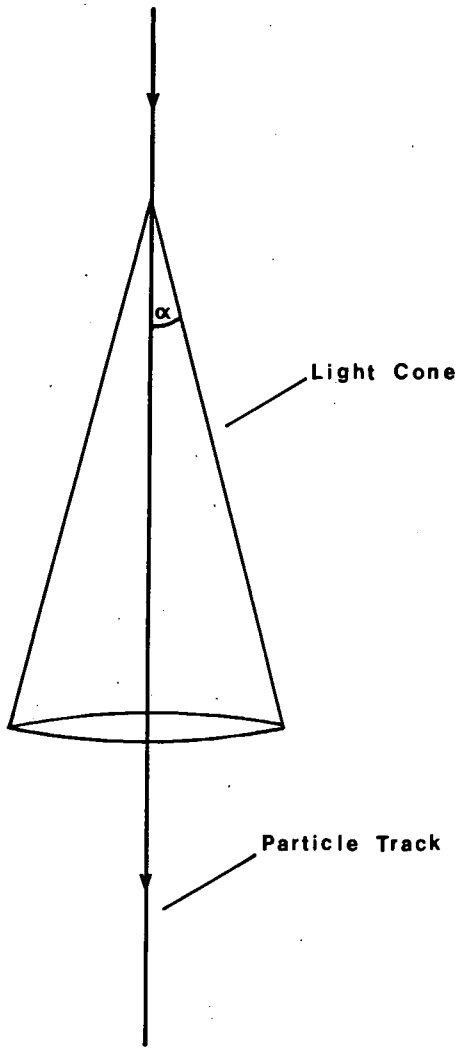

Figure 2.1 The Formation of the Čerenkov Light Cone.

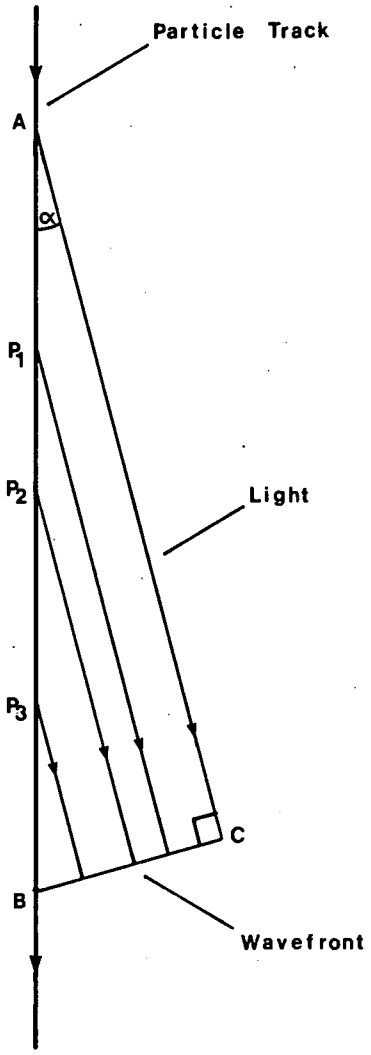

Figure 2.2 Huygen's Construction to Illustrate Formation of Coherent Čerenkov Light Wavefront at Angle α to Particle Track.

obtained:

$$\cos(\alpha) = \frac{c}{\eta v} \qquad (2.3)$$

From equation (2.3) the following conclusions may be drawn:

1. For any medium there is a threshold velocity (v_t) for the charged particle below which no emission takes place:

$$v_t = \frac{c}{\eta} \qquad (2.4)$$

At this critical velocity the radiation is emitted along the direction of the particle track.

2. There is a maximum angle (α_{max}) at which Cerenkov light may be emitted:

$$\alpha_{max} = \cos^{-1}(1/\eta) \qquad (2.5)$$

3. The emission occurs mainly in the visible and near-visible regions of the spectrum for which $\eta > 1$. Thus emission is not possible in the X-ray region for example since η is then less than unity and equation (2.3) cannot be satisfied.

2.2 The Discovery of Cerenkov Light from the Night Sky.

Blackett first suggested in 1948 (Blackett, 1948) that Cerenkov radiation emitted by individual cosmic rays of the CR beam

ought to contribute a small fraction ($\sim 10^{-4}$) of the total brightness of the night sky. There was, however, no way of detecting this effect, since the contribution was so small.

About five years later it occurred to Galbraith and Jelley that there was a real possibility of extensive air showers (EAS) producing measurable pulses of Cerenkov radiation because of the large number of particles involved, and the short time-scale ($\sim$10 ns) over which they were produced.

In order to pursue this idea they devised a simple experiment. A 25 cm f/0.5 parabolic mirror was mounted at the bottom of a dustbin, and a photomultiplier positioned with its photocathode at the focus of the mirror. Coupling this to the fastest amplifier then available (0.03 μs rise-time) they were able to make the first observations of Cerenkov light from the night sky (Galbraith and Jelley, 1953).

Before going into the history of the technique's use in gamma ray astronomy the processes involved in the development of the EAS will be discussed.

2.3 The Development of a Gamma Ray Initiated Electron-Photon Cascade.

When a primary high energy gamma ray enters the atmosphere, an EAS is generated. This is initiated by pair-production, and the growth of the shower takes place via successive steps of Bremsstrahlung and further pair-production. The shower develops to a maximum, and then dies away as the energy is expended.

The lateral growth of the shower is mainly due to Coulomb scattering of the electrons and their deflection in the Earth's

geomagnetic field.

In this section these processes are discussed, and the development of a typical 1000 GeV shower is described.

2.3.1 Bremsstrahlung.

The result of the interaction between an electron and an atom depends on the distance of closest approach (R) of the electron to the atomic nucleus. If R is larger than atomic dimensions then the atom as a whole reacts to the field of the passing electron resulting in its excitation or ionization. When R is of the order of atomic dimensions the problem becomes one of a collision between the incident electron and an atomic electron. At values of R less than atomic dimensions the interaction results in the emission of Bremsstrahlung.

The differential radiation probability for electrons in air is plotted against E'/E in Figure 2.3 (from Rossi and Greisen, 1941).

2.3.2 Pair-Production.

As with electron-atom interactions, photon-atom interactions may be divided into three cases. The interaction of the photon with the atom as a whole is known as the photo-electric effect, the interaction of the photon with an atomic electron, which may be regarded as free, results in the Compton effect, and the interaction of the photon with the nucleus results in pair-production. Since the rest energy of an electron or positron is 0.51 MeV, the photon must have energy of at least 1.02 MeV to create a pair.

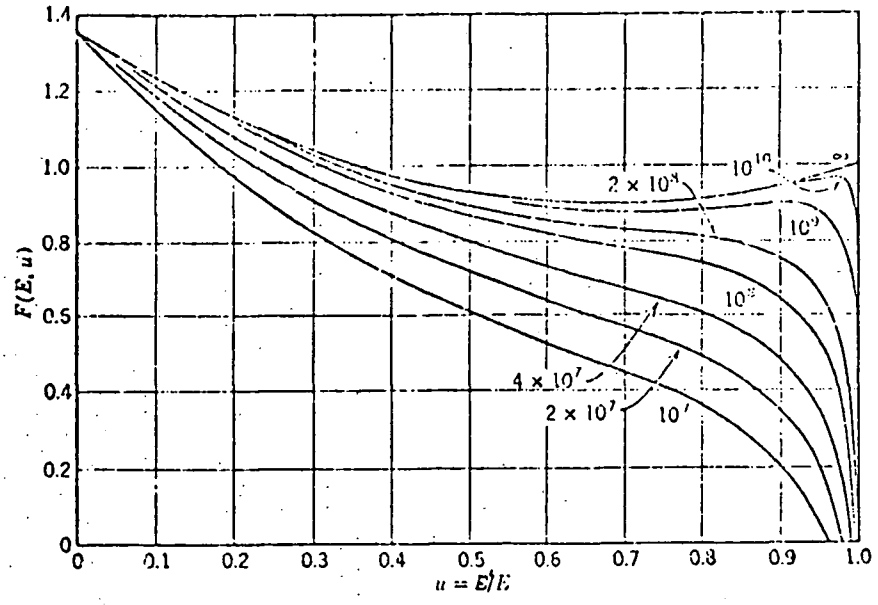

Figure 2.3 Differential Radiation Probability per Radiation Length of Air for Electrons of Various Energies (the numbers attached to the curves are the electron energies (eV)): from Rossi and Greisen, 1941.

In Figure 2.4, the differential probability of pair-production per radiation length of air for photons of various energies is plotted against E'/E, the ratio of positron energy to electron energy (*ibid.*); the process is symmetrical with respect to the interchange of E' and E.

2.3.3 Coulomb Scattering.

The principal dispersive process involved in shower development is the Coulomb scattering of cascade electrons by air nuclei.

From Rossi and Greisen (Rossi and Greisen, 1941) the mean square angle of scatter for relativistic particles with momentum p is given by the relation

$$\langle \alpha^2 \rangle = \frac{E_s^2 t}{p^2 \beta^2} \quad \text{radians} \tag{2.6}$$

where t is the path length measured in units of the radiation length, X_o (which has the value of 37.7 gcm^{-2} in air), and E_s is a constant (21 MeV), which is independent of particle mass and the nature of the medium. For typical cascade electrons, $p \sim E$, the electron energy, and $\beta \sim 1$. Hence over a single radiation length, equation (2.6) leads to

$$\langle \alpha \rangle_{rms} \sim \frac{21}{E} \quad \text{radians} \tag{2.7}$$

when E is in MeV. Thus for a typical cascade electron, with $E \sim 100$ MeV, the r.m.s. scattering angle is about 12°. As will be seen in

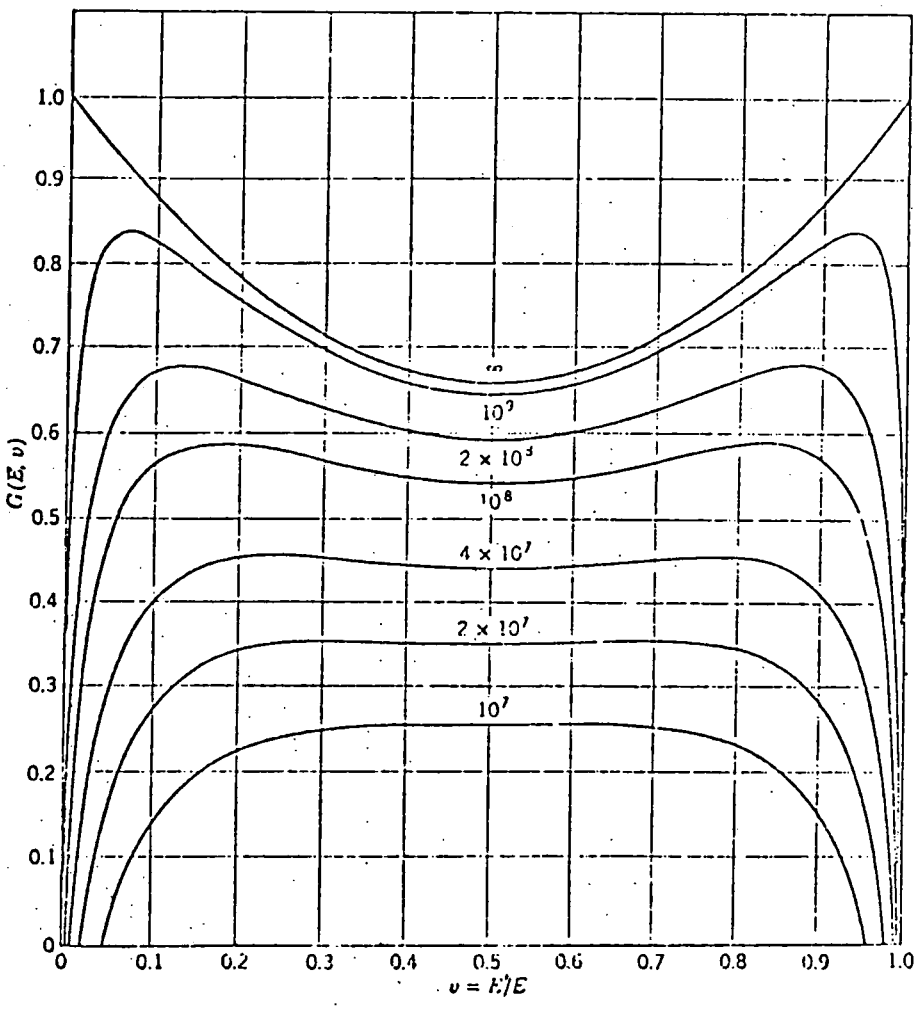

Figure 2.4 Differential Probability of Pair Production per Radiation Length of Air for Photons of Various Energies (the numbers attached to the curves are the energies (eV) of primary photons): from Rossi and Greisen, 1941.

section 2.4.2, this is an order of magnitude larger than the Cerenkov cone angle.

In Figure 2.5, a comparison is made between the Coulomb scattering angle (using equation 2.7) and the Cerenkov cone angle, as a function of electron energy. From this it can be seen that even at very high electron energies (> 100 MeV) the scattering angles are frequently of the same order or larger than the Cerenkov angle. Thus, many of the features of the Cerenkov radiation are masked by the effects of Coulomb scattering.

2.3.4 The Effect of the Earth's Geomagnetic Field.

The effect of broadening of EAS due to the deflection of cascade electrons by the Earth's geomagnetic field was first noted by Cocconi (Cocconi, 1954). This process is not significant at sea level, but at heights greater than 10-15 km it dominates over Coulomb scattering under suitable geometric conditions, as pointed out by Greisen (Greisen, 1956).

The results of incorporating the effects of the Earth's geomagnetic field in detailed calculations were first reported by Browning and Turver (Browning and Turver, 1977). They calculated the lateral distribution of Cerenkov radiation from 100 GeV gamma ray initiated showers, injected vertically, and observed using a detector with an opening (full) angle of 1°. In the case of the geomagnetic field being applied the light pool was found to be approximately 10% larger than with no field, with correspondingly lower peak photon density.

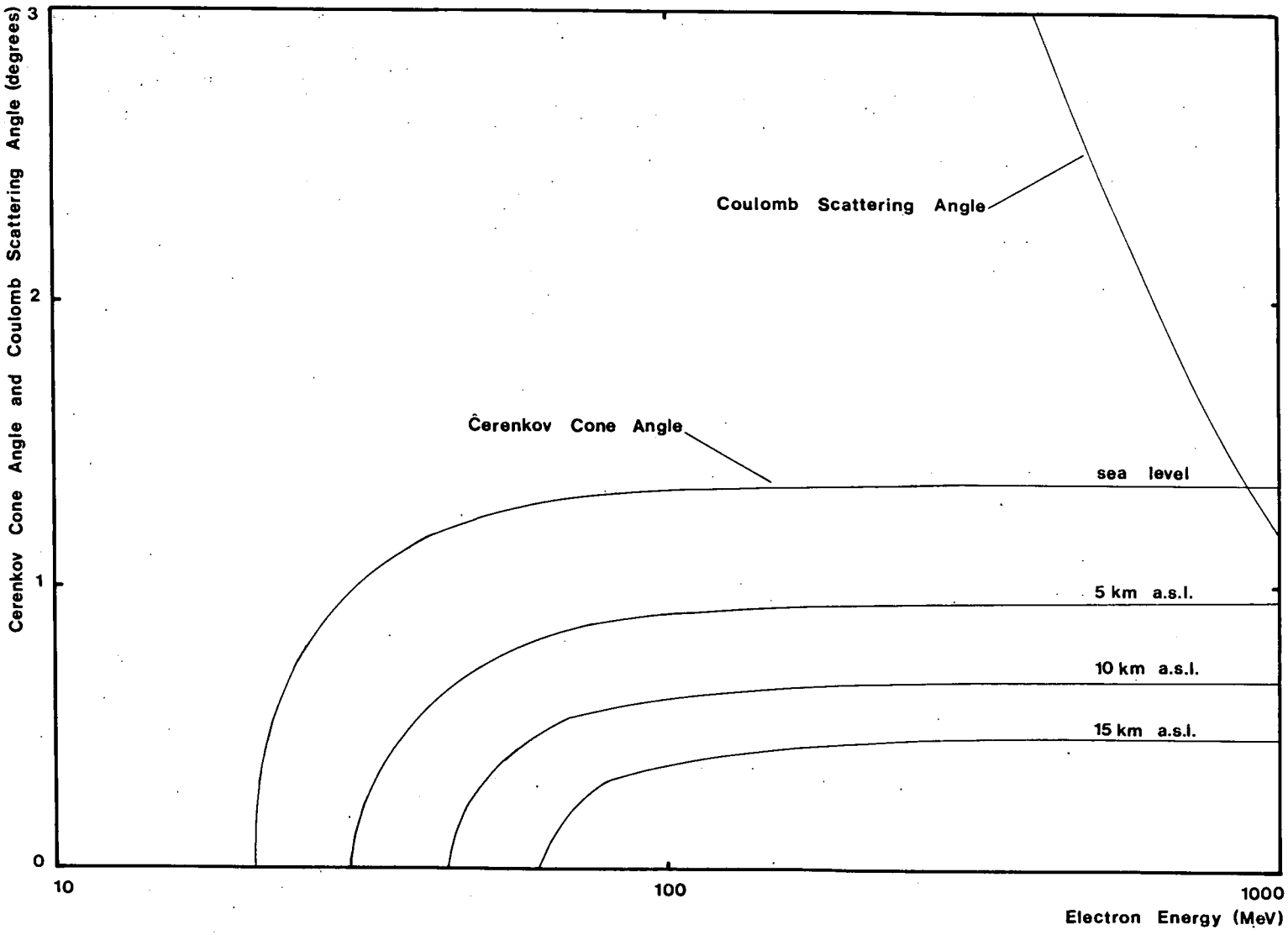

Figure 2.5 Comparison of Cerenkov and Coulomb Effects on Angular Distribution of Light.

2.3.5 A Typical 1000 GeV Shower.

A representation, in one dimension, of a gamma ray initiated shower is presented in Figure 2.6 (from Longair, 1981). In this simple model it is assumed that the electron-positron pairs share the available energy equally, and that over each radiation length each of these particles loses half its energy in radiating one Bremsstrahlung photon. Thus the number of cascade particles doubles after each radiation length until particle energies are reduced to the point where ionization losses dominate over radiation processes.

Full Monte Carlo simulations (Browning and Turver, 1977) have indicated that for a typical 1000 GeV gamma ray initiated shower, the first interaction is at a depth of about 40 gcm^{-2}, with the shower maximising at around 250 gcm^{-2} (10 km a.s.l.). At the maximum, there are about 1000 electrons.

The Cerenkov light pool produced has a diameter of 100-200 m, with photon densities of typically 30 photons m^{-2}. This pulse passes the observation level in a time less than 5 ns. There are few surviving electrons or photons from the cascade.

2.4 Characteristics of the Cerenkov Radiation Produced by the Cascade.

2.4.1 The Electron Energy Threshold for Emission.

The electron energy threshold for emission, which is a function of altitude, is calculated as follows.

The energy (E) of a particle of rest mass m_o is given by the equation

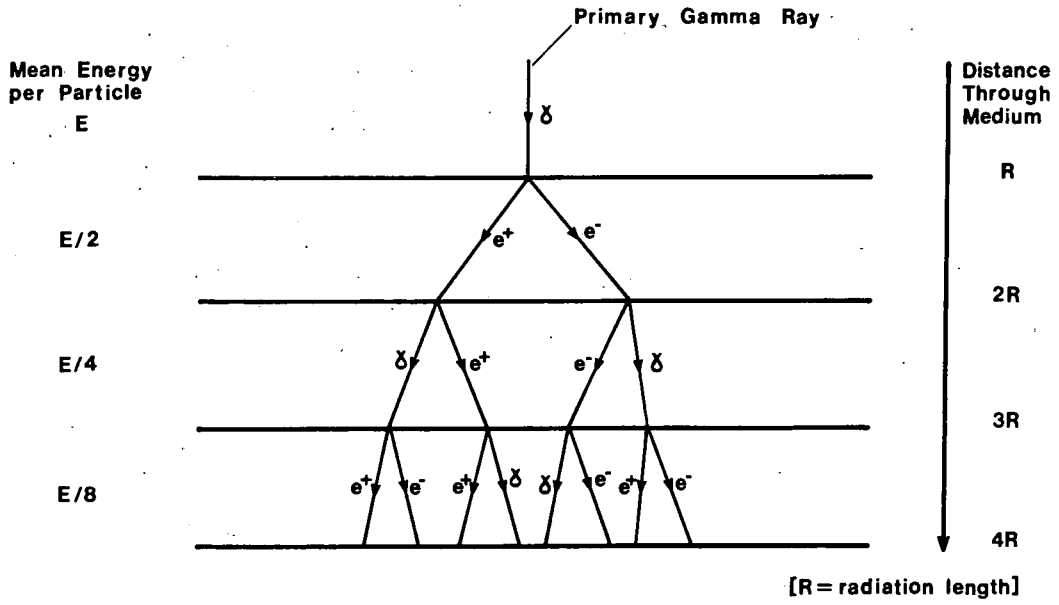

Figure 2.6 Simple Model of Gamma Ray Initiated Cascade.

$$E = m_o c^2 [1 - (v/c)^2]^{-0.5} \qquad (2.8)$$

From equation (2.4), the threshold for emission corresponds to v/c = $1/\eta$. At sea level, η = 1.00029, which for electrons leads to a threshold energy for emission of approximately 21 MeV, rising to about 43 MeV at 10 km a.s.l.

2.4.2 The Cerenkov Cone Angle.

The Cerenkov cone angle (α) is dependent on both particle energy and altitude. The maximum value (α_{max}) is obtained from equation 2.5. Thus at sea level, α_{max} is about 1.3°, reducing to less than 1° at 10 km a.s.l.

Curves relating the Cerenkov cone angle and electron kinetic energy for different altitudes were shown in Figure 2.5. From this the values for the threshold energy and maximum Cerenkov cone angle may also be obtained.

2.4.3 The Size of the Light Pool.

The size of the light pool produced by an EAS, initiated by a gamma ray of a particular energy, is governed primarily by the depth of the maximum of the EAS development. The parameter used here to measure 'size' is based on the lateral distribution of light, being defined as the radius (R_e) at which the photon density has fallen to 1/e of its peak value.

The main processes which determine the value of R_e are the Coulomb and geomagnetic scattering of the particles in a shower, and the emission of light at an angle to the electron/positron tracks. The effect of the last of these alone may be calculated as

follows.

Consider a single ultra-relativistic electron incident vertically at the top of the atmosphere (the effects of the scattering and slowing down of the electron, and the scattering and refraction of light will be neglected for the purposes of this calculation). The light produced at a height h and at Cerenkov angle α (radians), arrives at the observation plane at a distance r from the point of electron impact. For small values of α this leads to the relation

$$r = h\alpha \tag{2.9}$$

Now, for small values of α,

$$\cos(\alpha) = 1 - \frac{\alpha^2}{2} \tag{2.10}$$

The equation for the maximum Cerenkov angle (2.5) may be rearranged to give

$$\cos(\alpha_{max}) = \frac{1}{\eta} \tag{2.11}$$

The refractive index (η) may be written in the form

$$\eta = 1+N \tag{2.12}$$

where $N = N_o e^{(-h/l)}$ ($N_o = 2.9\ 10^{-4}$, and $l = 7.1$ when h is in km).

From equations (2.10)-(2.12) we obtain

$$\alpha_{max} = [2N(1+N)^{-1}]^{0.5}$$

$$\sim (2N)^{0.5} \qquad (2.13)$$

Substituting (2.13) into (2.9) gives

$$r(\alpha_{max}) = h(2N)^{0.5}$$

$$= (2N_o)^{0.5} h e^{(-h/21)} \qquad (2.14)$$

This has its maximum value when h = 21 (= 14.2 km) which leads to a maximum value for r of 126m.

As has been noted previously, however, the effective angular distribution of the light produced in the EAS is governed more by the Coulomb and geomagnetic scattering of the particles in the shower. These effects have been taken into account in detailed computer simulations (Browning and Turver, 1977) the results of which indicate that the maximum radius of the light pool produced by a 1000 GeV gamma ray initiated shower is ~ 400-450 m. However, in practice the effective size of the light pool is much smaller than this when the angular acceptance of the typical gamma ray telescope (~2° FWHM) is taken into account; the calculations above referring, in effect, to detectors of 180° angular acceptance. From the simulations described in Chapter 4, values for the effective radius of the light pool produced by a vertically injected 1000 GeV primary gamma ray range from ~45 m to ~110 m, a typical value being ~100m.

2.4.4 The Rate of Photon Production.

Most of the Cerenkov emission occurs in the wavelength band 350-550 nm, the blue end of the optical spectrum. Although the efficiency of production of Cerenkov light in air is very low, the energy of an optical photon is also low (about 3 eV), so the number of photons produced is high, and it is this which contributes to the success of the technique in giving a worthwhile sample of a penetrating component of the EAS. At sea level the rate of production of light is about 0.3 photons cm^{-1} of path per electron (Jelley, 1958).

2.4.5 The Attenuation of Light in the Atmosphere.

Light is attenuated in the atmosphere at different rates depending on wavelength and altitude. This attenuation is primarily due to Rayleigh scattering, aerosol scattering and ozone absorption. Rayleigh (molecular) scattering of light depends only on the molecule number density. Scattering by aerosols (small particles, 1-10 μm in size) depends on their size distribution and number density. It is most important near ground level and is a highly fluctuating effect. Ozone absorption is a major factor only at wavelengths less than 290 nm passing through high altitudes, and the effects of other attenuation processes, such as dispersion, diffraction and refraction are negligible.

2.5 The Experimental Technique.

In its simplest form, a gamma ray telescope based on the atmospheric Cerenkov technique consists of a mirror with a photomultiplier tube (PMT) at its focus. The PMT and associated

electronics must be of fast response (rise time < 5 ns), in order to achieve a good signal to noise (S/N) ratio. For the same reason, since sources of VHE gamma rays are expected to produce a light spot in the sky with angular dimensions of about 2°, the angular acceptance of the telescope must be of this order.

The principal disadvantage of the technique is that there is, at present, no reliable way of distinguishing between the light produced by photon initiated showers, and that produced by the very much more frequent nucleon induced ones. Other techniques applied to low energy (100 MeV) gamma ray astronomy use anti-coincidence shields to exclude the latter.

The major requirement, therefore, is to optimise the parameters for the detection of a discrete gamma ray source against the vast background of pulses produced by the primary cosmic ray flux. Fortunately, this background flux is spatially isotropic, whereas it is expected that all high energy gamma ray sources will, in effect, be point sources. In addition, the periodicity of, for example, pulsar sources aids their detection against the random CR background.

A second requirement is that the collection areas and energy thresholds of the detectors be known, in order to determine the absolute value of any detected flux. Here, detailed computer simulations of the detector response are of great value, giving the only method of estimating these important quantities.

2.5.1 Optimising the Design of a Gamma Ray Telescope.

The employment of fast PMTs and a geometrical aperture of ~2° have already been cited as necessary in achieving an acceptable S/N

ratio for a gamma ray telescope. To improve this further, the use of two or more flux collectors in coincidence is required; a telescope operating with a threefold coincidence system all but eliminates the possibility of accidental triggering of the system and allows the use of the lowest energy threshold.

Since the speed of response of a PMT is sensitive to changes in gain, caused by varying sky brightness, some form of servo system is required for stable operation. Usually this is achieved by shining a light source into the PMT and varying its intensity to maintain constant anode current. This topic will be discussed further in Chapter 3 (section 3.5.1) with reference to the University of Durham facility at Dugway.

2.6 Previous Observations Using the Technique.

Work has been carried out in the field of VHE gamma ray astronomy using the ground-based atmospheric Cerenkov technique for more than a decade.

The earliest observations were made around 1970 by groups operating in Malta (from Dublin) and at the Mount Hopkins Observatory (MHO) in Arizona, since renamed the F.L.Whipple Observatory (FWO). Of these two only the latter is still in operation. In 1972 observations commenced at the Crimean Observatory, U.S.S.R., which is still in operation, and at Narrabri, N.S.W., Australia, using the Hanbury-Brown stellar interferometer. Since 1977 measurements have been conducted at the Ootacamund Observatory (OOTY) in India, and in 1981, the year in which the University of Durham facility at Dugway, Utah was established, work began at the Iowa State-Jet Propulsion Laboratory

(JPL) facility at Edwards Air Force Base in California.

The equipment used at these locations is now summarised:

1.FWO: A 10 m reflector and several 1.5 m reflectors have been used in various coincidence modes. The work currently being conducted is a collaboration involving workers from six centres including Durham, the details of which are discussed in Chapter 5.

2.Malta: A Cerenkov detector consisting of four 1 m reflectors operating in coincidence was employed by University College, Dublin until 1975.

3.Crimea: The group here uses an array of four 1.5 m reflectors. Recently a camera of 19 PMTs has replaced the quadruple mirror system. In addition, an array of four reflectors, a duplicate of the original experiment, was established at a high altitude station in 1979.

4.Narrabi: Two 7 m reflectors were operated in coincidence, providing so far the only VHE gamma ray observations from the southern hemisphere.

5.OOTY: Coincidence systems of 0.9 m and 1.5 m reflectors are used in array and compact configurations.

6.JPL: Two 7 m reflectors separated by 25 m were operated in coincidence during short observations in 1980-1981.

2.6.1 Summary of the Main Results.

The sources detected by 1982 at VHE gamma ray wavelengths are the Crab and Vela pulsars, Cygnus X-3, and Centaurus A. The results are summarised in Tables 2.1 to 2.4, taken from a paper by Grindlay (Grindlay, 1982a) who made the point that the energy thresholds and fluxes listed in these tables should be regarded as uncertain.

1. The Crab Pulsar.

Detection of this source, summarised in Table 2.1, has been reported by five different groups. The results exhibit some disagreement, particularly with regard to the time averaged fluxes; a possible explanation for this is offered later in this thesis.

The first extended observations of the Crab Nebula using the atmospheric Cerenkov technique were those of Chudakov (Chudakov *et al*, 1962, 1965) which were carried out in 1960-1961. Using the drift scan technique they found an upper limit of 5.0×10^{-11} photons $cm^{-2}s^{-1}$ for primary gamma rays of 5 TeV or more. Following this, Fruin (Fruin *et al*, 1964) and Long (Long *et al*, 1965) reported observations providing an upper limit of 1.3×10^{-11} photons $cm^{-2}s^{-1}$ for a threshold energy of 2.7 TeV. Measurements were also conducted by Fegan (Fegan *et al*, 1968) and Tornabene and Cusimano (Tornabene and Cusimano, 1968) at this time.

The discovery, in 1968, of the pulsar NP0532 revived interest in high energy gamma rays from the nebula . Following the development of very precise optical measurements of the pulsar (Horowitz *et al*, 1972) it became possible to align runs from successive nights in phase resulting in improved statistics.

Possible positive periodic effects were reported by Grindlay

TABLE 2.1

VHE Gamma Ray Results on Crab Pulsar

Group	Ref. No.	Dates	Effect	E_0(TeV)	Flux (10^{-11} ph/cm^2 sec)	Technique	Comments
MALTA	12	2-3/70	3.5σ	2	0.2	Fast Ann.	Main + Inter; 18 ms. delay
MHO	8	10/69-4/72	—	0.12	<1.7	Single Beam	10m, Tracking
MHO	8	1/71	—	0.8	<0.7	Double Beam	S.L. Drift Scans
MHO	5,8	11-12/71	~3σ	0.8	0.6	Double Beam	Main + Interpulse; -2 ms. delay S.L. Drift Scan
MHO	15	1/72	~4σ	5	0.3	Wide Angle	Interpulse Only
MHO	15	2-3/72	--	5	<0.2	Wide Angle	10m, Tracking
MHO	8	2/73	—	0.8	<0.2	Double Beam	S.L. + 10m, Tracking
MHO	15	2-3/73	—	5	<0.2	Wide Angle	10m, Tracking
MHO	8	12/73	5.2σ	0.8	0.4	Double Beam	Main(?) only; 6 ms. delay S.L. +10m, tracking
MHO	8	1/74	4.3σ	1.8	1.3	3-PM Coinc.	Interpulse(?) only; -2 ms. delay
IOWA	3	3/76	~4σ	20	0.5	Coinc. Sys.	Main; ~15 Ms. Delay
OOTY	10	2/77	3.6σ	6.4	1.2	Coinc. Comp. Array	Main + Inter; uncertain phase
OOTY	11	78	—	3.2	<1	Comp. Array	
OOTY	11	79	—	2	<1	Comp. Array	
OOTY	11	80	—	1.5	<1	Comp. Array	
OOTY	11	2/81(Total)	≳2σ	0.9	<0.5	Dist. Array	
		vs. 2/81(7/16 nts.)	4.3σ	0.9	0.3	Dist. Array	Select Nts. with ≳2σ effect Main + Inter.; uncertain phase
DUGWAY	18	10/81	~5σ(peak)	2	2	Coinc. Array	Transient effect

in observations made in January 1971 (Grindlay, 1971) and in November-December 1971 (Grindlay, 1971, Grindlay *et al*, 1976) using the 10m reflector at MHO, and employing the drift scan technique. More significant results were obtained in 1973, but here the peak of the emission was displaced from the optical peak by 6.5 ms (Grindlay *et al*, 1973, 1974, 1976).

Further positive periodic effects were reported by Jennings (Jennings *at al*, 1974) for observations caried out in Malta in February-March 1970 using the fast annulus technique. Two peaks were observed, separated by the same amount as the optical main and interpulse, but displaced by 18 ms from their expected positions. In addition to the phase offset the events constituting the effect appeared to spread out over a wider angle than that expected from Rieke's theory of the electron-photon showers (Rieke, 1969). The possibility that this might be due to geomagnetic broadening (Porter, 1973) led to an experiment using a wider angle field of view carried out at MHO in 1972 and 1973 (Porter *et al*, 1974, 1976). This resulted in a significant effect for the January 1972 observations with a single pulse at the optical interpulse position, but no effect was found in Febuary 1972 or in 1973.

At the end of 1973 and beginning of 1974 a threefold coincidence arrangement was employed on the MHO 10m reflector resulting in a periodic effect being observed (Weekes and Rieke, 1974, Helmken *et al*, 1975, Grindlay *et al*, 1976). A single peak was found displaced by ~2 ms from the optical interpulse.

Observations at an energy of 6.4 TeV were recorded by the OOTY group which reported the detection of two pulses at the correct optical main-interpulse spacing, but the absence of

absolute phase information precluded the synchronisation of these with optical measurements (Gupta *et al*, 1977). Further observations by this group in 1978-1980 were unsuccessful, but in 1981 a significant result was obtained, with detection once again of two pulses at the appropriate spacing at uncertain phase.

By and large the results of observations on PSR0531+20 are different, and if all were to be accepted the pulsar would be required to be variable in both amplitude and phase. However, the Dugway measurements reported in Chapter 7 may offer some explanation for the apparent discordancy.

2.Vela Pulsar.

The first VHE gamma ray measurements of the Vela pulsar showing signs of a positive effect were made by Grindlay (Grindlay *et al*, 1975b) using the stellar interferometer at Narrabri. In this work a peak was observed 3 ms early with respect to the phase predicted from radio observations. The apparent flux detected in 1972 was $\sim 1.0 \times 10^{-11}$ photons $cm^{-2}s^{-1}$ for an energy threshold of $\sim$0.3 TeV.

Subsequent measurements by the Indian group at Ootacamund have yielded significant results in two out of four observing seasons, with a similar flux to that recorded by Grindlay but for an energy threshold greater by about one order of magnitude.

The results of VHE gamma ray observations of this source, the strongest at 100 MeV energies, are summarised in Table 2.2. The pulses of VHE gamma ray emission from the pulsar appear to be narrow and variable, although further confirmation is needed by new experiments in the southern hemisphere.

TABLE 2.2

VHE Gamma Ray Results on Vela Pulsar

Group	Ref. No.	Dates	Effect	E_o(TeV)	Flux (10^{-11} ph/cm^2 sec)	System	Comments
NARRABRI	7	4-5/72	4.2σ	0.3	1.0	2 x 7m Double Beam	Single narrow pulse; approx. optical phase
NARRABRI	7	4-5/73	—	0.3	<0.8	2 x 7m Double Beam	Upper limit from all data
NARRABRI	7	4-5/73	3σ	5	~0.1	2 x 7m Double Beam	Single narrow pulse for high PHA only; approx. optical phase
NARRABRI	7	4-5/74	—	0.3	<2	2 x 7m Double Beam	Limited exposure time
OOTY	1	1-3/77	—	16	<2	Compact SL Array	
OOTY	11	2-3/79	~4σ	4.5	~1	Compact SL Array	2 peaks separated by 0.4 in phase; no obs. phase
OOTY	11	1-3/80	—	3.4	<1.2	Compact SL Array	
OOTY	11	1-3/81	~4σ	2.3	~1.2	Dist. SL Array	2 peaks separated by 0.4 in phase; no obs. phase

3.Cygnus X-3.

Cygnus X-3 has been the subject of an extensive observing programme by the Crimean group since the radio outburst of 1972. The first observations, in September 1972, resulted in the first detection of VHE (>1000 GeV) gamma rays from this source (Vladimirski *et al*, 1973). The observed effects were restricted to the lower energy channel suggesting a steep energy spectrum.

Subsequent measurements by this group, and those at a different observatory using a duplicate experiment (Mukanov *et al*, 1979) showed the characteristic 4.8 hour periodicity noted in X-ray and IR observations.

There has been evidence for peaks in the emission of VHE gamma rays from Cygnus X-3, occurring at X-ray phases of ~0.1 and ~0.6, with some indication that the relative strengths of the two peaks have altered since the first measurements in 1972. Measurements by Neshpor (Neshpor *et al*, 1980) and Danaher (Danaher *et al*, 1980) suggest that in 1979-1980 the dominant feature of the VHE signal was the interpulse at phase ~0.6 rather than the main pulse previously observed at phase ~0.1.

Cygnus X-3 has now been detected by four groups, a summary of the main results being provided in Table 2.3. The results indicate variable emission of VHE gamma rays at or near phases 0.1 and 0.6 in the 4.8 hour X-ray period. Interpretations of the data suggest a fast, young pulsar as the collapsed object of the X-ray binary system. In this case a pulsed VHE gamma ray signal may be expected with a period shorter than that of the Crab pulsar, but so far this has not been detected.

TABLE 2.3

VHE Gamma Ray Results on Cyg X-3

Group	Ref. No.	Dates	Effect	E_0(TeV)	Flux (10^{-11} ph/cm^2 sec)	System	Comments
CRIMEA	16,17	72	~5σ	1.2	7	Coinc. SL	Single pk. at phase ≃0.1
CRIMEA	16,17	9/73	~3.5σ	1.2	2.4	Coinc. SL	Single pk. at phase ≃0.1
CRIMEA	16,17	8/74	~4.6σ	1.2	6	Coinc. SL	Double pks. at phase ≃0.1, 0.6; sporadic emission
CRIMEA	16,17	75	~4.6σ	1.2	1.5	Coinc. SL	Single pk. at phase ≃0.1
MHO	19	76	---	~0.3	<0.6	10m	Upper limit
CRIMEA	17	76-79	~3.5σ	1.2	1.0	Coinc. SL	Emission at phases ~0.1 and ~0.6
MHO	20	79	---	~0.3	<0.6	10m	Upper limit
MHO	21	5-6/80	≥4σ	~2	~1	Coinc. SL	Emission at phase 0.6-0.7 correl. with X-ray flare
CRIMEA	17	10/80	~3.5σ	1.2	~1	Coinc. SL	Sporadic emission at phase ≃0.6
DUGWAY	18	8-10/81	(~2.5σ)	≃1	~10(?)	Coinc. SL	Single pk. at phase 0.625; low PHA only
MHO	19	9-11/81	~3-4σ	~0.3	<3	10m Low-PHA	Φ=0.6-0.7; Φ~0.8 Flare
JPL	13	9/81	~4σ	~1	~1	2 x 7m Coinc.	Φ=0.5-0.7
MHO	21	6/82	---	~1	<1	10m - 7PMT camera	Upper limit
DUGWAY	18	6-8/82	~3-4σ	~1	?	Coinc. SL	Positive effect at 4.8 hr phase ≃0.62 and near maximum of 34 day phase.

4.Centaurus A.

The detection by Grindlay (Grindlay, 1975a) of the nearby radiogalaxy, Centaurus A, using the Narrabri stellar interferometer, provided the first evidence of extragalactic gamma rays. A flux of 2.0×10^{-10} $cm^{-2}s^{-1}$ was measured and interpreted by Grindlay as emission from the Compton synchrotron process in the compact galactic nucleus.

So far these measurements (Table 2.4), which were made a decade ago, constitute the only detection of this source.

TABLE 2.4

VHE Gamma Ray Results on Cen A

Group	Ref. No.	Dates	Effect	E_o(TeV)	Flux (10^{-11} ph/cm^2 sec)	System	Comments
NARRABRI	6	3-5/72	4σ	0.3	~4	2 x 7m Double beam	X-ray High
NARRABRI	6	3-4/73	1σ	0.3	<4	2 x 7m Double beam	X-ray Low
NARRABRI	6	3-5/74	3σ	0.3	~4	2 x 7m Double beam	X-ray High
NARRABRI	6	72-74	4.6σ	0.3	~4	2 x 7m Double beam	Average of all data

CHAPTER 3.

THE UNIVERSITY OF DURHAM GAMMA RAY FACILITY AT DUGWAY.

The University of Durham facility for high energy gamma ray astronomy was established at Dugway Proving Grounds, Utah (40.2° N, 112.82° W), during the Spring and Summer of 1981. This is a United States Army base and test area located at a desert site about 80 miles south-west of Salt Lake City.

The facility comprises an array of four Cerenkov light detectors arranged at the apices and centre of an equilateral triangle of side 100 m (Figure 3.1 and Plate 1).

Each detector, or telescope, consists of three paraxial, parabolic mirrors mounted on an alt-azimuth platform, with a fast PMT at the Cassegrain focus of each mirror (Plate 2). This use of three flux-collectors, with the requirement for a threefold coincidence between them for a detection of the light flash, provides an almost accidental-free detection of a local Cerenkov signal. Each telescope, is equipped with a paraxial low light CCTV camera capable of detecting sixth magnitude stars to provide continuous images of the field under study.

A caravan near the centre of the array houses the supervising Tektronix 4051 computer (TEK 4051) and most of the microprocessors and electronics employed to steer the detectors and record the data.

3.1 The Choice of Site.

The Dugway site was chosen for a number of reasons:-

1. The desert climate is dry, with moderate rainfall,

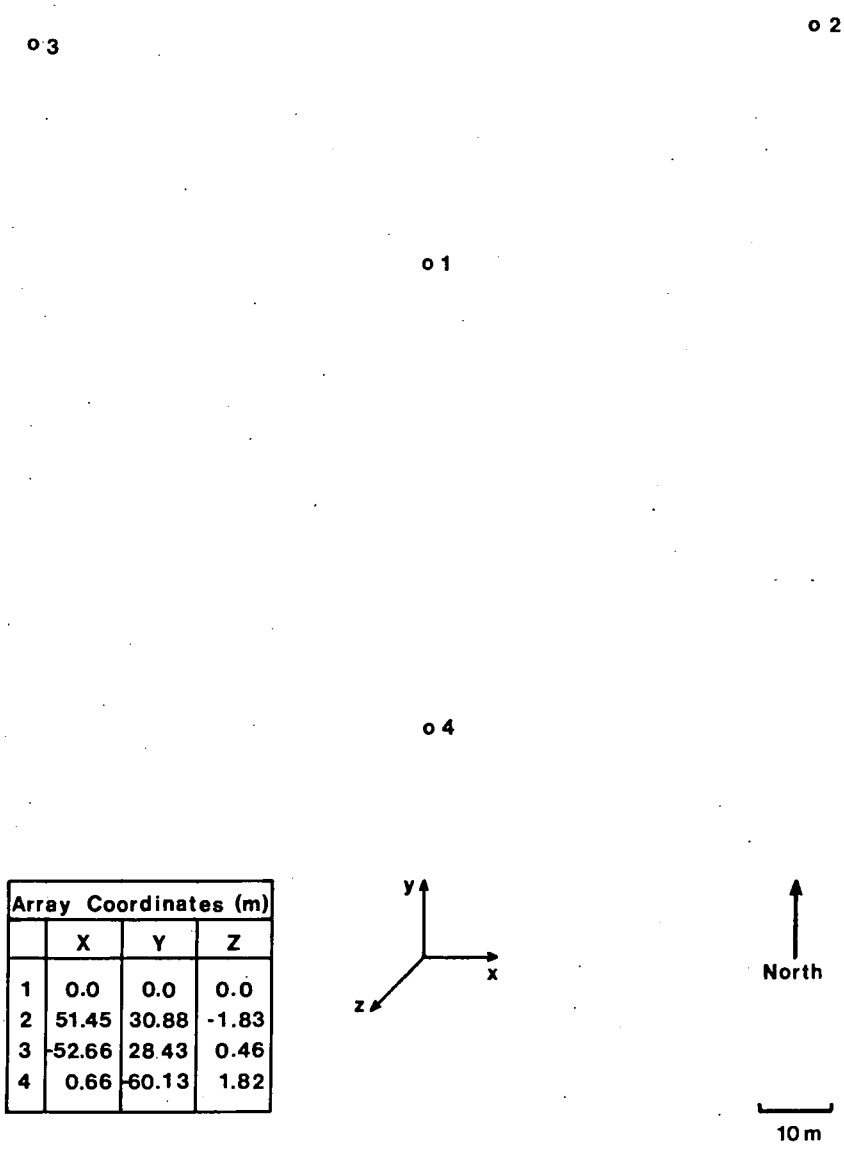

Array Coordinates (m)			
	X	Y	Z
1	0.0	0.0	0.0
2	51.45	30.88	-1.83
3	-52.66	28.43	0.46
4	0.66	-60.13	1.82

Figure 3.1 The Dugway Array.

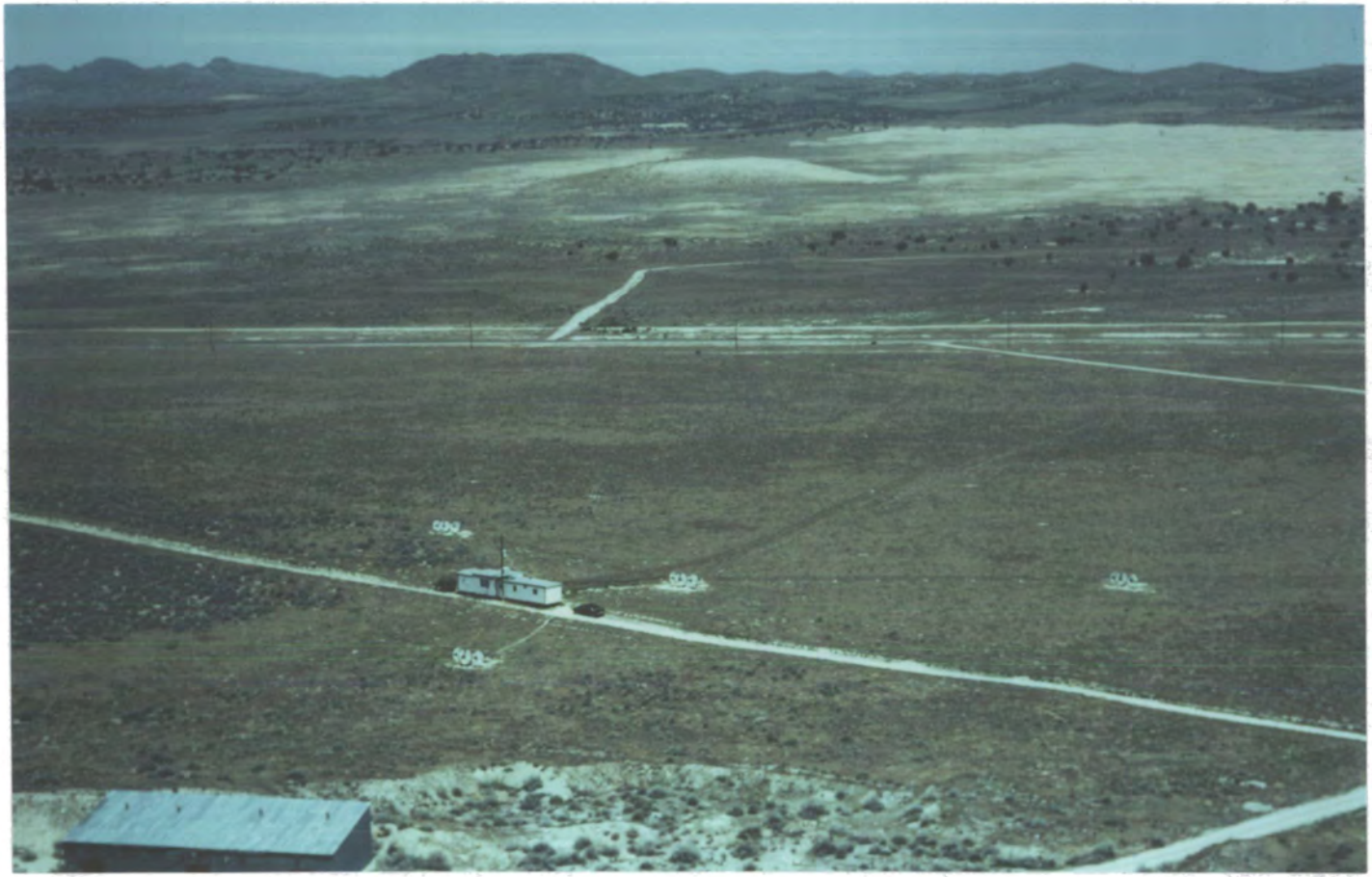

Plate 1.

Plate 2.

resulting in many clear, cloudless nights especially during the months from June to November.

2. The site is ideally situated in latitude for the study of those high energy gamma ray source candidates which were of initial interest to us, such as the Crab pulsar and Cygnus X-3, which culminate at or near the zenith.

3. The logistic support given by the personnel on the Base was very helpful during the operation of an earlier cosmic ray experiment between 1977 and 1980, and has continued to be so.

3.2 The Site Characteristics.

3.2.1 The Climate.

The Utah desert climate is quite well suited to the purpose of the experiment. However, the annual temperature variations, illustrated in Figure 3.2, are large. The months when problems arise are November to February, when the extremely low temperatures (-20°C) make operation of mechanical components difficult. The facility is not normally operated during this period, which coincides with periods of substantial cloud cover.

Annual rainfall is moderate, occurring evenly throughout the year, the only significant source of inteference with observation in the June-November period being the thunderstorms which occur mainly in July and August. The long runs of signal cable above ground present a prime target for lightning strikes, and strict measures are taken to ensure the isolation of the electronics in the event of a local storm. Nevertheless there have been two instances of substantial lightning-induced damage. There are on average six local thunderstorms during these two months in each

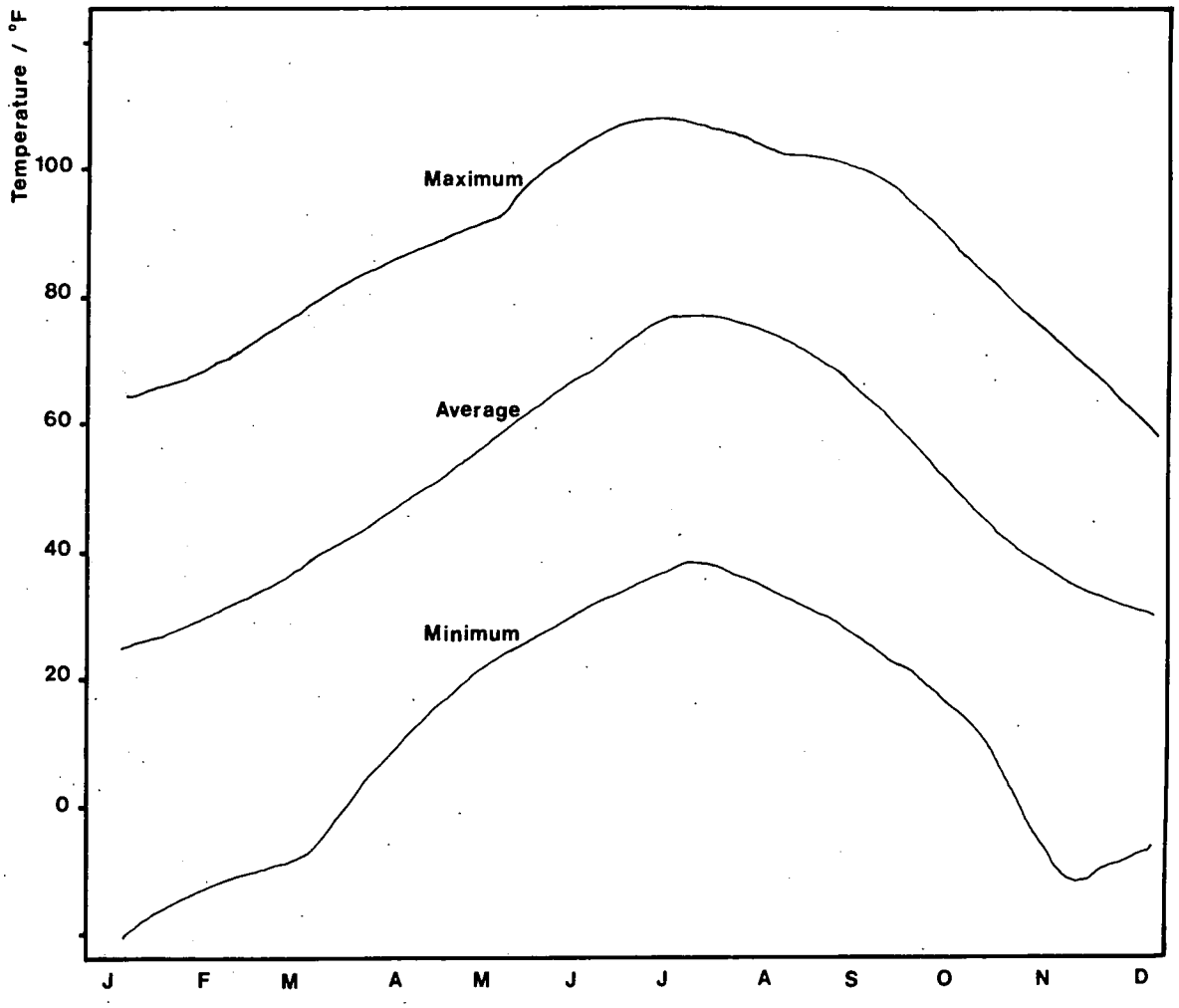

Figure 3.2 Annual Temperature Fluctuations at Dugway.

year; in some weather conditions distant lightning is a frequent occurrence in the late evening.

3.2.2 Sky Clarity.

The low humidity, remote site and high altitude (1.4 km a.s.l.) result in good sky clarity for much of the year, with stars of magnitude 6.5 being visible to the naked eye.

The cloud cover throughout the year is shown in Figure 3.3 which compares the cover at Dugway with that at three other locations, including Durham. These histograms indicate the proportion of time with less than 2/8 cloud cover throughout the year.

The disadvantage of the site in Utah is that it is subject to large fluctuations during periods when cloud free conditions may be expected, being under the competing influences of the Arctic and Sub-tropical jetstreams. A southerly drift in the Arctic jetstream brings storms followed by clear weather from the Pacific north-west; dominance by the Sub-tropical jetstream leads to hot, dusty, windy conditions, with much thunderstorm activity from the south.

3.2.3 The Site Survey.

The site has been accurately surveyed using a theodolyte and chains. The position and distance of each detector was measured from a single datum point, and the positional measurements converted to absolute values by a measurement on Polaris with reference to an ephemeris. The estimated accuracy of position and distance measurements is 0.1° and 10 cm respectively, with the

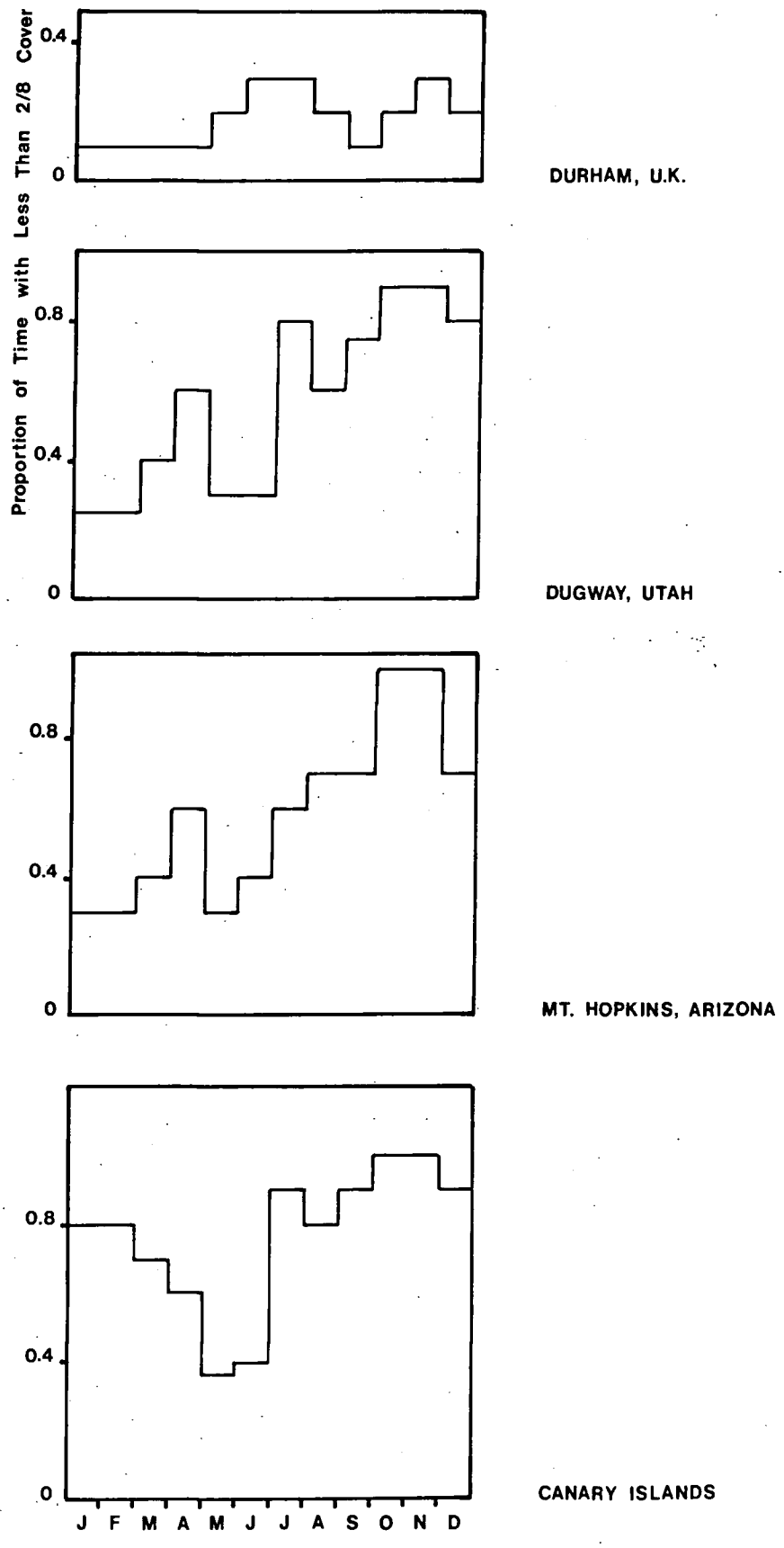

Figure 3.3 Annual Cloud Cover Variations at Four Sites.

accepted coordinates being shown inset on Figure 3.1 (these are given in metres using a right handed Cartesian coordinate system, with the x and y axes pointing east and north respectively and the z axis vertically upwards).

3.3 Mechanical Design of the Detectors.

The mechanical design of the detector was developed by Durham University staff during 1980.

3.3.1 The Alt-azimuth Platform.

An alt-azimuth platform was chosen in preference to an equatorial one since it offered fewer engineering problems, and would be less expensive to construct despite the requirement to be driven on two axes. The weight of the telescope is taken by a large central thrust bearing aided by four smaller ones acting at the perimeter of the 30" diameter platform. The steering movement is provided by two computer-controlled, 24 V d.c. motors, driving the azimuth and zenith movement through gears. To protect the bearings and motors from damage by gusting winds when the detector is not in use, it is steered to a "parked" position, and brass pegs inserted to lock it firmly in place.

All steering is done under the control of four Mostek F8 microprocessors, one for each detector, using incremental shaft-encoders to sense motion (to ± 0.1°) in each plane. This device is initiallised with the coordinates of the "parked" position, established by survey, and it then calculates the number of bits to be incremented at each shaft-encoder to arrive at each desired new position as specified by the supervising TEK 4051. As

the target is approached, the speed of slewing is progressively reduced, under F8 microprocessor control, to achieve a smooth stop, in order to prevent the motors and gear-boxes from being unnecessarily strained.

3.3.2 Covering and Waterproofing.

The equipment is well-protected against weather-damage. So that it may remain *in situ* permanently all the external electronics are sealed in waterproof, temperature-controlled boxes.

In addition, at the end of each night's observing, the following routine is executed:-

1. The detectors are steered to the parked position and pegged to prevent any motion in wind.

2. The PMTs are removed to a cooler, air-conditioned environment to prevent possible evaporation of the photo-cathode by high Summertime daytime temperatures.

3. The mirrors are covered as protection against both rain and dust.

In the event of a local thunderstorm, all connections between the recording system and the detectors are severed at both ends.

At the end of an observation period, when the equipment may be unattended for up to several months, extra precautions are taken to ensure the protection and security of the system. The system can be placed in or removed from preservation in less than 24 hours.

3.4 Optical Characteristics.

For reasons to be discussed in the following section, it was decided to employ a Cassegrain optical system. Parabolic mirrors of

1.5 m diameter and 65 cm focal length with rhodium plated surfaces were used as the primaries, while the secondaries had 25 cm diameter and 20 cm focal length. The primaries, ex-searchlight mirrors which were available at no cost, were more or less suited to the purpose of the experiment apart from their rather short focal length, giving considerable light losses from the outer regions of the mirrors and a wide field of view. The secondaries were manufactured in the Physics Department workshops at Durham University from aluminium plate by cutting and polishing.

3.4.1 The Cassegrain System.

There were several reasons for choosing a Cassegrain system as opposed to a prime focus system bearing in mind the equipment available.

Firstly, with a prime focus system the angle of incidence at the PMT would have been as large as 83° for light from the edge of the mirror, resulting in much light being lost. With the Cassegrain system this is reduced to about 33°.

Secondly, the field of view of a prime focus system would have been too big (about 11°) if the whole face of the available PMT (13 cm) had been used. A smaller field of view could have been obtained by masking down the cathodes, but this may have led to problems since the sensitivity varies across the face of the PMT, and the propogation time may also vary. The Cassegrain system uses the whole PMT face but with only a 2° field of view, by using a defocussed image as illustrated in Figure 3.4.

The main disadvantage of a Cassegrain system as opposed to a prime focus system is that it involves an extra reflection,

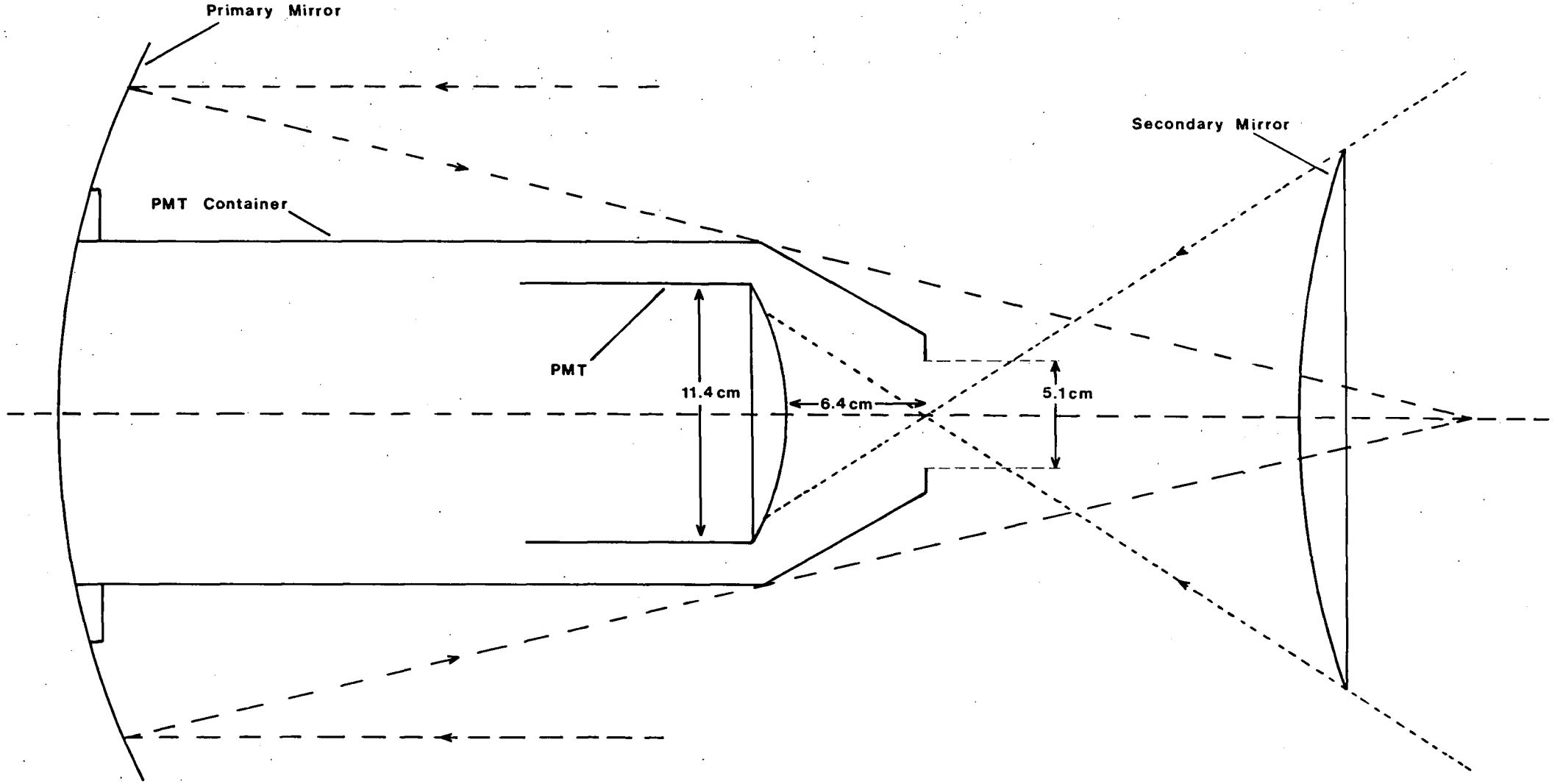

Figure 3.4 The Optical System, Showing Formation of Defocussed Image and Obscuration Caused by PMT.

resulting in greater light loss. In the Dugway system the overall reflectivity is estimated to be about 40%, with a loss of about 35% occurring at the rhodium plated primary reflector, and a similar reduction at the aluminium secondary.

3.4.2 The Optical System.

The main features of the optical system are illustrated in Figure 3.4.

A circular aperture of 5 cm diameter is placed at the Cassegrain focus, defining a physical field of view of approximately 2°. About 6 cm behind this aperture is placed the PMT. A cylindrical baffle around the secondary protects the PMT from direct illumination by the night sky. The obscuration presented by the secondary and baffle is approximately 4%.

3.4.3 The Geometrical Aperture Function.

The geometrical aperture function for each detector was determined by a raster scan of 5° diameter about a second magnitude star (Polaris). At each 0.5° step the anode current of each PMT was recorded. The results (Gibson *et al*, 1982a) are in accordance with the calculated aperture function, with a FWHM of 1.7°.

3.5 The Light Detector (PMT).

The PMT used was the RCA 4522, a fast, 12 cm, linear-focussed tube. These tubes had been employed in, and were available from, previous experiments, and had been tested thoroughly for suitability (Stubbs, internal report).

As noted in section 3.4.1, the optical system chosen uses the

whole face of the PMT. This is important due to the non-uniformity of the response of the tube across its face (*ibid.*). A 2" tube could have been used, placed at the Cassegrain focus, but this would have led to problems when bright stars appear in the field of view. The image of the star would be focussed onto the photocathode, resulting in an intensely illuminated region. This would have the effect of distorting the electron-optics, possibly affecting the gain and speed of the PMT; by defocussing the image with a larger tube these problems are reduced.

3.5.1 Operating Conditions.

An important requirement, to be discussed in the next section, is that the PMT be capable of a fast response to the Cerenkov signal. Consequently, the voltage applied across each stage is high. If all stages were used under these conditions, however, the overall gain would be too great, so only 11 dynodes are employed. The typical EHT applied between the cathode and eleventh dynode is 1800 V, giving a gain of approximately 50000. Under these conditions the sky induces a current of around 5 μA.

Individual PMT EHT settings are chosen to give rates of about 10 kHz, at a discrimination level corresponding to an estimated photon threshold of 50-100 photons m^{-2}.

Servo-controlled green l.e.d.s are used to stabilise the anode current in order to maintain the PMT at constant gain; the time constant for the servo loop is about 10 s. Typically, the addition of 50% of green light to a dark sky anode current is sufficient to maintain a steady anode current during the transit of a second magnitude star through the field of view. The measurement

of the anode current and addition of the desired proportion of green light is carried out by the TEK 4051, after which 741 operational amplifiers maintain the light level.

The PMT is isolated from the effects of the Earth's magnetic field by a cylindrical μ-metal shield maintained at the cathode potential to avoid distortion of the electron-optics.

3.5.2 The Speed of Response.

A high speed of response is required from the PMT in order to achieve a good S/N ratio and effective detection of Cerenkov light flashes by a voltage-dependent discriminator system. The longer the tube takes to respond to the flash of Cerenkov light, the more distributed in time the signal will become. This flash lasts for only a few ns and the PMT response time must be of this order. Under the current operating conditions the pulse rise time is 2-3 ns, and the FWHM about 5 ns.

3.5.3 Alignment in Time of the Response of the PMTs.

For a detector to register a threefold coincidence the signals must arrive simultaneously at the fast coincidence unit. Although care had been taken to ensure that equal lengths of cable were used for each signal path, small differences were expected. In order to achieve this accurate alignment of the signals at the coincidence unit the following procedure was adopted.

A source in the form of an l.e.d. was positioned about 200 m from the array. This was driven by an avalanche pulse generator, capable of producing very short pulses, of the order of 10 ns duration. Each detector was pointed at the source, and the PMT

signals observed on an oscilloscope. One was used as the trigger, and the other two were aligned in time with respect to this by inserting different delays into each signal path. Final checks were made by arbitrarily placing small additional delays in each channel and observing the maximum coincidence rate when detecting cosmic rays.

3.6 System Control.

The TEK 4051 controls the steering of the array and logging of data by means of a system of seven Mostek F8 microprocessors, communicating with them via the IEEE interface. The configuration of this is illustrated in Figure 3.5.

3.6.1 The Microprocessor Units.

Each detector has a dedicated microprocessor unit (MPU) assigned to it, to sense its pointing direction and control its steering (MPUs 1 to 4). The action of these was discussed in section 3.3.1.

MPU 5 is the Digital-to-Analogue Converter (DAC) controller. This provides the computer interface for 16 channels of DAC, of which 12 are used to set the reference voltages for the servo l.e.d. systems.

MPU 6 controls the printer, which is used to display the housekeeping information; this is a summary of the general performance of the array, the details of which will be discussed later in section 3.10. The information is updated by the TEK 4051 every minute, the interval between print-outs being chosen by the observer.

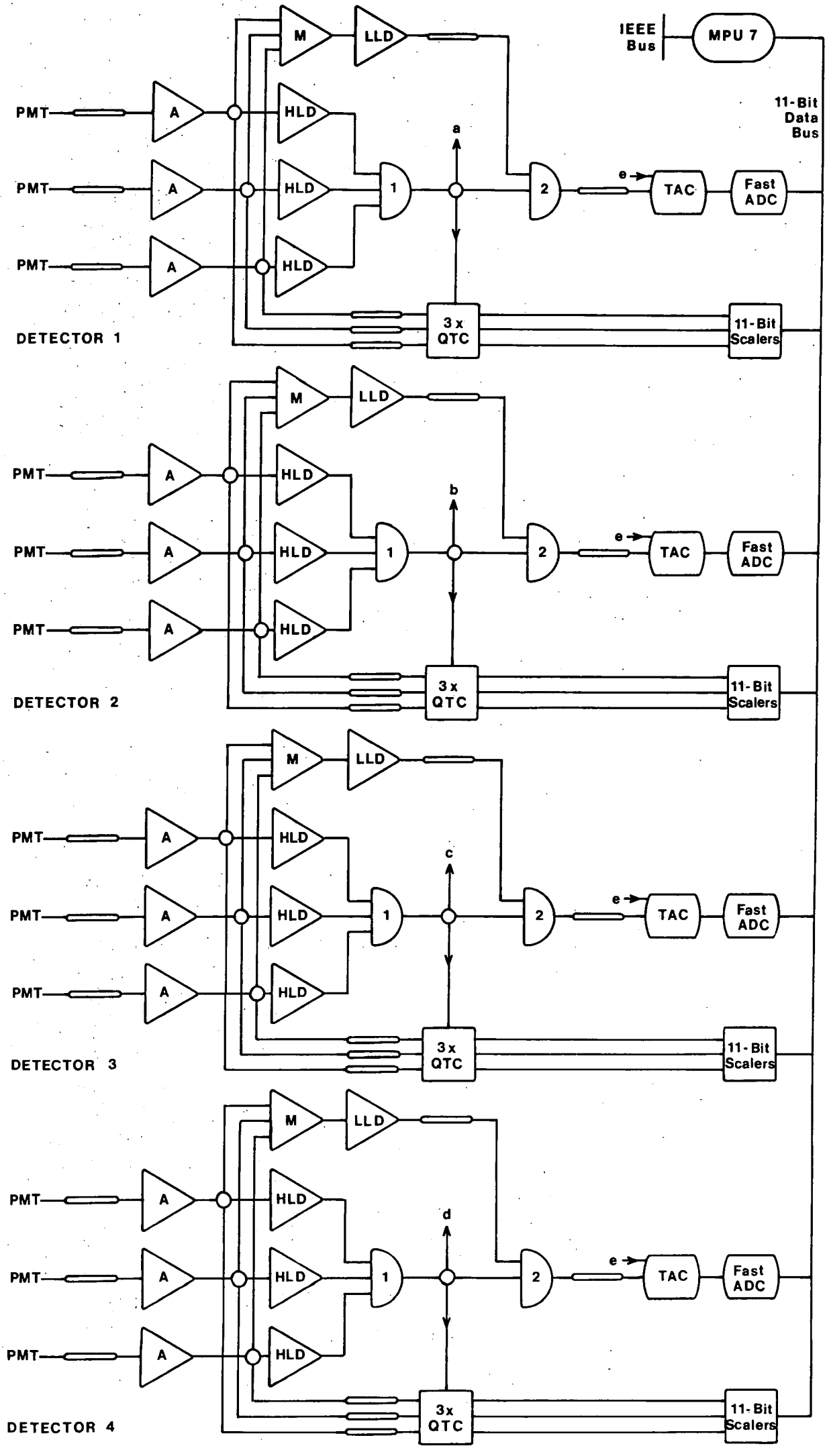
IEEE Bus
MPU 7
11-Bit Data Bus
PMT
A
M
LLD
HLD
1
2
a
b
c
d
e
TAC
Fast ADC
3 x QTC
11-Bit Scalers
DETECTOR 1
DETECTOR 2
DETECTOR 3
DETECTOR 4

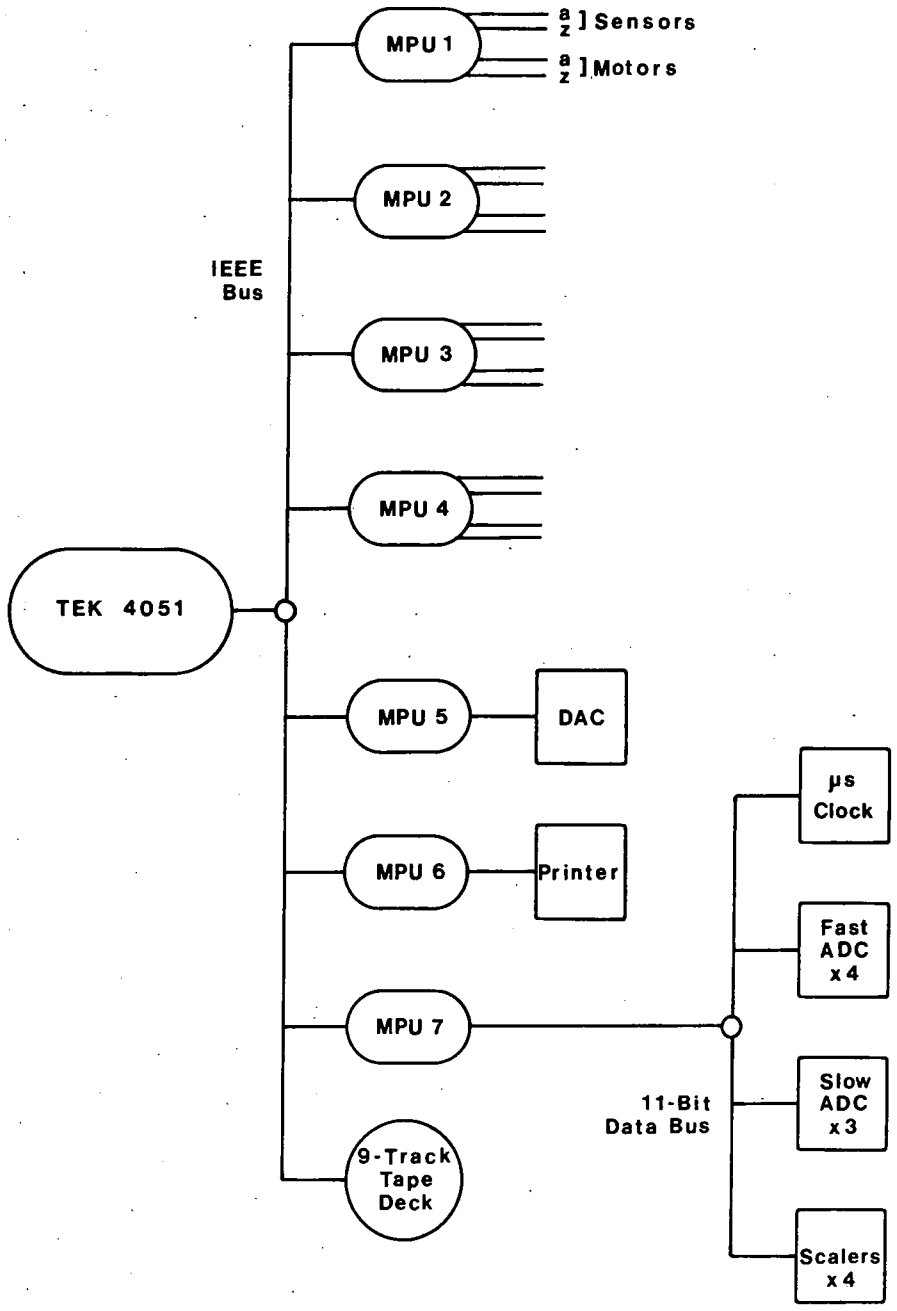

Figure 3.5 System Control Configuration.

MPU 7 supervises the logging of data, extracting the relevant information from an 11 bit data bus, which services the scalers, ADCs and the microsecond clock, and compiling the data record to be sent to the 9-track tape recorder each time the system is triggered. The information recorded is summarized in section 3.6.2.

Data is recorded in two modes. In the normal mode, when MPU 7 receives the signal from the master trigger that a signal has been detected, the data record is compiled and recorded immediately; in this mode the tape recorder is permanently waiting to record everything that appears on the IEEE bus.

The second mode is when the TEK 4051 is busy steering the array. When MPU 7 decides that a steer is due the following procedure is executed:

1. MPU 7 switches the tape deck off and signals the TEK 4051 to commence steering.

2. If the array is triggered during this mode, MPU 7 interrupts the TEK 4051 and passes the compiled data record to it for storage until steering is complete.

3. When the TEK 4051 has finished steering it switches the tape deck on, transmits to it the information it has stored, and then switches it off again.

4. The TEK 4051 then signals MPU 7 to resume control, and this reverts to normal mode and switches the tape deck on once more.

3.6.2 Information Recorded for Each Detection of the Cerenkov Signal.

Whenever the array is triggered the following data are

recorded on magnetic tape:-

1. the relative time of the occurrence of the pulse which triggered the array, with a resolution of 1 μs,

2. the relative arrival time of signals from other detectors occurring within a specified gate time, with a resolution of about 1 ns,

3. the charge in the pulses from all 12 PMTs, in the range 0-250 pC, with a resolution of 1 pC per bit,

4. the anode currents of all PMTs.

3.7 The Logging Electronics.

A flow diagram (Figure 3.6) is provided to illustrate the configuration of the recording electronics.

3.7.1 Selection Logic.

For each detector, the three PMT signals are amplified and passed through high level discriminators to a fast (7 ns) threefold coincidence unit (AND gate(1)). This determines whether or not a genuine Cerenkov light flash has been detected. The output from this is passed to a triple fan-out, from where one signal path leads to an OR gate, which is common to the array with an input for each detector (a,b,c and d in Figure 3.6). The output from this provides the master trigger, informing MPU 7 that a signal has been detected.

3.7.2 Charge-to-Time Converters.

After the amplification stage, the signal from each PMT is also passed, using fan-outs, to a charge-to-time converter (QTC),

which calculates the amplitude of the pulse. This information is stored in 11-bit scalers until it is read out by the computer.

The gates to all the QTCs within a detector are opened by the signal leaving AND gate(1). The delays in the signal paths from the amplifiers are to give this gating signal time to arrive.

3.7.3 Time-to-Amplitude Converters.

The within-field-of-view fast timing aspect of the experiment, discussed in detail in section 3.12.5, relies on obtaining the relative arrival times of the Cerenkov flash at each detector, with a resolution of about 1 ns. In order to achieve this a time-to-amplitude converter (TAC) is used for each detector, coupled to a fast analogue-to-digital converter (ADC).

All the TACs are started simultaneously by the signal leaving the OR gate (e in Figure 3.6). The stop pulse for each individual TAC is provided by that detector's low level discrimination channel as follows.

After amplification, the signals from the three PMTs are added together by a mixer, to improve the S/N ratio, and passed through a low level discriminator to AND gate(2). The other input to this gate comes from the output from AND gate(1). It is the output from this second AND gate which stops the TAC. Thus the TACs are stopped in the order in which the detectors respond to the Cerenkov pulse. If a detector fails to do so its TAC is not stopped and is automatically reset. The TAC values can then be used to calculate the relative arrival times of the flash at each detector.

The jitter on the start pulse is quite large due to the level of discrimination used, which is near the top of the signal pulse.

This is why the output from a low level discrimination channel, with much reduced jitter, is used to stop the TACs. The effect of jitter on the start pulse is eliminated since all TACs are started simultaneously.

3.7.4 The Microsecond Clock.

This provides the time of detection of the Cerenkov signal and is based on a 1 MHz oven crystal and 12-bit 30 MHz scalers; timekeeping is discussed in detail in section 3.9.

3.7.5 Housekeeping Information.

The housekeeping information, which is discussed in greater detail in section 3.10 is recorded once every minute. Slow analogue-to-digital converters (ADC) are used to translate the signals from temperature and pressure sensors and the PMT anode currents into a form suitable for recording. In addition, the individual PMT count rates, twofold coincidence rates and threefold accidental channels are recorded by 11-bit scaler units.

3.8 Calibration Routines.

3.8.1 The Time-to-Amplitude Converters.

Calibration of the TAC units was carried out using the arrangement depicted in Figure 3.7. Each TAC was started and stopped by the same pulse by using a dual fan-out and a length of cable providing a known delay. Different lengths of cable were used, and the TAC reading, in bits, noted for each one. Thus it was possible to obtain a conversion from TAC reading to real time. The results, which are plotted in Figure 3.8 (M. Walmsley, private

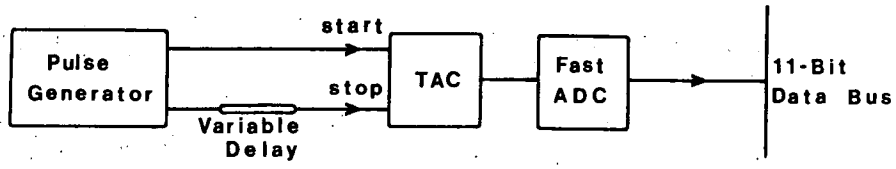

Figure 3.7 Experimental Arrangement for TAC Calibration.

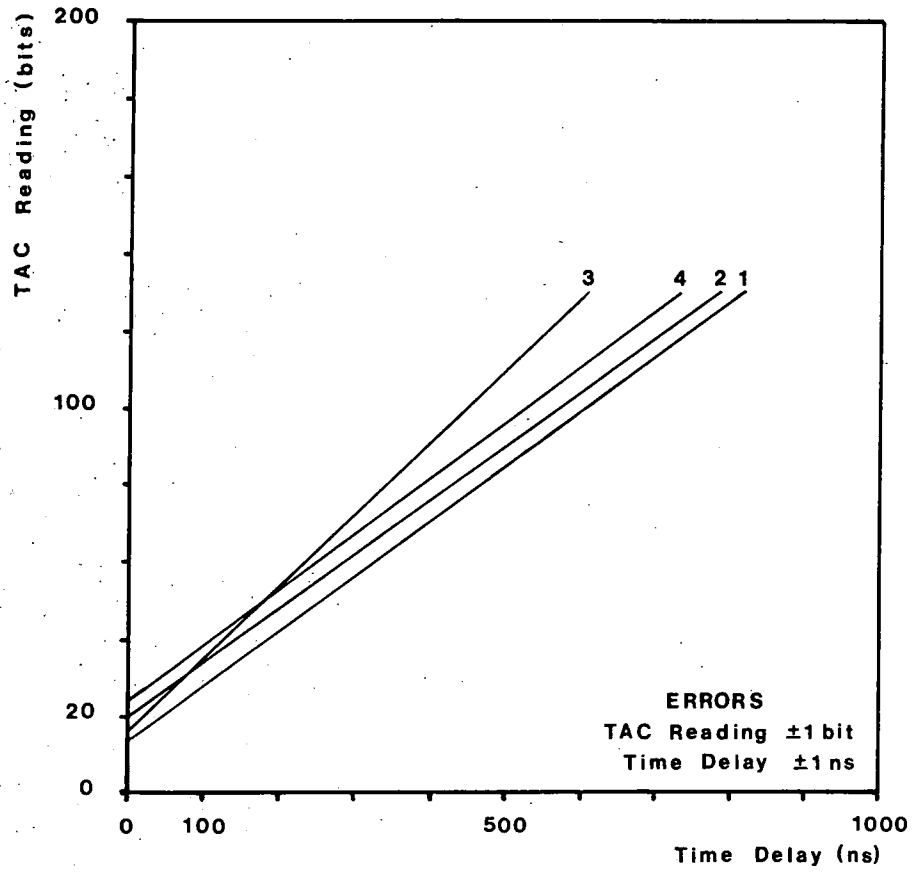

Figure 3.8 Results of Calibration of the Four TAC Units.

communication), indicate good linear responses from all units.

3.8.2 The Charge-to-Time Converters.

These were calibrated for each detector by sending a pulse simultaneously to each of its three QTC units (left (L), centre (C), and right (R)) via a triple fan-out. The number of bits registered by each was noted, the procedure being carried out using pulses of three different amplitudes. Plotted in Figure 3.9 are the ratios L/C and R/C for each detector; these are straight line graphs as would be expected for a correctly operating system.

3.9 Timekeeping.

Timekeeping is based on a local, oven-stabilised, 1 MHz crystal oscillator. The pulses produced by this are counted by a scaler unit.

3.9.1 Use of 60 KHz Off-Air Signal.

The timing signal provided by the oven crystal is checked regularly against a 1 MHz standard derived from an off-air, 60 KHz radio frequency standard, by measuring the frequency difference on an oscilloscope. Thus it is possible to maintain relative time to an accuracy of about 1 μs.

3.9.2 Absolute Timing Measurements.

The drift rate of the crystal clock is about 30 ms day^{-1}, and the regular measurements of this (section 3.9.1) allow absolute time to be maintained to an accuracy of about 1 ms using the off-air WWVB timing signal.

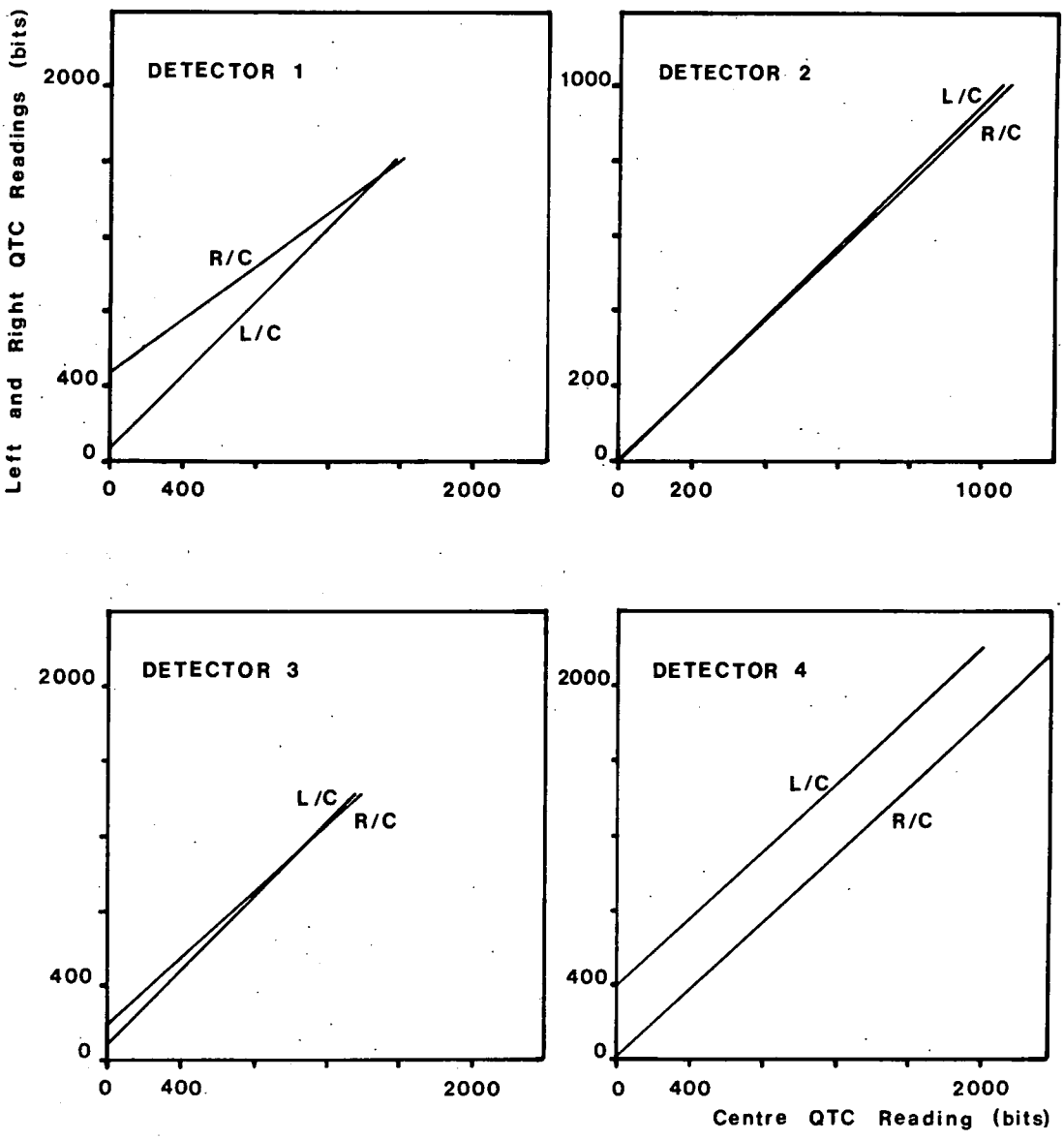

Figure 3.9 QTC Calibration Results.

The clock can run for more than 10 days before a reset is necessary which results in high relative timing accuracy. If the drift rate was high (>100 ms day^{-1}) or the measurement of it too imprecise, it would be necessary to reset the clock daily to maintain absolute time to sufficient accuracy, to the detriment of relative timing accuracy.

The WWVB signal consists of a 1 s tick for the first 50 s of each minute, followed by silence until a tone sounds at exactly 0 s. The procedure for resetting the clock is to wait for the pause in the ticks and then initialise the clock; the clock does not start immediately, but is triggered by the rising edge of the 0 s tone, giving a start time which is accurate to better than 0.5 ms.

3.10 Housekeeping Routines.

The housekeeping routines provide important information on the general operating conditions and stability of the equipment. This information is used both during an observation run, where regular updates provide confirmation that all is well, and in conjunction with the data analysis to eliminate system malfunction as a possible source of any observed effect.

The information recorded consists of the temperature, anode current and count rate of each PMT, atmospheric pressure, the number of coincidences between any two flux collectors in each telescope, the accidental threefold rate and the information recorded by the mains frequency monitor.

During an observation run this information is produced on a printer at regular intervals; the spacing of these intervals can be varied by the observers, but usually the print-outs are obtained

every time the telescope pointing directions are adjusted (typically every two minutes).

3.10.1 Temperature.

The effect of temperature variations on the performance of the RCA 4522 PMT has been investigated. Measurements were carried out on 13 PMTs operating in ambient temperatures over the range 5-35 °C, using a constant intensity light source. The transit times and EHT values were measured as functions of output pulse height at each temperature. It was found that within experimental error the PMTs were very stable over this temperature range.

3.10.2 Anode Currents.

The a.g.c. system ensures that under normal operating conditions the anode currents are constant throughout the observation. However, distant lightning can sometimes be detected, resulting in bursts of bogus light pulses. When this happens the flashes are too rapid for the a.g.c. to respond, causing wide variations in anode currents; this fact can be used to clearly identify such bursts in the data, and eliminate them from the analysis.

3.10.3 Individual PMT Count Rates.

These are monitored to ensure that the PMTs are performing correctly. Individual PMT count rates are set as high as possible for maximum sensitivity, without being so high as to result in accidental triggers of the system; typically each PMT counts at a rate of about 10 kHz.

3.10.4 Atmospheric Pressure.

The atmospheric pressure data has not yet been used in data analysis; it is recorded for completeness, and for possible future reference.

3.10.5 Twofold Mirror Coincidences.

This information is recorded to provide a link between the present experiment, using threefold coincidences, and earlier experiments which frequently used twofold coincidences.

3.10.6 Accidental Threefold Rate.

In addition to the standard recording of threefold mirror coincidences, the PMT signals from one detector are used to provide a measure of the threefold accidental rate. This is achieved by passing the signals to an extra threefold coincidence unit, but with a delay of 140 ns in one of the signal paths; this delay is long enough to ensure that any coincidences recorded by this unit are not genuine. In practise the observed accidental rate is less than $\sim$1 event hour^{-1}, which is suficiently small to be ignored.

3.11 A Typical Data Record.

Presented in Figure 3.10 is a facsimile of a typical section of data. Several different types of data record are shown, including signal records, housekeeping records, and blocking information.

3.11.1 Format of the Signal Record.

The first two integers, n_1 and n_2, are not data recorded

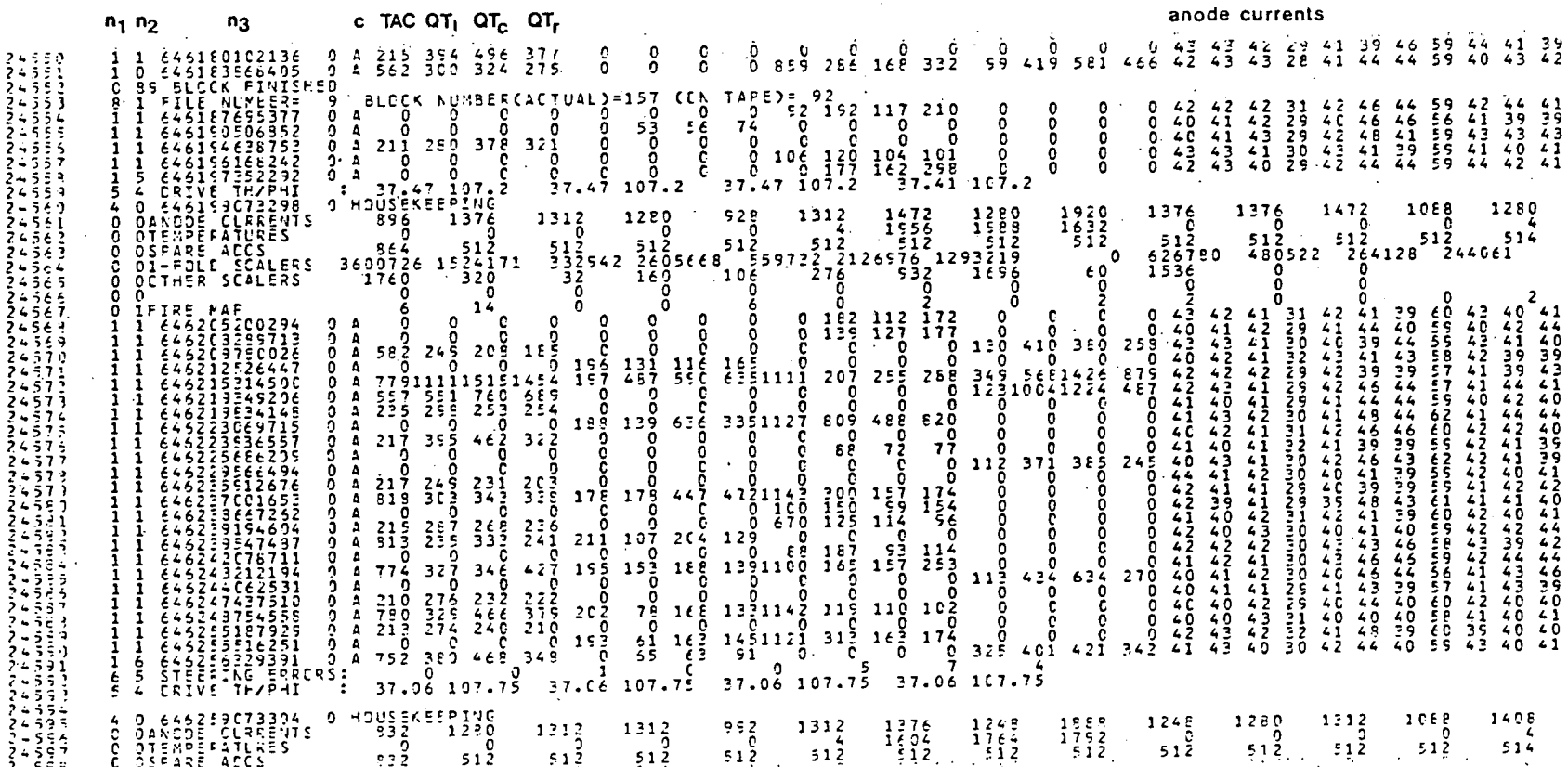

Figure 3.10 A Section of Data.

during observations, but are added later as an aid to data analysis. Their use will be discussed in Chapter 6.

The twelve digit number, n_s, is the relative time of arrival, in microseconds, of the Cerenkov pulse at the first detector. The character, c, which can take values of either 'A' or 'S' indicates which data gathering mode the system was in when the information was recorded; 'S' represents normal mode, while 'A' indicates that the TEK 4051 was steering the array (section 3.6.1).

The next four groups of numbers are the TAC and QT readings for each detector; within each group the order is TAC, QT_L, QT_C, QT_R. Finally, the anode currents of all twelve PMTs are recorded.

3.11.2 Housekeeping Information.

With reference to Figure 3.10, lines 24559 to 24567 contain a typical housekeeping record providing the following information:

Line 24559: The target coordinates in degrees (zenith and azimuth) for each of the four detectors.

Line 24560: The μs time at which the housekeeping information is delivered.

Line 24561: The PMT anode currents.

Line 24562: The PMT temperature information (not all the temperature sensors were functioning at the time these data were recorded).

Line 24564: The total number of counts recorded by each of the 12 PMTs since the previous housekeeping record.

Line 24567: A breakdown of array responses into the fifteen possible categories; details of this are contained in section 6.2.1.

3.12 Modes of Operation.

There are two modes of operation which have found frequent application, these being the drift scan (DS) mode and the tracking (TR) mode. Other possibilities exist for the operation of the flexible system and have been occasionally used.

3.12.1 The Drift Scan Mode.

In the DS mode, all detectors are pointed in the same direction and the source allowed to drift through the field of view. The advantage of this mode is that for the duration of the scan there is a constant background against which any excess from the source can be referenced. The disadvantage is that for much of the observation time the source is out of the field of view. This is thus an inefficient but reliable technique.

3.12.2 The Tracking Mode.

In the TR mode the detectors are steered as often as once a minute to keep the source near the centre of the field of view at all times. For studies of pulsars, where the prime indicator of activity is a periodicity in the signals, this is ideal. However, there is the drawback that there is no off-source data to use as a reference, and so only rather large variations ($> \sim 10\%$) in the signal intensity can be detected. For example, there can be complications in allowing accurately for the upward or downward trend in count rate due to systematically changing zenith angle.

During the course of the experiment tracking has assumed precedence over drift scanning, since the majority of the sources studied have been pulsar candidates. A further advantage of the TR

mode which has come to light since the experiment began, is that some sources exhibit variability on a time scale of minutes in their emission. For example, the Crab Pulsar has been found to emit short bursts of VHE gamma ray radiation at apparently random intervals. With the DS technique there is a strong possibility that these would occur during an off-source period and be partially or wholly missed.

3.12.3 The Survey.

Another possibility is that of surveying a large area of space, such as the entire Cygnus region, by means of a series of long, overlapping drift-scans. A step has recently been taken in this direction with a single 3 hour scan across the galactic plane through Cygnus.

3.12.4 Multiple Source Observations.

It is possible to observe two sources simultaneously by operating the system as two separate pairs of detectors. This technique has potential when for example observing speculative sources at the same time as monitoring sporadic emitters.

3.12.5 Fast Inter-Detector Timing.

When a Cerenkov light flash triggers two or more detectors, the relative time of arrival of the pulse at each can be used to calculate the direction of the source. The angular resolution of this technique depends on a number of factors.

Firstly there is uncertainty in the measurement of the arrival time of the pulse due to the presence of random sky noise;

clearly, the higher the S/N ratio is, the more accurately this time can be measured. Electronic time slewing also increases the error in measurement, but the use of dual-level pulse-gated discrimination has much reduced its effect.

Secondly, the Cerenkov light originates from an extended source, about 1° across, and this results in a large shower image in the focal plane. This is exacerbated by aberrations of the optical system and leads to jitter of the transit time across the PMT, and hence timing errors.

Thirdly, there are errors in determining the direction of the principal axis of the shower owing to the uncertainty in locating the axis impact point; the relative timing measurements merely yield a direction normal to the chord of the shower front cut by the array, which is not necessarily the most likely direction for the origin of the gamma ray. This error amounts to approximately 0.5 minutes of arc m^{-1}.

3.13 The Choice of Array Spacing.

The spacing of the array was chosen as a compromise, there being two conflicting requirements. From the point of view of achieving high count rates for statistical reasons, whether in DS or TR mode, the detectors should be sufficiently far apart to operate as independent telescopes; for a gamma ray energy of 2000 GeV, a spacing greater than about 100 m would suffice. On the other hand, a fundamental requirement of the fast timing technique is that there be multiple detector coincidences, in order to locate the direction of origin of the primary gamma ray.

The angular resolution of the array improves with increasing

detector spacing, up to the threefold limit; beyond this the detectors become independent and the technique is inapplicable. However, at the same time the effective collecting area of the array for threefold or fourfold responces is reduced. The theoretical variation of these two quantities with array size is illustrated in Figures 3.11a and 3.11b (Gibson *et al*, 1981); the quantity plotted in Figure 3.11a is the effective threefold area relative to the theoretical maximum, this corresponding to the three telescopes being positioned directly adjacent to one another.

The final choice of array spacing (Figure 3.1) represents the best compromise; the angular resolution is about 0.2°, the threefold collecting area is approximately 0.5 of the maximum possible value, and the outer detectors are approaching independence at a spacing of 100 m.

3.14 Facility Performance.

In order to illustrate the general performance capabilities of the array the night of August 25 1982 has been selected for detailed examination. It was a clear, cloudless night, during which Cygnus X-3 was tracked from the zenith down to 52°. There was no apparent excess from the source during this run.

In Figure 3.12, the rates of onefold, twofold, threefold and fourfold detector coincidences are plotted as a function of zenith angle, together with the total count rate. The perhaps unexpected features here are the dips in the responses at the zenith. This is a feature which also appeared in the 1981 data. Its origin and implications will be discussed in Chapter 4.

In Figure 3.13, the relative sensitivities of the four

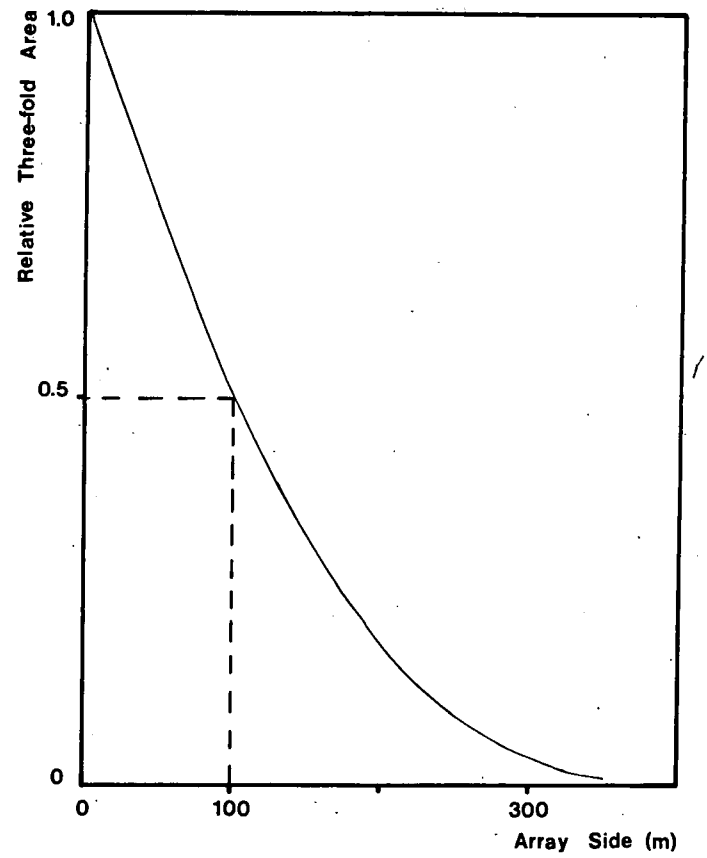

Figure 3.11a Relative Three-fold Area as a Function of Array Size.

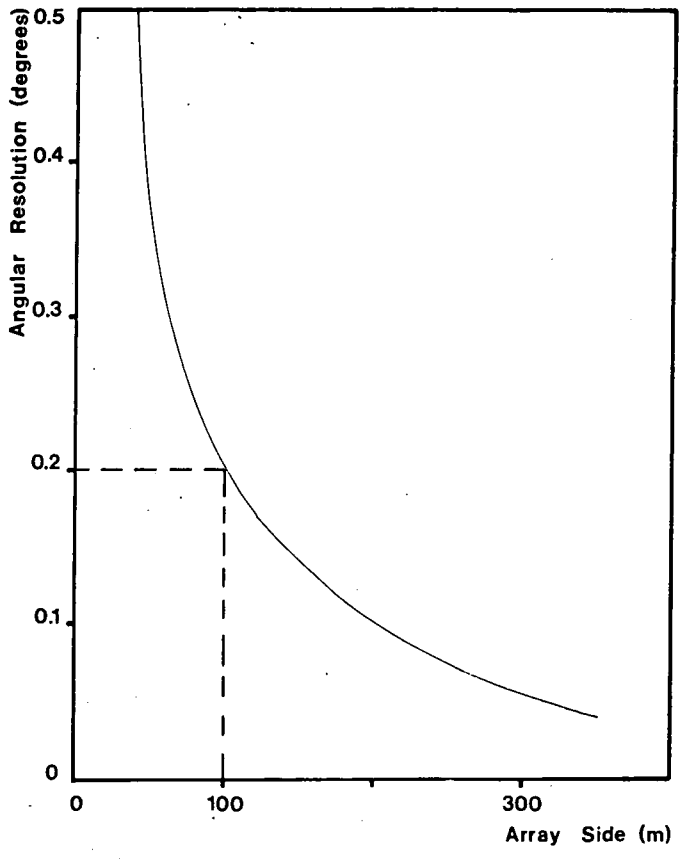

Figure 3.11b Angular Resolution for Inter-Detector Timing as a Function of Array Size.

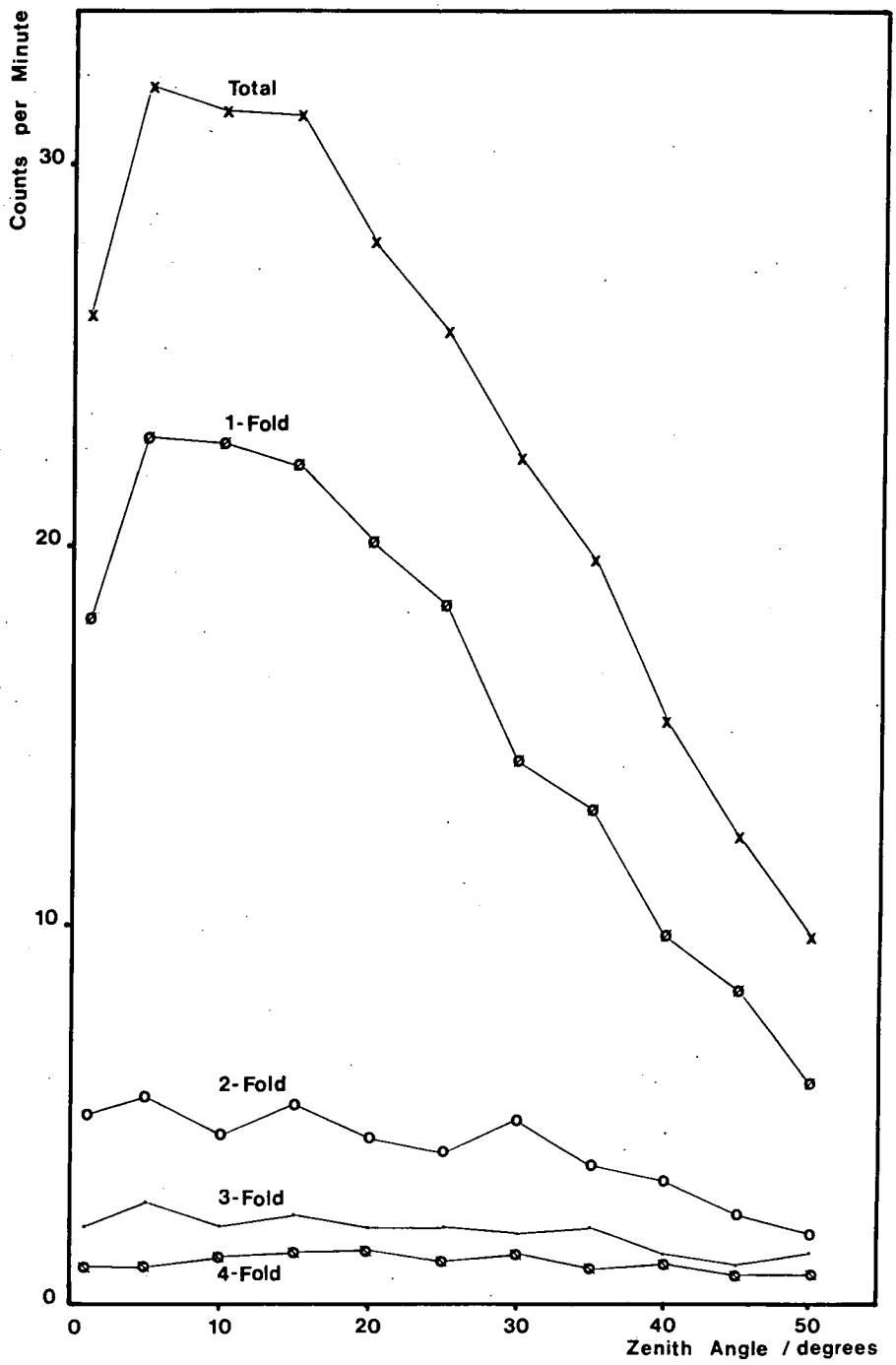

Figure 3.12 Example of Array Performance in 1982.

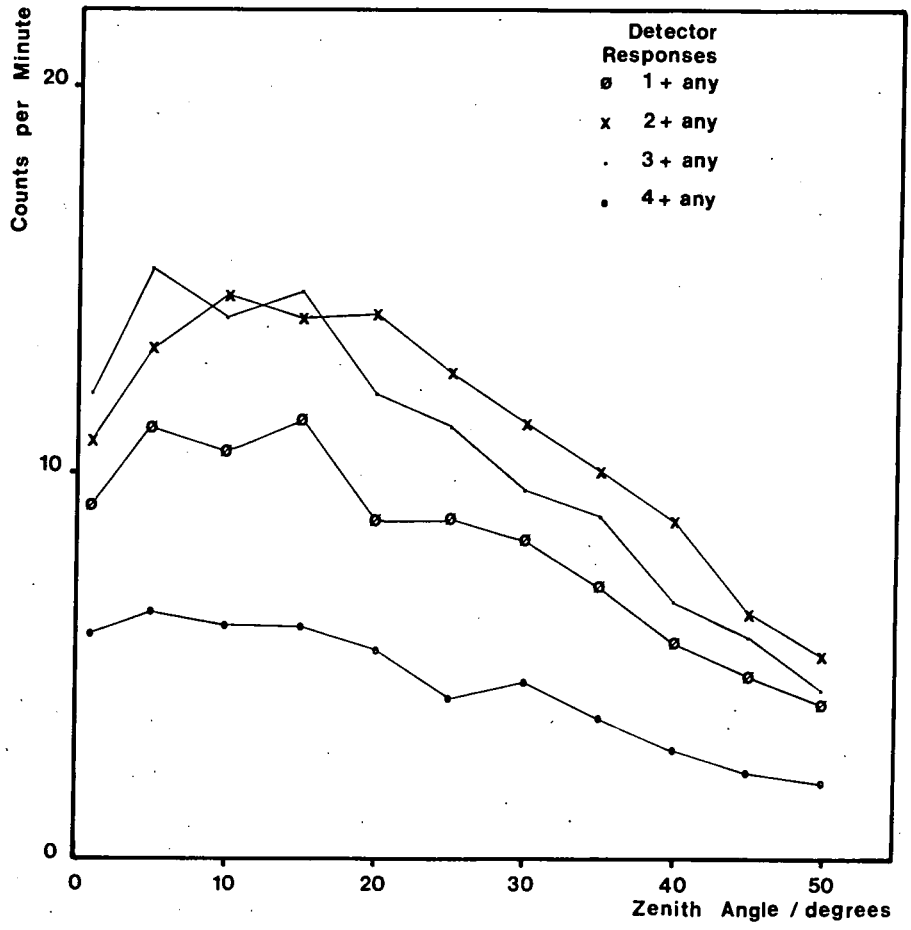

Figure 3.13 Relative Sensitivies of the Four Telescopes.

telescopes are illustrated. The total number of responses by each detector is plotted against zenith angle. (No account is taken of which other detectors were also triggered, so these are not independent graphs.) Nevertheless, they show that detectors 2 and 3 are of relatively low threshold, detector 4 is relatively high, and detector 1 is intermediate. This difference in sensitivities was not a design feature, but reflects the varying quality of mirror surfaces and PMTs in use. It has, however, proved useful in estimating the slopes of energy spectra, as discussed in Chapter 7 (section 7.1.4).

3.14.1 The Energy Threshold and Collecting Area.

The interelationship between collecting area and energy threshold makes it difficult to provide an accurate measure of either. From examination of the data in terms of single and multiple-fold responses (Figure 3.12) it is clear that the collecting area of a single telescope corresponds to a circle of radius ~50 m, that is, ~1.5×10^4 m^2; if it were much larger than this, the proportion of multiple-fold responses would be greatly enhanced at the expense of single detector triggers, much smaller and the converse would be the case.

Based on this it is possible to estimate the threshold of a single telescope by noting the count rate when there is no source of VHE gamma rays in the field of view; under this condition the detector is recording the CR background. By considering the estimated collecting area it is possible to calculate the flux detected, and since the energy spectrum of the CR background is well established an estimate of detector threshold is possible.

For the four detectors in the Dugway array the estimated energy thresholds vary over the range 1-2 TeV, with an estimated error of ~40% (Kirkman, private communication and forthcoming Ph.D. thesis).

CHAPTER 4.

THE SIMULATION OF CERENKOV LIGHT PRODUCED BY 1000 GeV GAMMA RAYS.

Detailed computer simulations have been made of the production of Cerenkov light in the cascades produced by 100-1000 GeV gamma rays, and include the responses of two detection systems. The results relating to one of these, the Dugway facility, are dealt with in the second part of this chapter, while those relating to the other, the Mount Hopkins Imaging experiment, will be discussed in Chapter 5. In the first part of this chapter the mathematical model employed is examined.

4.1 The Mathematical Model.

In the next section an overview of the original program is given. This is followed by a description of the modifications and additions employed in the current simulations.

4.1.1 The Original Program.

The original calculations were developed at Durham between 1971 and 1979 (Smith and Turver, 1973, Browning and Turver, 1977, Protheroe and Turver, 1979, McComb and Turver, 1981) in conjunction with the extensive air shower (EAS) experiments at Haverah Park, and at Dugway, Utah. These calculations were designed to produce predictions for Cerenkov light produced by CR protons and gamma rays. The published data on gamma ray showers were of general application, no attempt being made to tailor them to any particular experiment.

The electron-photon cascade was simulated in three dimensions

using a Monte Carlo calculation. A left-handed Cartesian coordinate system was used with the origin defined as the point of injection of the primary gamma ray. The x direction was defined as magnetic east, the y direction as magnetic north, and the z direction towards the Earth's centre.

The tracks of all electrons and positrons were split into straight segments approximating to their curved trajectories in the geomagnetic field and the Cerenkov light component calculated as follows. (The term 'electron' will be used generically to include positrons unless otherwise stated.)

The cone of radiation produced by each segment of the electron track, which was assumed to originate at its midpoint, was represented by 180 rays of photons terminating in the observation plane and forming there an ellipse. These were then binned by core distance (using a series of annular rings centred on the core impact position), zenith angle, wavelength and time.

The processes whose effects were incorporated in the model include Bremsstrahlung, pair-production, multiple Coulomb scattering, Compton scattering, ionisation and direct pair-production by electrons. The effect of the Earth's geomagnetic field was also included. The attenuation of light in the atmosphere was calculated using the model of Eltermann (Eltermann, 1968).

The results of these original calculations were compared with those obtained by other workers using different simulation programs by Browning and Turver (Browning and Turver, 1977). Extensive comparison of the results was difficult because of the very different, more detailed approach to the calculations particularly with regard to the inclusion of the effect of the Earth's

geomagnetic field, these being the first calculations to do so. Nevertheless some general areas of agreement were found, a full discussion of which is given in the above mentioned paper.

4.2 The Simulation of the response of the Dugway System.

The aim of the current work was to simulate as closely as possible the response of the Dugway system to 1000 GeV gamma rays. The simulations were to be used to assist in the choice of array spacing, and the estimation of the telescope threshold energy and collecting area.

4.2.1 Modifications Employed in the Simulations.

Most of the original computer code remained unaltered, including the parts dealing with cascade development and Cerenkov light production. The binning routine, however, was replaced.

Photon densities were binned in a rectangular matrix of 1225 (49 x 25) detectors of the type employed at Dugway, pitched at 15 m in the x-direction (east) and 26 m in the y-direction (north). These dimensions were chosen to accommodate the geometry of the actual array (Figure 4.1). The use of such a matrix enables a single shower to be observed by a Dugway-type array from many different positions relative to the shower's core.

As in the actual experiment, each detector in this matrix consisted of three paraxial flux collectors, each with geometrical angular acceptance of 1.7°. Details of the geometrical aspects of the binning are given in the following section.

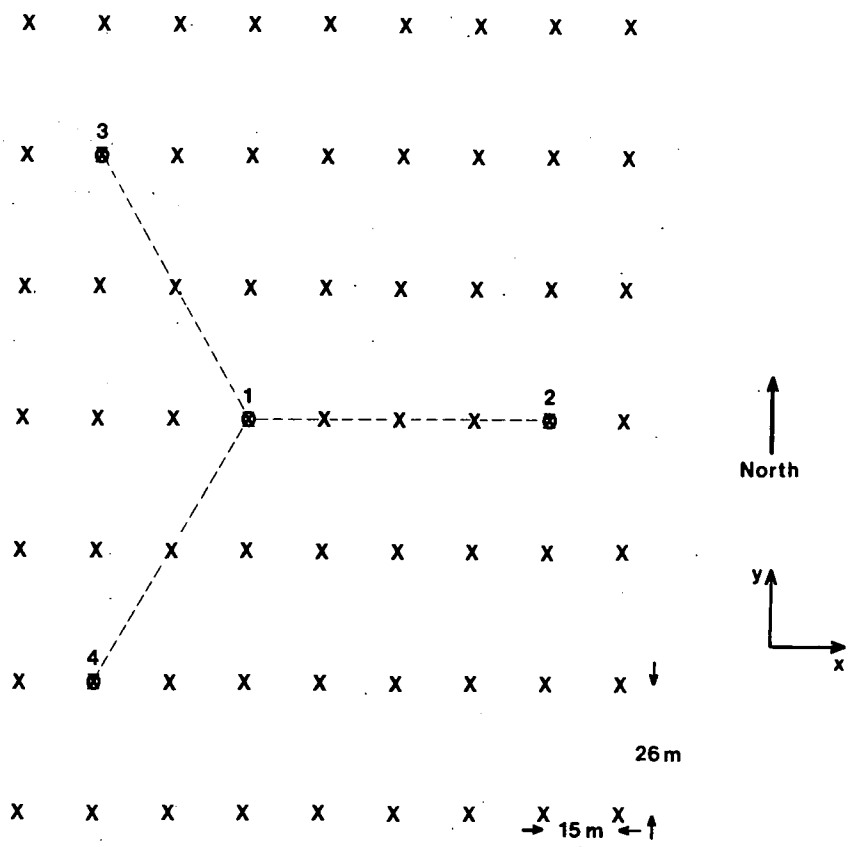

Figure 4.1 A Section of the Binning Matrix Showing a Possible Location for the Array.

4.2.2 Binning Geometry.

In order to simulate the acceptance of a detector as accurately as possible, the following procedure was adopted.

Each ray of photons was dealt with individually. The existing program provided the coordinates of P_o, the mid-point of the track segment producing the ray, the coordinates in the observation plane of P_1, the point of impact of the ray, and the ray's photon density at this point.

The first step was to determine to which detector in the matrix P_1 was closest, the detectors being spaced sufficiently far apart to make the closest detector the only one capable of intercepting the ray.

Two conditions must be satisfied for the telescope to be considered to detect the ray: the path of the ray must be intercepted by one of the telescope's three mirrors, and its direction must fall within the cone of acceptance. For reasons of computing efficiency, the latter condition is investigated first.

In Figure 4.2 the technique used is illustrated. The telescope is represented by three circles of 1.5 m diameter lying in a plane. It is considered to pivot about the point $P_3(x_3,y_3,z_3)$, the middle of the central mirror. The ray of photons originates at $P_o(x_o,y_o,z_o)$ and terminates in the observation plane at $P_1(x_1,y_1,z_1)$, intersecting the plane of the telescope at $P_2(x_2,y_2,z_2)$. The angle α_1 is that between the line P_oP_1 and the normal to the plane, while α_2 is that between P_oP_3 and the normal.

In general, the angle (α) between two lines with direction cosines (l_1,m_1,n_1) and (l_2,m_2,n_2) is given by the equation

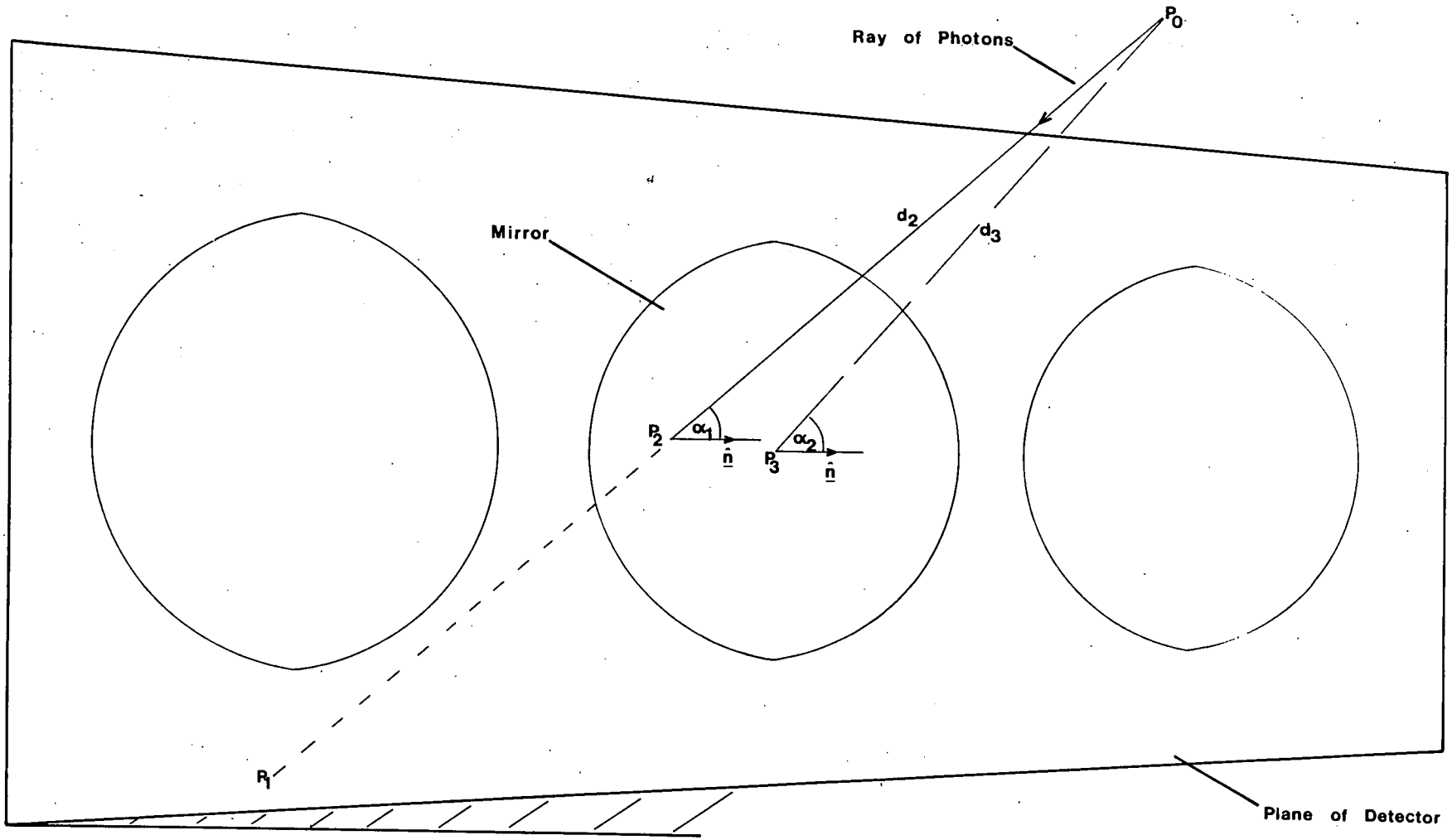

Figure 4.2 Illustration of Technique Used to Determine Whether a Ray Has Been Intercepted.

$$\cos(\alpha) = l_1 l_2 + m_1 m_2 + n_1 n_2 \qquad (4.1)$$

For the ray, P_oP_1, the direction cosines are given by

$$l_1 = \frac{\delta x}{d_1} \qquad (4.2)$$

$$m_1 = \frac{\delta y}{d_1} \qquad (4.3)$$

$$n_1 = \frac{\delta z}{d_1} \qquad (4.4)$$

where

$$\delta x = (x_o - x_1)$$

$$\delta y = (y_o - y_1)$$

$$\delta z = (z_o - z_1)$$

and d_1, the length of P_oP_1, is

$$d_1 = [\delta x^2 + \delta y^2 + \delta z^2]^{0.5}$$

For the telescope, pointing in a direction (θ,ϕ) the direction cosines are

$$l_2 = \sin(\theta)\cos(\phi) \qquad (4.5)$$

$$m_2 = \sin(\theta)\sin(\phi) \qquad (4.6)$$

$$n_2 = \cos(\theta) \qquad (4.7)$$

Hence α_1 may be found using equation (4.1). For detection, the inequality $\alpha_1 < 0.85$ must hold.

To satisfy the other condition, the point P_2 must lie within one of the three circles. Its coordinates are calculated as follows.

A more general form of equation (4.2) is

$$l_1 = \frac{(x_o - x)}{d}$$

where x is any point on the line P_oP_1, and d is the distance of that point from P_o. Rearranging this, we obtain

$$x = x_o - l_1 d \ .$$

We are interested in x_2, so we use

$$x_2 = x_o - l_1 d_2 \qquad (4.8)$$

Therefore in order to obtain x_2 we need to know d_2, the length of the line P_oP_2.

Now, the perpendicular distance, p, from P_o to the plane is given by,

$$p = d_2 \cos(\alpha_1) \qquad (4.9)$$

and also

$$p = d_3 \cos(\alpha_2) \qquad (4.10)$$

Since d_3 (the length of the line P_0P_3) and α_2 may be calculated in a similar way to d_1 and α_1, the coordinates of P_3 being known, we may eliminate p from equations (4.9) and (4.10) to yield,

$$d_2 = \frac{d_3\cos(\alpha_2)}{\cos(\alpha_1)} \qquad (4.11)$$

Substituting into equation (4.8) we have

$$x_2 = x_0 - \frac{l_1 d_3\cos(\alpha_2)}{\cos(\alpha_1)} \qquad (4.12)$$

Similarly

$$y_2 = y_0 - \frac{m_1 d_3\cos(\alpha_2)}{\cos(\alpha_1)} \qquad (4.13)$$

$$z_2 = z_0 - \frac{n_1 d_3\cos(\alpha_2)}{\cos(\alpha_1)} \qquad (4.14)$$

Using equations (4.12)-(4.14) the coordinates of P_2 may be found. Then the distance, r, between P_2 and the centre of each 'mirror' can be calculated. If the condition $r <= 0.75m$ is fulfilled for any of these the ray is considered to have struck that one.

At this point the attenuation of light in the ray is determined in order to calculate the photon density, which is then stored.

4.2.3 Considerations of Computational Efficiency.

An important consideration regarding the implementation of the modifications was the efficiency of the code; for example, the subroutine containing the binning processing is called $\sim 10^5$ times for a cascade initiated by a 1 TeV gamma ray. In order to maximise the efficiency of the code two main strategies were adopted.

The first of these involved attempting to eliminate as many 'rays' of photons as possible simply on the basis of the information regarding the point of impact on the ground without resorting to the complicated, and therefore expensive, calculations described in the previous section. Given the physical characteristics of a telescope, including its size and angle of acceptance, and applying the constraint that it not be operated at zenith angles greater than 60°, it is possible to define for each a catchment area in the ground plane. With the chosen telescope spacing in the matrix this catchment area is small compared to the total area of the matrix.

After the coordinates in the ground plane of the point of impact of a ray of photons have been calculated, the next step is to determine to which telescope this point is closest. This is done by translating the coordinates into a frame of reference with units in x and y directions chosen such that the coordinates of telescope locations are integers, the central telescope being located at (25,13); this is to facilitate storage of the detected signal in computer memory. It is then a straightforward matter to decide whether the coordinates of the point of impact are sufficiently close to integer values to be within a telescope's catchment area, and if they are not the ray is abandoned, thus avoiding the

complicated calculations outlined in the previous section.

The second strategy involved running the simulation program in conjunction with a supplied system subroutine whose purpose is to monitor the distribution of cpu time among the program's subroutines and functions. This produced a detailed report from which it was possible to identify the most frequently executed sections of code and take steps to improve their efficiency. By this means the average cpu time used by the program was reduced by about 30%.

4.3 Checks of the Simulations.

To minimize the possibility of corrupting the existing program, the new sections of code were inserted as extra, as opposed to replacement, and redundant code was simply bypassed rather than deleted altogether. These new sections were thoroughly tested in isolation from the rest of the program before use, particularly those relating to the geometrical calculations described in section 4.2.2.

As a final check, before any deductive work was carried out using the new simulations, they were tested against previous calculations using the same basic code (Browning and Turver, 1977, Protheroe and Turver, 1979). The aim of these tests was not to establish the validity of the cascade production part of the program since this had already been achieved (section 4.1.1), rather to check that the new binning routines gave sensible results. It was not possible to compare the present results with similar calculations made by other workers since none exists which is directly comparable.

Lateral distributions for vertically injected showers at energies of 100, 300 and 1000 GeV were obtained by averaging the appropriate events from the simulation database, details of which are given in the next section. The results are shown in Figures 4.3 and 4.4 where they are compared with similar plots obtained at 100 and 300 GeV by Browning and Turver (Browning and Turver, 1977), which employed geometrical apertures of 1° and 3° (FWHM), compared to the present value of 1.7°, and an observation altitude of 2380 m a.s.l. instead of the Dugway altitude of 1448 m a.s.l. The current results are consistent with previous work. (It should be noted that the current lateral distributions refer to an origin at the centre of the detector matrix, the position of core impact, but that the peak in intensity of the light pool generally occurs away from this point, as discussed later in section 4.5.1. Consequently Figures 4.3 and 4.4 do not represent the maximum photon densities recorded. However, since the previous results (*ibid.*) were also centred at the position of core impact this was the most appropriate way of calculating lateral distributions for the purpose of comparison).

4.4 The Simulation Database.

Preliminary estimates of the threshold energy of the Dugway detectors yielded a value of the order of 1000 GeV. As this is the highest energy which can be realistically simulated given the constraints set by considerations of available time on the computer, it is upon cascades initiated by gamma rays of this energy that the results are based. However, as mentioned in the previous section, in order to provide a link with earlier calculations at lower energies based on the same program (Browning

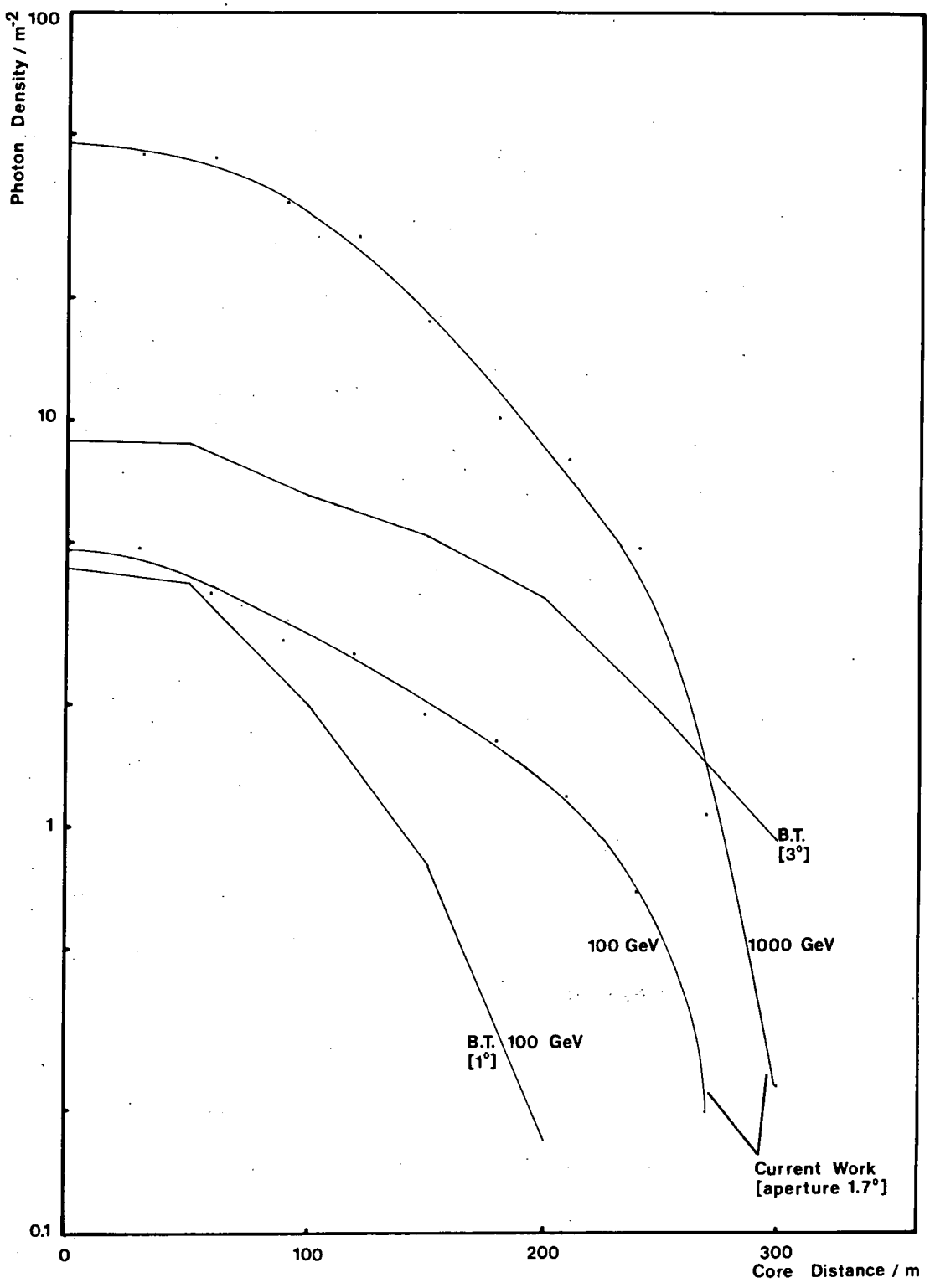

Figure 4.3 Comparison of Lateral Distributions with Previous Work at 100 GeV.

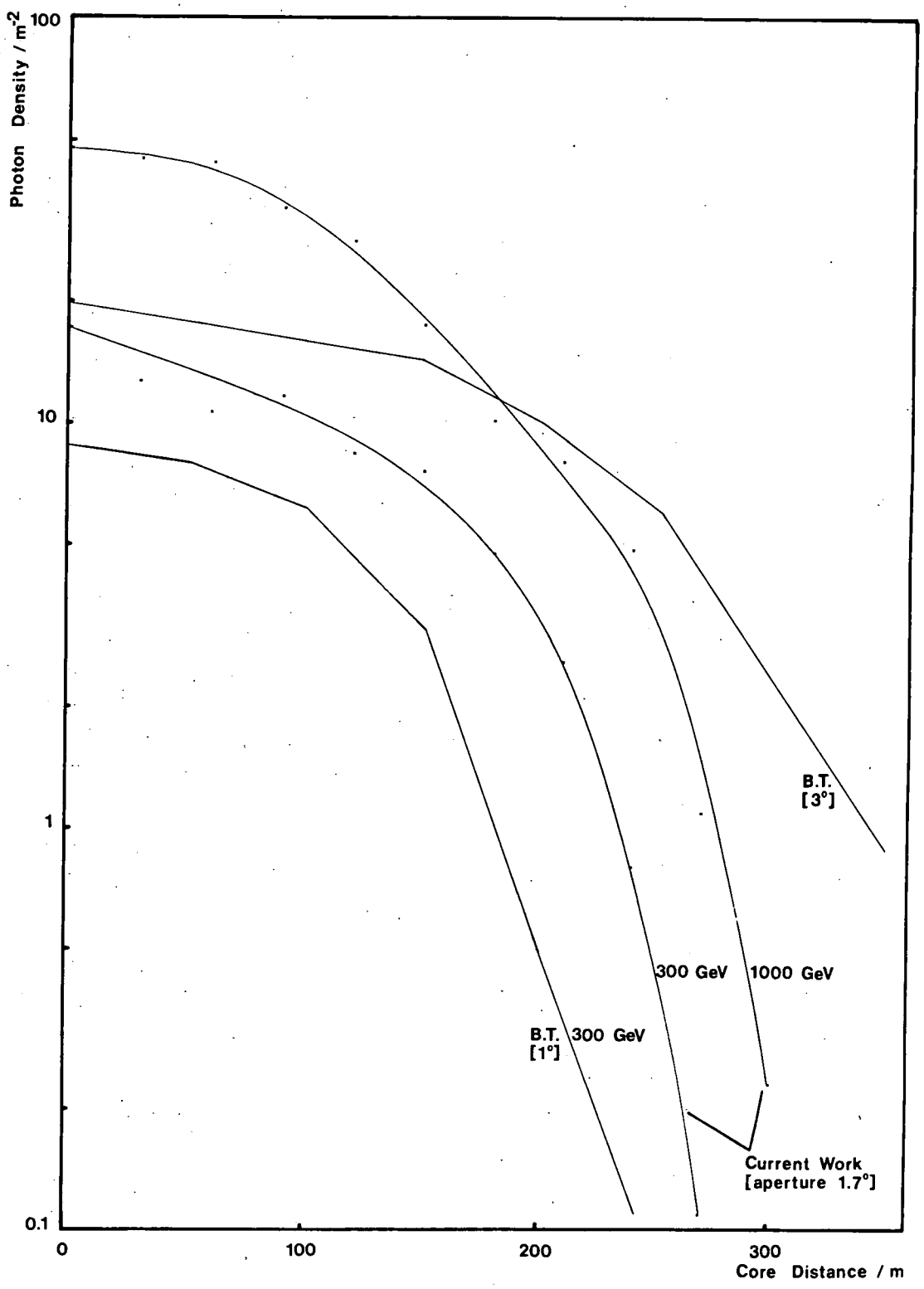

Figure 4.4 Comparison of Lateral Distributions with Previous Work at 300 GeV.

and Turver, 1977), simulation of 100 GeV and 300 GeV gamma ray initiated showers was also carried out (Figures 4.3 and 4.4).

Simulations were obtained with primary gamma rays injected at 0, 10 and 35 degrees to the zenith to provide a measure of the performance of the array over the range of zenith angles employed in the actual observations. A summary of the calculations made is given in Table 4.1.

Each simulated shower is initiated by a 10 digit random number. To allow as close a comparison as possible between cascades initiated by gamma rays of different injection angles, the numbers selected randomly for the vertically injected showers were retained for the non-vertical ones, so that as near as is possible the same cascade developments were used. Of course, the shower development is different in detail at different injection angles, but the general characteristics, such as the depth at which the cascade maximises, are similar.

The results of each simulation are observed by the matrix of 1225 detectors seven times, that is, with detectors pointing along the line of approach of the primary gamma ray, and with them tilted up to ± 3° off-axis, in 1° increments (no significant signal is detectable at offset angles greater than 3°). This simulates the effect of a source passing through the field of view of the telescopes, and is used to calculate their effective aperture functions.

4.4.1 Basic Output from the Calculated Showers.

The information produced upon completion of a simulated gamma ray initiated cascade falls broadly into three categories:

Table 4.1

Energy(GeV)	Injection Angle(Zen)	No. of Events
1000	0	20
1000	10	20
1000	35	20
300	0	10
300	10	10
300	35	10
100	0	25
100	10	10
100	35	25

Table 4.2

Primary gamma ray energy = 1000 GeV
Injection angle Zenith = 0.0°, 10.0°, 35.0°
Azimuth = 90.0°
Injection altitude = 29600 m a.s.l.
Observation altitude = 1448 m a.s.l. (Dugway)
Energy cut-off to ensure emission = 20.0 MeV

1. Firstly there are general details regarding the initial parameters selected, including the energy of the primary gamma ray, its injection angle and altitude, the observation altitude, and the electron energy threshold for emission of Cerenkov light. The values employed throughout these calculations are given in Table 4.2.

2. Secondly a summary is given of the electron number development and the number and energy of electrons and photons reaching the observation level. The former is particularly useful in distinguishing between showers which develop normally, and those developing particularly early or late in the atmosphere. Generally, the deeper the primary gamma ray penetrates into the atmosphere before the first interaction occurs, the narrower is the pool of light produced at the observation level.

3. Thirdly, the response of the large matrix of Dugway-type detectors is given in units of photons m^{-2}, as a function of offset angle between the direction of travel of the primary gamma ray and the orientation of the telescopes. This forms the principal database for analysis to assist the Dugway experiment.

4.4.2 Map of Array Responses.

For the main analysis the information in the database undergoes further processing. A map of array responses is produced by considering the response of a Dugway-type array at each position in the ground plane covered by the matrix. Examples are provided in Figures 4.5a,b,c and d, which are maps derived from a cascade produced by a vertically injected 1 TeV primary gamma ray, observed over a range of detector thresholds. The position (0,0) is that of

Shower No. : H.D.206

Threshold : 40.0 photons/sq. m

Detectors pointing along shower axis

Core impact position at (0,0) (axis units are metres)

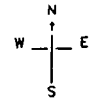

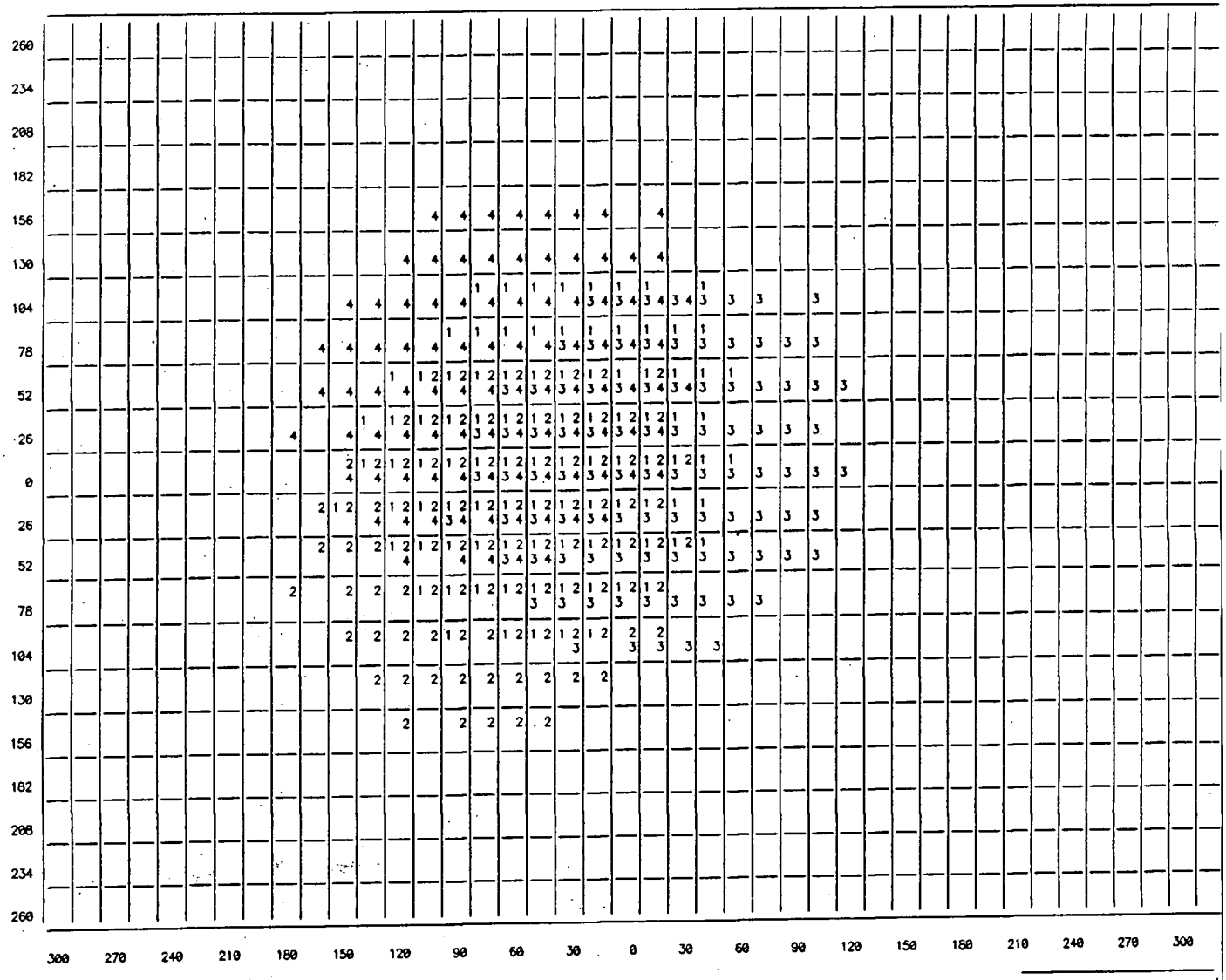

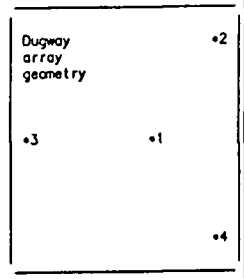

Breakdown of responses

Number of 4-folds = 26						
Number of 3-folds = 39	123(14)	124(16)	234(0)	134(9)		
Number of 2-folds = 37	12(10)	13(12)	14(10)	23(2)	24(2)	34(1)
Number of 1-folds = 93	1(0)	2(27)	3(33)	4(33)		

Figure 4.5a Map of Array Responses to Vertically Injected 1000 GeV Shower.

Shower No. : H.D.206

Threshold : 55.0 photons/sq. m

Detectors pointing along shower axis

Core impact position at (0,0) (axis units are metres)

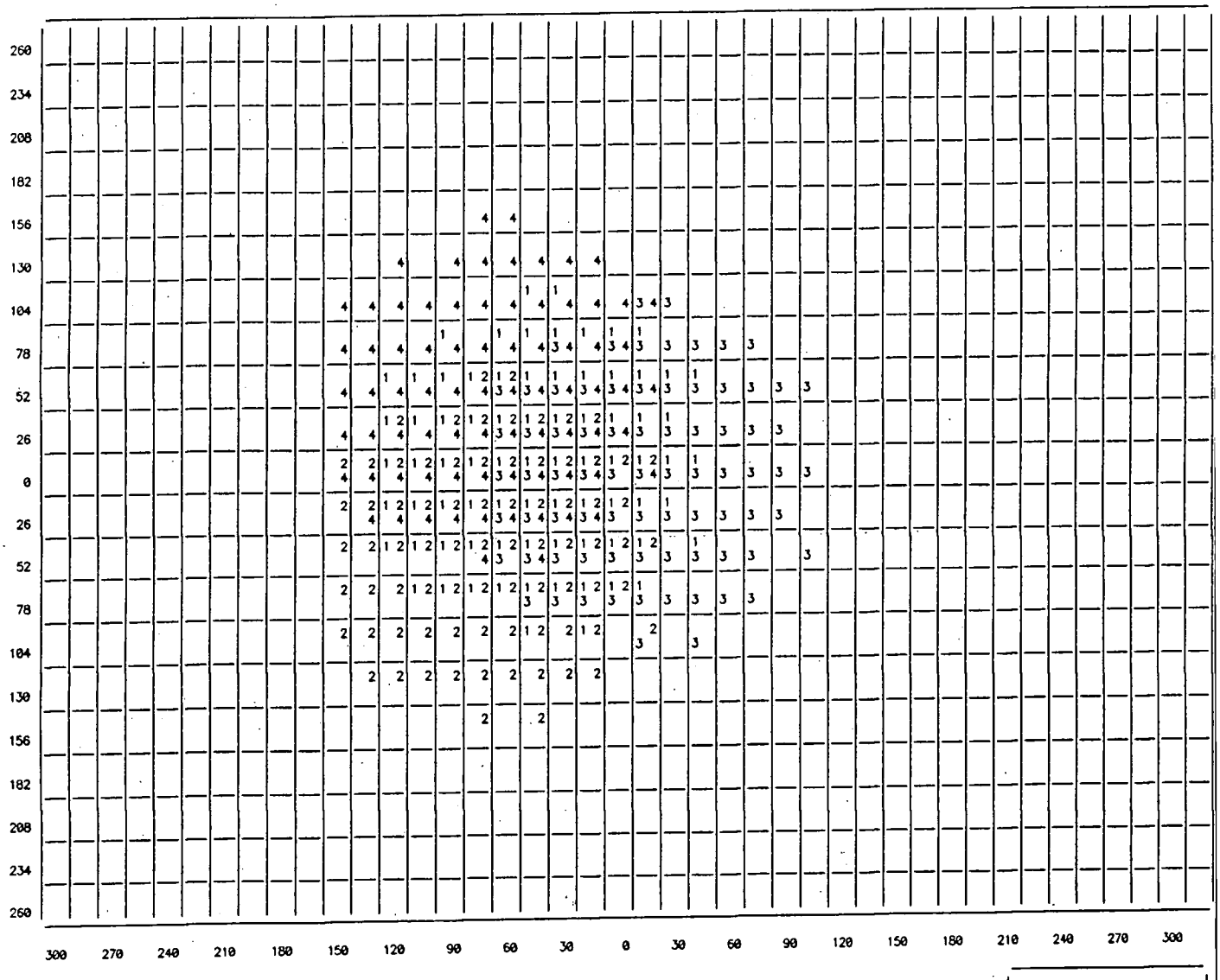

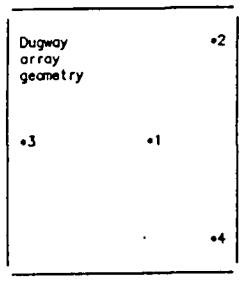

Breakdown of responses

Number of 4-folds = 15

Number of 3-folds = 32 — 123(11) 124(13) 234(0) 134(8)

Number of 2-folds = 35 — 12(9) 13(11) 14(10) 23(1) 24(3) 34(1)

Number of 1-folds = 82 — 1(0) 2(25) 3(30) 4(27)

Figure 4.5b Map of Array Responses to Vertically Injected 1000 GeV Shower.

Shower No. : H.D.206

Threshold : 70.0 photons/sq. m

Detectors pointing along shower axis

Core impact position at (0,0) (axis units are metres)

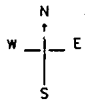

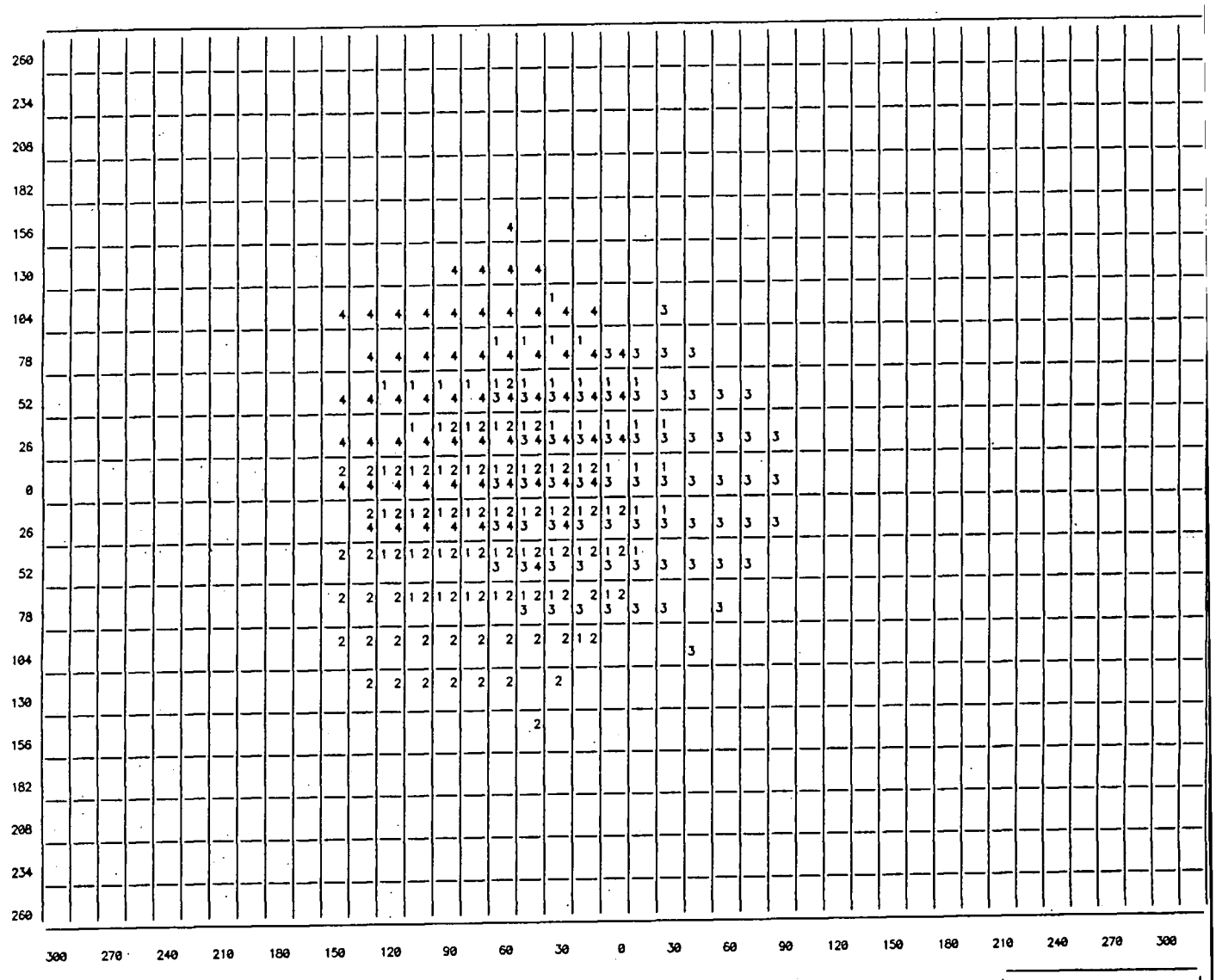

Breakdown of responses

Number of 4-folds = 9						
Number of 3-folds = 28	123(10)	124(11)	234(0)	134(7)		
Number of 2-folds = 33	12(9)	13(9)	14(10)	23(1)	24(3)	34(1)
Number of 1-folds = 74	1(0)	2(22)	3(28)	4(24)		

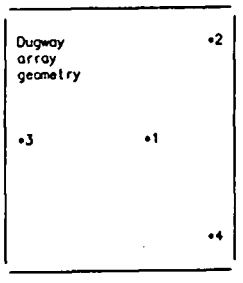

Figure 4.5c Map of Array Responses to Vertically Injected 1000 GeV Shower.

Shower No. : H.D.206

Threshold : 85.0 photons/sq. m

Detectors pointing along shower axis

Core impact position at (0,0) (axis units are metres)

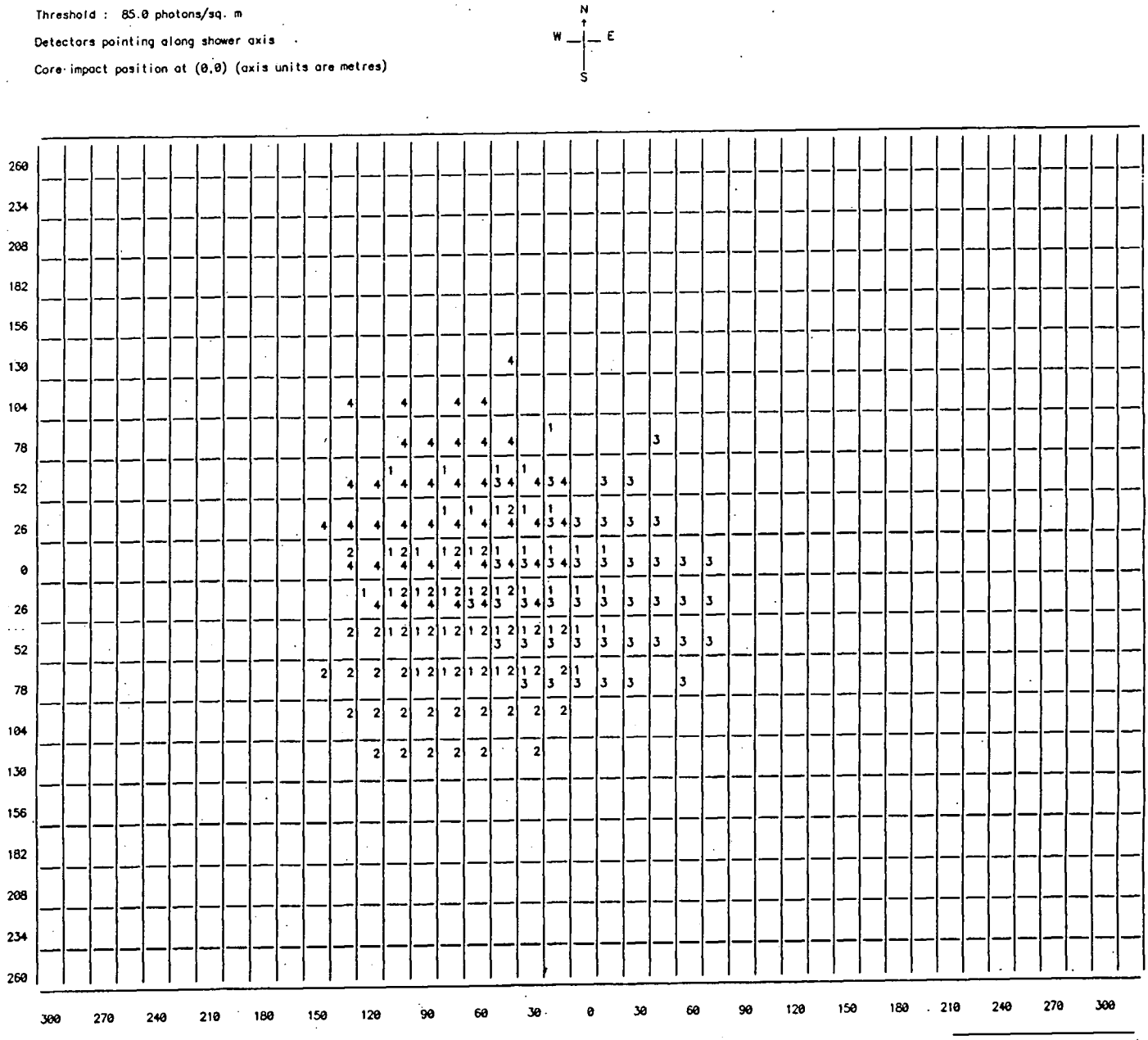

Breakdown of responses

Number of 4-folds = 1					
Number of 3-folds = 18	123(5)	124(7)	234(0)	134(6)	
Number of 2-folds = 27	12(8)	13(8)	14(8)	23(1)	24(1) 34(1)
Number of 1-folds = 64	1(1)	2(21)	3(22)	4(20)	

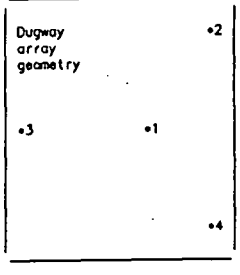

Figure 4.5d Map of Array Responses to Vertically Injected 1000 GeV Shower.

the theoretical point of impact of the primary gamma ray, and the numbers along both axes correspond to distance measured in metres. The numbers in each box indicate which of the four detectors would have been triggered by the event if the central detector of the array had been in the position indicated by that box (the presence of the number '1' indicates that detector 1 would have been triggered, and so on). Thus, the presence of all four numbers represents a fourfold detection of the Cerenkov light flash.

The value chosen for threshold of the detectors is variable, and for this work a range of six values, from 25 to 100 photons m^{-2}, was used. This choice was based on the original estimates of the expected sensitivity of the detectors, (70-100 photons m^{-2}) which has been supported by experimental results. Very little signal is detected when observation thresholds greater than 100 photons m^{-2} are employed.

4.5 Results of the Simulations.

One of the most important aspects of these simulations lies in their assistance in understanding the performance of the array of telescopes at different zenith angles. For example, previous workers have suggested that the count rate observed by such detectors should diminish as $\cos^{2.5}(\theta)$, where 'θ' is the zenith angle: it will be shown here that the zenith angle dependence is very much more complicated and is a strong function of the detector threshold, a fact for which there is significant coroboratory evidence in the data obtained at Dugway during 1981 and 1982.

4.5.1 General Characteristics of the Vertically Injected 1000 GeV Simulated Cascades.

The general characteristics of the showers, such as the size of the light pool, vary with the depth of the maximum of the electron-photon cascade. The histogram in Figure 4.6 indicates the range of values for this parameter for vertically injected cascades, with the 'unit' of atmospheric depth being 25.8 gcm^{-2} (that is, the n^{th} bin is centred at a depth of 25.8 x (n - 0.5) gcm^{-2}). From this the most likely depth of maximum is ~270 gcm^{-2}, with the earliest developing event in the database maximising at a depth of ~245 gcm^{-2} and the latest at ~530 gcm^{-2}.

The number of electrons of energy greater than 20 MeV at the maximum varies over the range 500-800, the mean value for the 20 vertical 1000 GeV events standing at ~670. The average number of electrons reaching the observation level (1448 m a.s.l.) is 12, and that of photons 60, but peak values can be as high as 60 and 300 respectively for late developing cascades.

The peak in the recorded photon density is typically > ~100 photons m^{-2} for early and normal shower development rising to > ~400 photons m^{-2} for the latest developing cascades.

The parameter used to define the size of the light pool is the distance from the position of the peak in the recorded photon density to that at which this has fallen to 1/e of its maximum value; this distance is measured in eight compass directions and the mean calculated. Typical radii of light pools for the earliest, an average and the latest developing showers are 110 m, 100 m and 45 m respectively.

Finally, as mentioned previously, the peak in the recorded

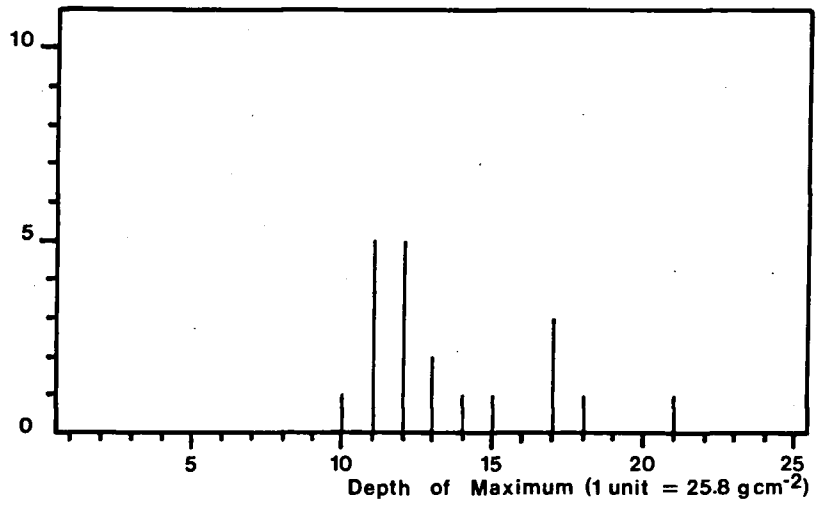

Figure 4.6 Histogram Showing Variation of Depth of Maximum.

photon density is displaced by up to 100 m from the position of core impact. There is no significant evidence for a preferred direction for this displacement, and similar effects have been noted by other workers (Porter, 1973).

4.5.2 General Characteristics of the Non-Vertical Cascades.

For cascades initiated by gamma rays injected at zenith angles of 10° and 35° the peak in the electron number development occurs typically one or two bins earlier than with the vertical showers (the total number of electrons produced is approximately the same). The numbers of electrons and photons reaching the observation plane are more or less unchanged for 10° cascades, but much reduced at 35°, with average values of 1 and 5 respectively.

The peaks in photon density recorded for 10° cascades are similar to those obtained for vertical ones, but at 35° these fall to between 50 and 100 photons m^{-2} for early and normal shower development and $>$ ~130 photons m^{-2} for late developers.

Finally, the size of the light pool increases with zenith angle as expected. At 10° the radii of light pools for early and normal developing showers are typically in the range 120-130 m, while late developers produce values ~70 m. For 35° showers the radii are difficult to estimate according to the convention described in the previous section since the typical light pool no longer has a well-defined peak, being a fairly wide distribution with a large number of small peaks and troughs. Only in the case of late developing cascades is it possible to make a reasonable estimate, and this produces a value of ~115 m.

4.5.3 The Variation of Array Response with Zenith Angle.

To determine the zenith angle dependence of the array response, the number of on-axis counts, averaged over the 20 showers, has been plotted as a function of zenith angle in Figure 4.7, for each of the six thresholds used.

In all cases except that corresponding to the highest threshold, the maximum count rate is observed away from the vertical, contrary to conventional expectations. The explanation offered here for the form of these plots is that there are two competing influences on the telescope response, the relative importance of which depends on the threshold being considered.

As the injection angle of the primary gamma ray is increased, the shower develops at progressively higher altitudes and the Cerenkov signal consequently suffers greater attenuation, resulting in lower photon density in the observation plane.

At the same time, however, the size of the light pool on the ground is increased, due partly to a factor of $\cos^{-1}(\theta)$ arising from the tilting of the light cone with respect to the plane of observation, and moreso due to the lengthening of the cone axis resulting from the development at a greater distance from the observation level.

The net result is that as the zenith angle is increased the light pool diminishes in density but increases in size. At high observation thresholds ($\sim$100 photons m^{-2}) the former influence is expected to dominate, with the latter having increasing effect as the threshold is reduced. At the lowest thresholds ($<$50 photons m^{-2}) it can be seen from Figure 4.7 that the size of the light pool is the principal influence.

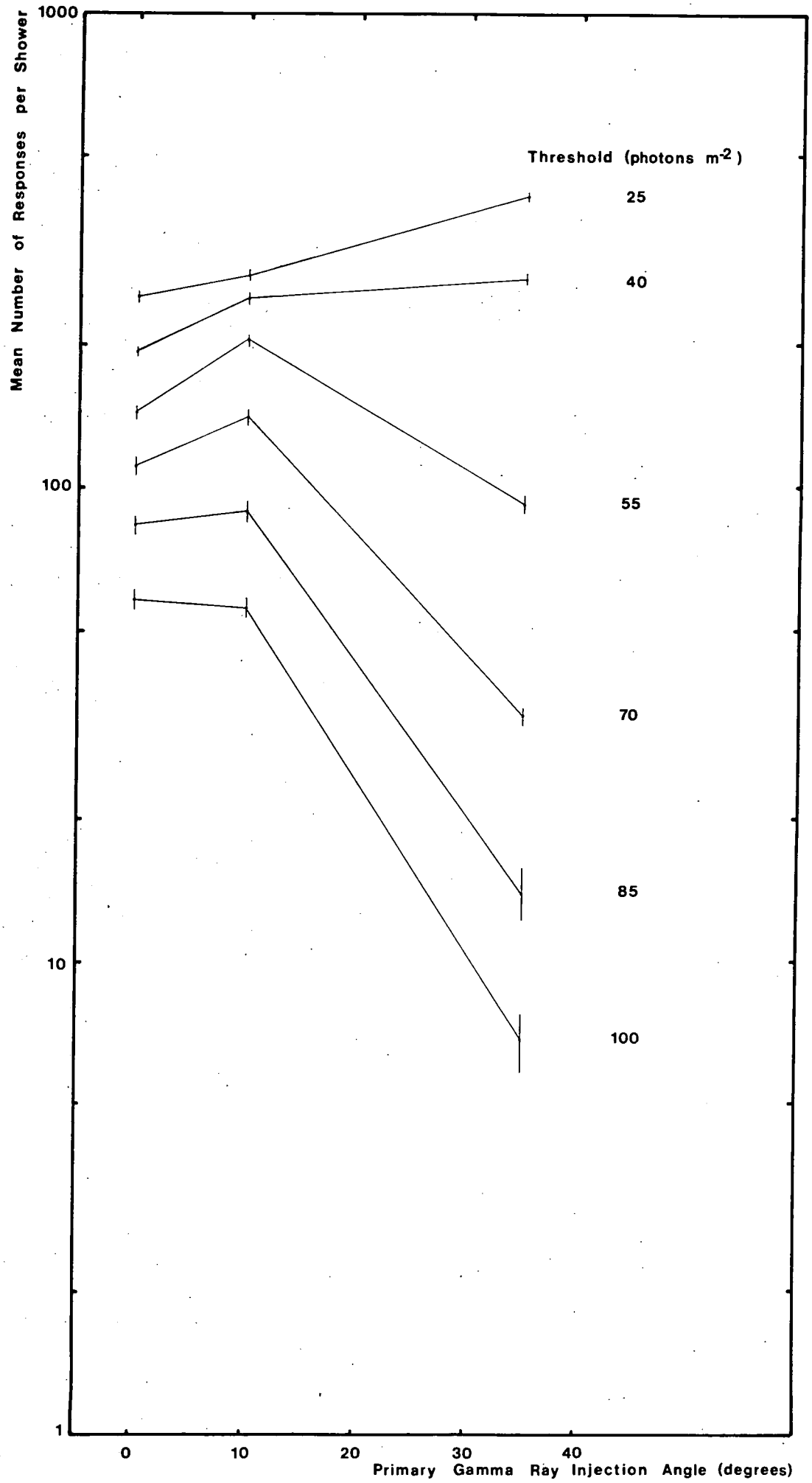

Figure 4.7 Zenith Angle Dependence of Array Response at Each Threshold.

A comparison with actual data, drawn from three nights' observation, is provided in Figure 4.8. The selection of the nights of 22 and 25 August and 14 October 1982 was based upon three criteria:

1. On each night the source (Cygnus X-3) was tracked continuously over the entire range of zenith angles pertinent to the simulations.

2. The sky conditions were excellent throughout.

3. No significant excess count was detected at any phase, indicating that there were no sources emitting.

In Figure 4.8 the total number of counts detected by the array of four telescopes is plotted against zenith angle; each data point repesents 30 minutes data, the point being plotted at the average zenith angle for that period. For two of these plots the maximum observed count occurs at $\sim 5°$, while for the third the response is fairly flat out to $\sim 20°$. According to the simulated responses of Figure 4.7 these correspond to observation thresholds of between 70 and 100 photons m^{-2} in agreement with values derived from calibrations. It should be noted that in the simulation of the response of the array the detectors are all assumed to have the same threshold, whereas the real telescopes span a range of sensitivities as noted in Chapter 3 (section 3.14).

4.5.4 Single and Multiple Detector Responses.

The relative contributions of single and multiple detector responses to the total number of counts are plotted as a function of zenith angle in Figures 4.9a to 4.9f, for each of the six

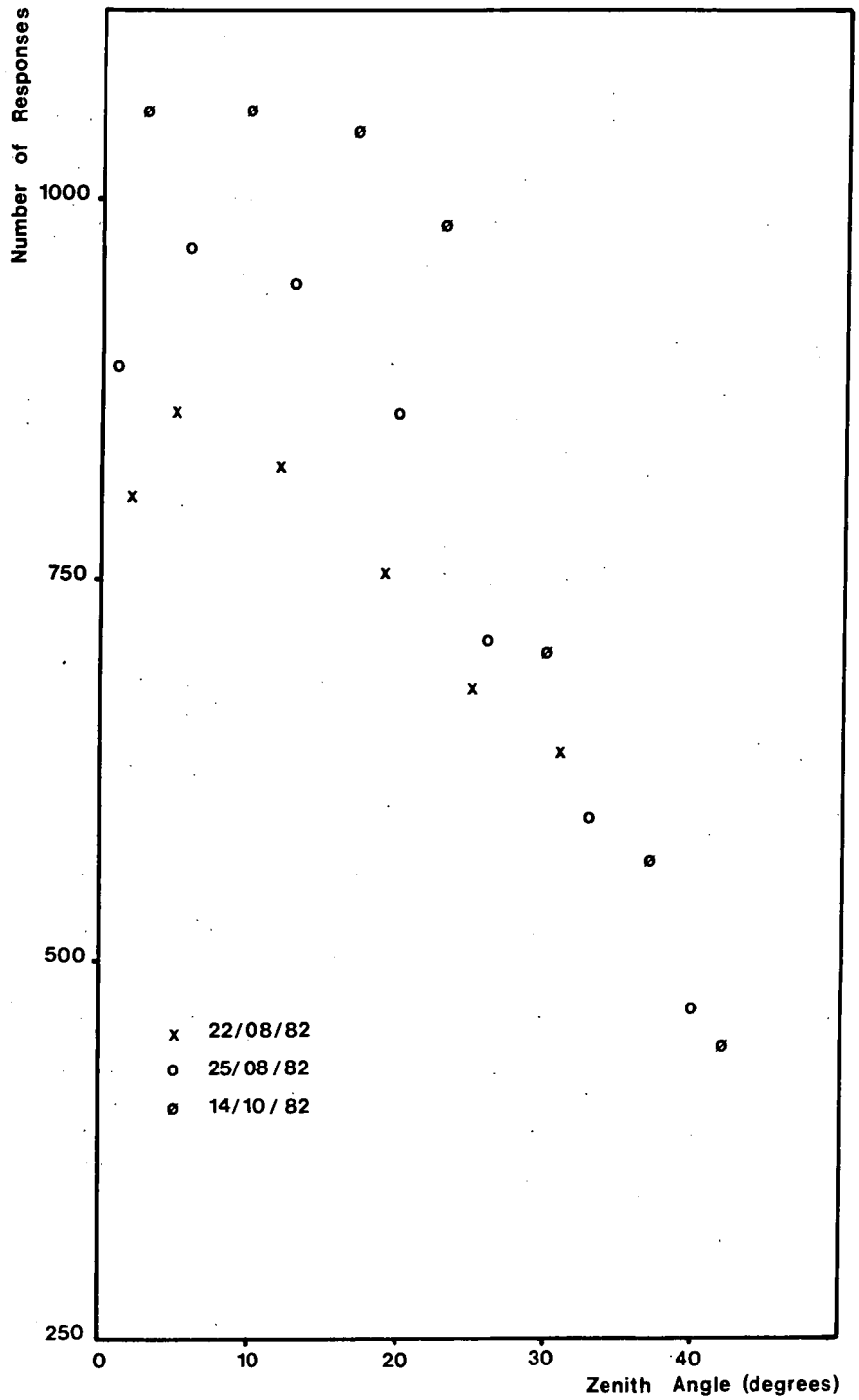

Figure 4.8 Zenith Angle Dependence of Array Response.

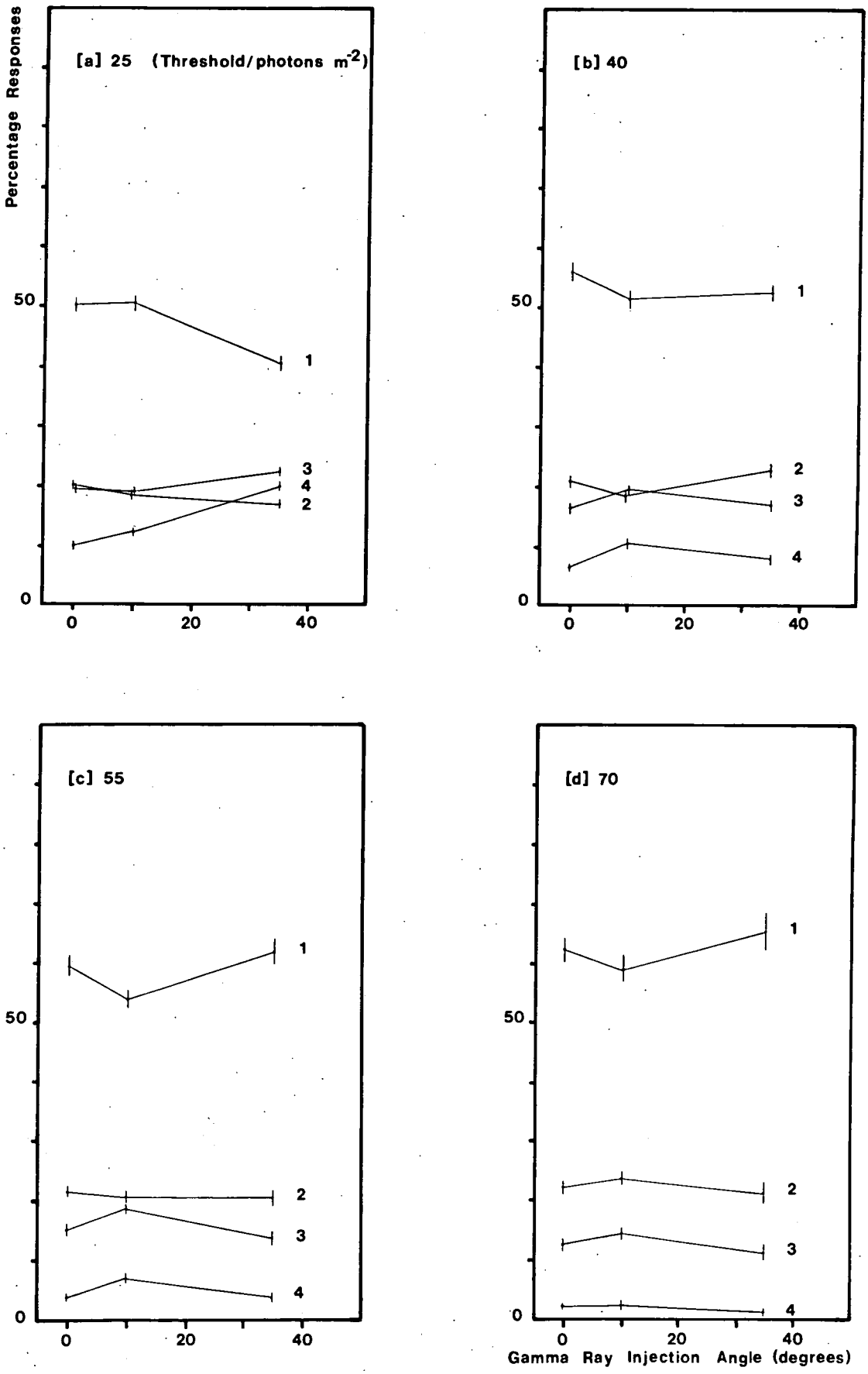

Figure 4.9 Angular Dependence of Responses at Each Threshold.

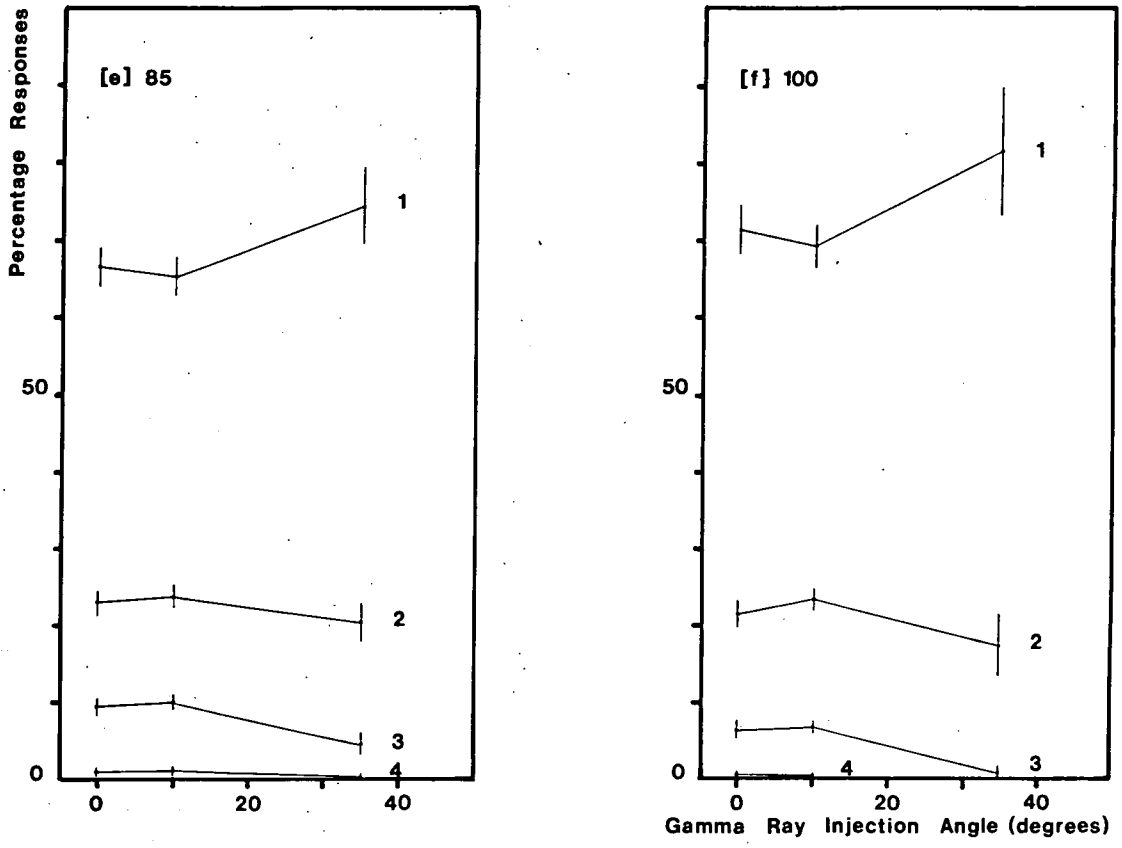
Percentage Responses
[e] 85
[f] 100
1
2
3
4
50
0
0
20
40
Gamma Ray Injection Angle (degrees)

Figure 4.9e,f

density thresholds chosen.

In the light of the results discussed in the previous section, these results are not surprising. At the higher thresholds (Figures 4.9e and 4.9f) the variation of the relative responses with zenith angle is more or less what would be expected from this previous work; as the injection angle is increased the light is more attenuated and consequently the number of onefolds rises at the expense of multiple-fold responses. At lower thresholds, however, once again the increase in size of light pool becomes progressively more significant, leading ultimately, at the lowest threshold (Figure 4.9a), to the case where onefold and even twofold responses diminish, allowing the higher multiplicity responses to increase in number.

Once again, comparison with experimental results is useful, these being two graphs (Figures 4.10a and 4.10b), the first based on 1981 data and the second on that recorded in 1982, in which the percentages of single, two, three, and fourfold responses are plotted against the zenith angle at which the observations were made. In 1981 the array comprised one low threshold, two medium threshold and one high threshold detector. In 1982 the sensitivity of the array was improved by more rigorous mirror alignment and operating at higher PMT gain, the principal benefit being the increase in sensitivity of one of the medium threshold telescopes resulting in two low threshold channels.

The effect of this improvement in sensitivity is most marked at zenith angles greater than $\sim 20^{\circ}$ where the percentage of multiple-fold responses is maintained for much longer. Comparison with the results in Figures 4.9a to 4.9f is encouraging. The 1981

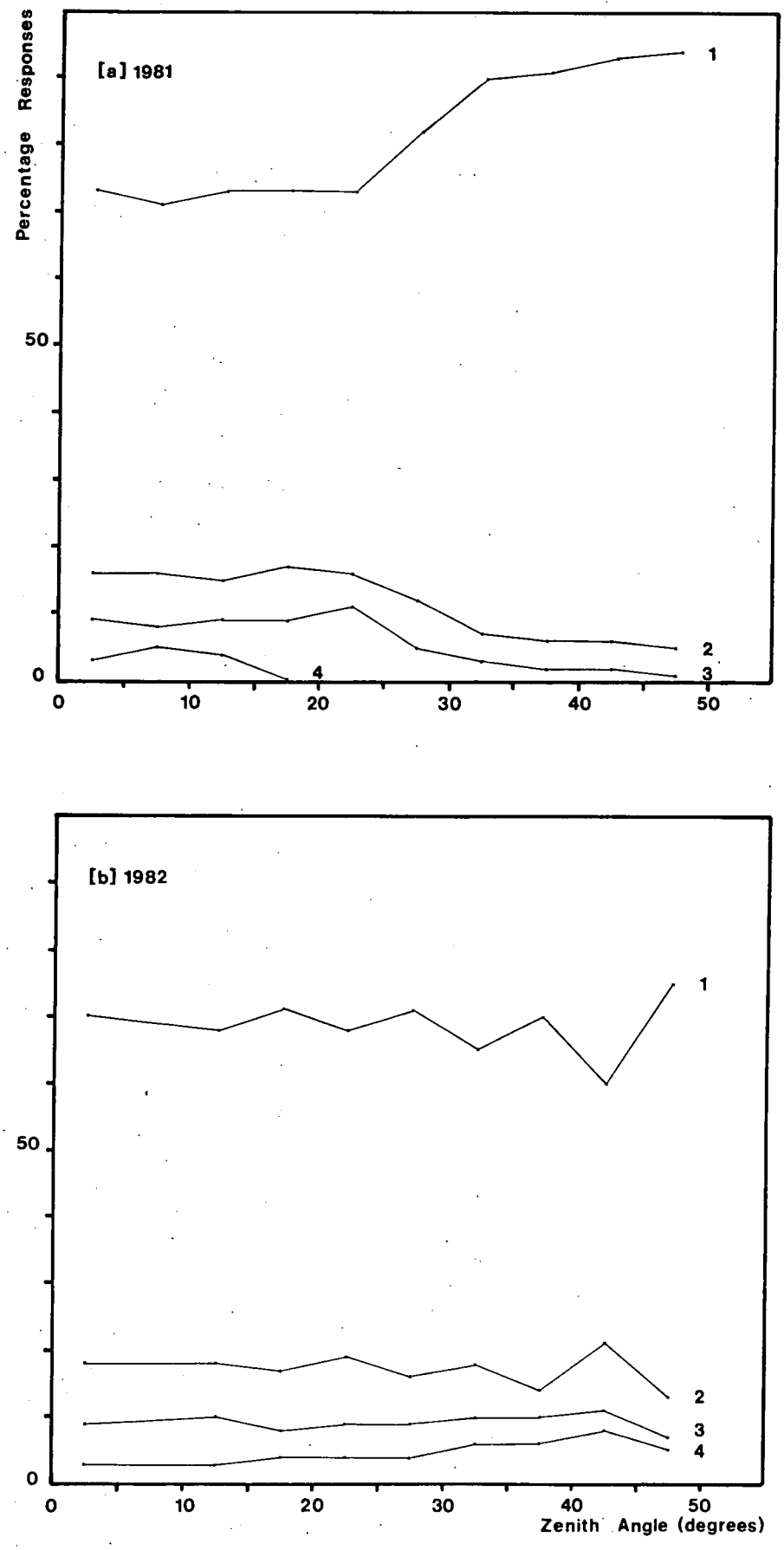

Figure 4.10 Distribution of Single and Multiple-Fold Responses for 1981 and 1982.

data is similar in form to the plot at 100 photons m^{-2}, whereas the 1982 data is more like that at 70 photons m^{-2}. There is a slight discrepancy in that the share of onefold responses is higher and that of twofold and threefold correspondingly lower for the simulated cascades that for the real data, but this may be due to the non-uniform sensitivities of real telescopes at Dugway.

4.5.5 The Response of One or More Detectors as a Function of Threshold.

The number of responses of one, two, three or four detectors, expressed as a percentage of total response, is plotted in Figures 4.11a, 4.11b and 4.11c, as a function of threshold, for the zenith angles in use.

The general characteristic is of a steady increase in the percentage of onefolds at the expense of the higher fold numbers. This is entirely expected, since the light pool is effectively reduced in size as the threshold is increased.

There is, however, an unusual feature, namely the behaviour of the twofold curve. At 0° injection angle, the percentage of twofolds is just greater than that of threefolds at the smallest threshold: thereafter the difference between them increases. At 10° the percentage of the latter is marginally greater than that of the former at low thresholds, with the crossover point occurring between 40 and 55 photons m^{-2}, and the effect is even more pronounced at 35° injection angle. This may be explained by similar arguments to those used in the preceeding section, namely that at sufficiently low thresholds the effect of the greater size of the light pool at increased injection angles outweighs the

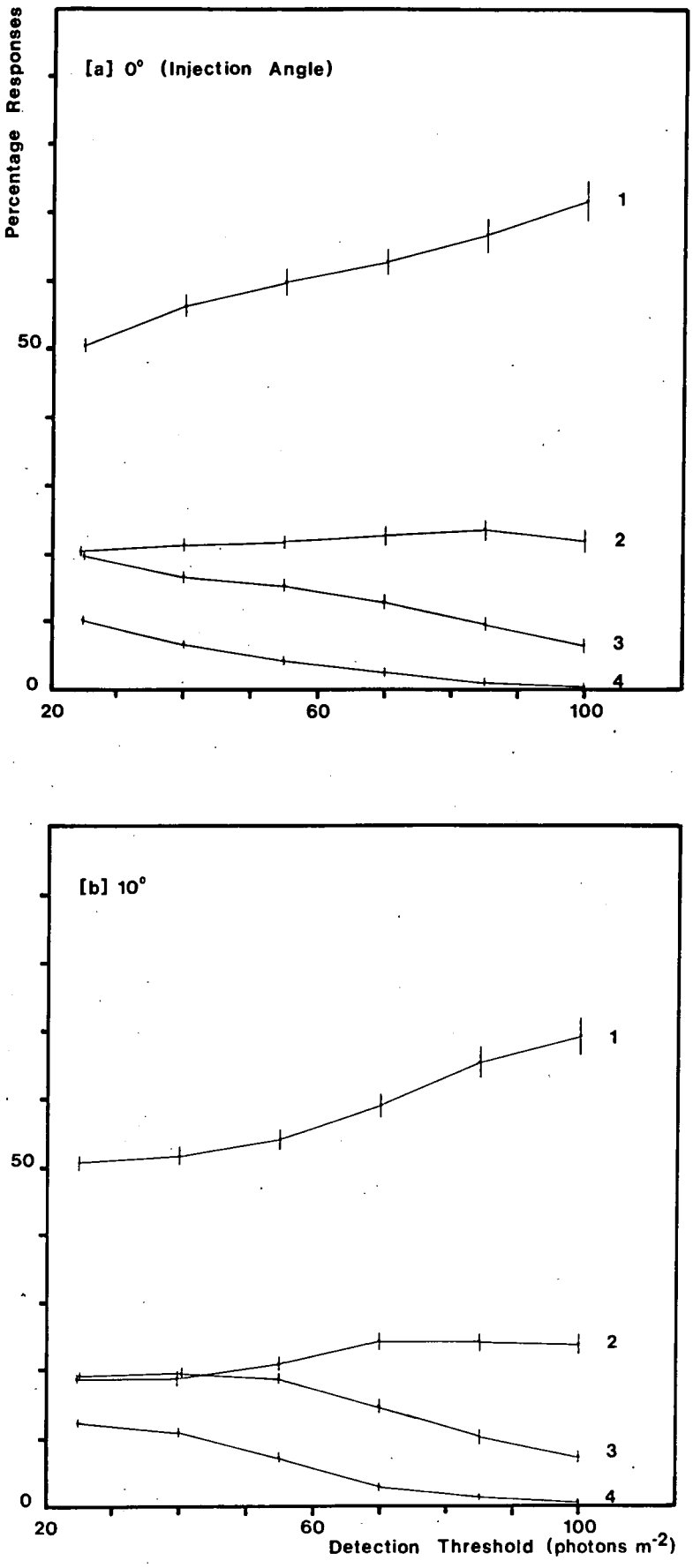

Figure 4.11 Threshold Dependence of Responses at Each Injection Angle.

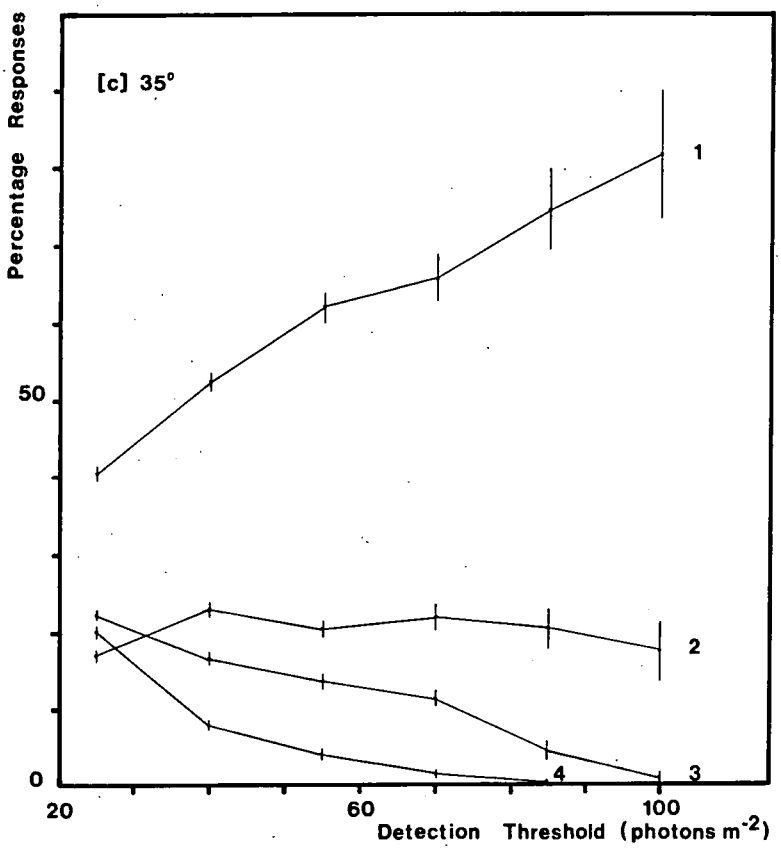
[c] 35°
Percentage Responses
50
0
20
60
100
Detection Threshold (photons m-2)
1
2
3
4

Figure 4.11c

corresponding reduction in photon density in the observation plane.

4.5.6 The Computed Aperture Function.

The computed telescope aperture functions were obtained by calculating the number of responses of the detector matrix for each 1000 GeV shower (see Figure 4.5) as a function of the offset angle between the arrival direction of the primary gamma ray and the pointing direction of the telescopes. The results were integrated over all showers at each zenith injection angle and for each of the selected observation thresholds.

Curves were fitted to the data points using a function of the form

$$y(x) = A \exp(-x^p/a) \qquad (4.15)$$

where y corresponds to the number of responses at an offset angle x, expressed as a percentage of the total number of responses. The values of the parameters A, a and p are fixed by the values obtained for y at 0, 1 and 2 degrees offset respectively: the value of the FWHM may be obtained by substituting y=A/2 into this equation. (Aperture functions for which $A < y(1)$ have a more complicated functional form than that described by equation 4.15 and were therefore fitted "by eye".) The results are plotted in Figures 4.12a, 4.12b and 4.12c as single-sided functions (the responses were found to be symmetrical for negative and positive values of x, and were combined to give improved statistics). These functions are seen to be approximately Gaussian, with typical values of p falling between 2 and 3 (equation 4.15 reduces to

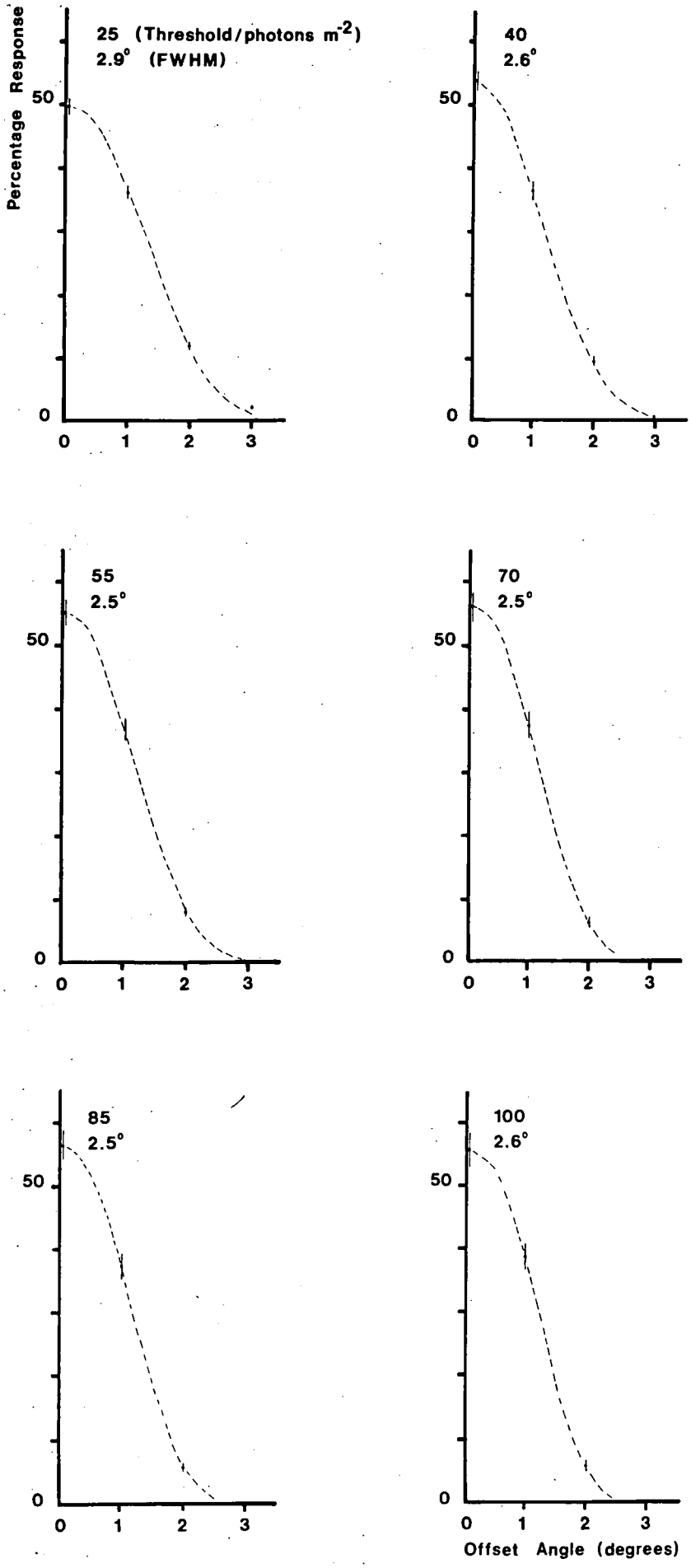

Figure 4.12a Aperture Functions for Cascades Initiated by Gamma Rays Injected at 0°.

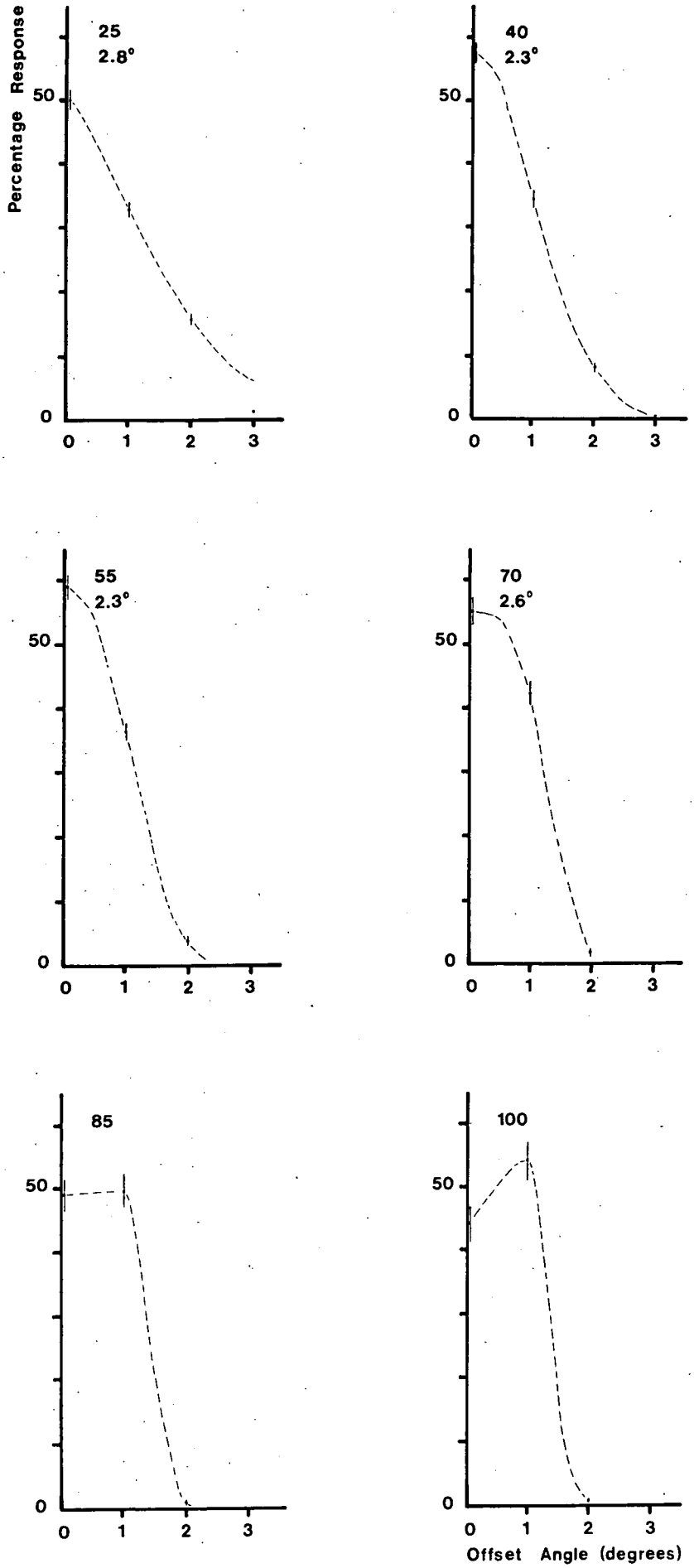

Figure 4.12 b 10° Cascades.

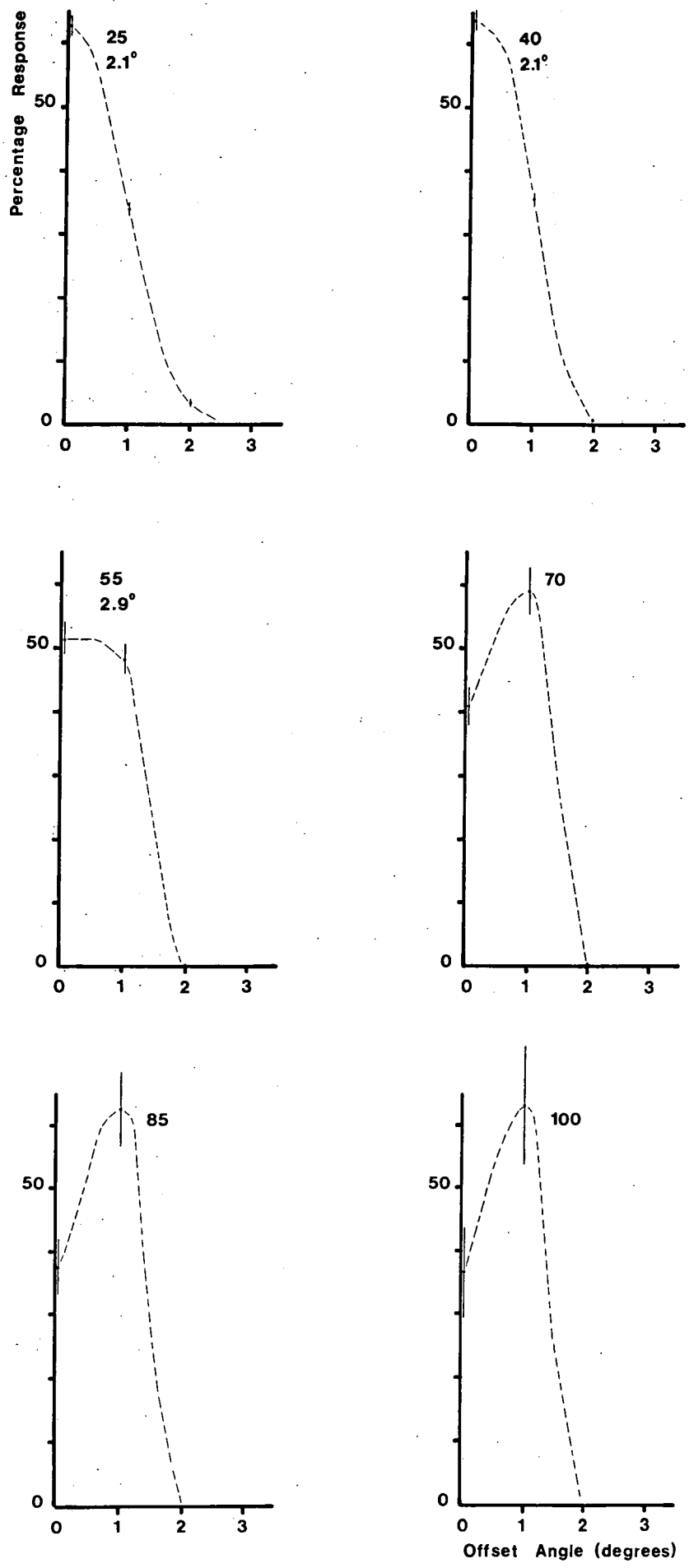

Figure 4.12c 35° Cascades.

Gaussian form when p=2).

The most important fact is that the geometric aperture (1.7° FWHM) is increased owing to the finite size of the light spot to a value in the range 2-3°. The general characteristic is of an aperture function whose width and shape varies with both threshold and injection angle. It will be shown that these two quantities are closely related, which is not unexpected, and that this has important consequences regarding the interpretation of an experimental determination of the aperture of a telescope.

In Figure 4.12a the aperture functions obtained for vertically injected showers are presented. The main characteristic is that the aperture function narrows as the observation threshold increases. At the lowest threshold considered (25 photons m^{-2}) it has the value of ~2.9°, which is reduced to ~2.5° at a threshold of 55 photons m^{-2}. Thereafter no appreciable further reduction is seen, and in fact at a threshold of 100 photons m^{-2} there is even an apparent widening to 2.6°.

The corresponding results for injection angles of 10° and 35° are presented in Figures 4.12b and 4.12c respectively. At 10° the width of the aperture function reaches its minimum value (2.3°) at a threshold of 40 photons m^{-2}. From 70 photons m^{-2} upwards the function is widening again, and at 85 photons m^{-2} the peak response appears at 1° offset. Moving on to 35°, a similar pattern is seen, but now the aperture function is at its narrowest (2.1°) at 25 photons m^{-2}, and the shift in the peak response position occurs at still lower thresholds.

In addition to considering the total array response in this way, the differences between aperture functions corresponding to

single and multiple-fold telescope responses were investigated. In Figure 4.13 the results derived from the 20 vertical 1000 GeV cascades, and using an observation threshold appropriate to the actual array (70 photons m^{-2}), are given. The aperture function is seen to narrow as fold-number increases from 2.8° for onefold responses to 1.7° for fourfold responses. The changes seen in width and shape of these functions are expected from the previous findings, since in effect an increase in fold-number is equivalent to an increase in threshold.

Experimental evidence, using the fast inter-detector timing technique described in Chapter 3 (section 3.12.5), (Dowthwaite *et al*, 1984a) has indicated that the gamma rays from a source have a spread of only ~1°, whereas the CR protons are, of course, isotropic. If the aperture functions in Figure 4.13 are examined with this in mind it may be seen that the higher fold-number responses ought to be richer in gamma rays than the lower ones, since a greater percentage of these showers are detected within 0.5° of the direction of the source (assumed to be at 0° offset).

This is supported by the light curves given in Figures 4.14a and 4.14b (*ibid.*), formed from onefold and twofold telescope responses respectively, using data recorded on the Crab pulsar during 1982-1983, where an excess in counts is seen at the phase of the radio main pulse. This excess, while observed at better than the 3 σ level of significance in both datasets, is seen to be stronger by a factor of ~2 in the data of Figure 4.14b than for those of Figure 4.14a, a 100% improvement in S/N ratio.

This is somewhat larger than the prediction from the simulations, which suggests ~ 27% improvement only. This prediction

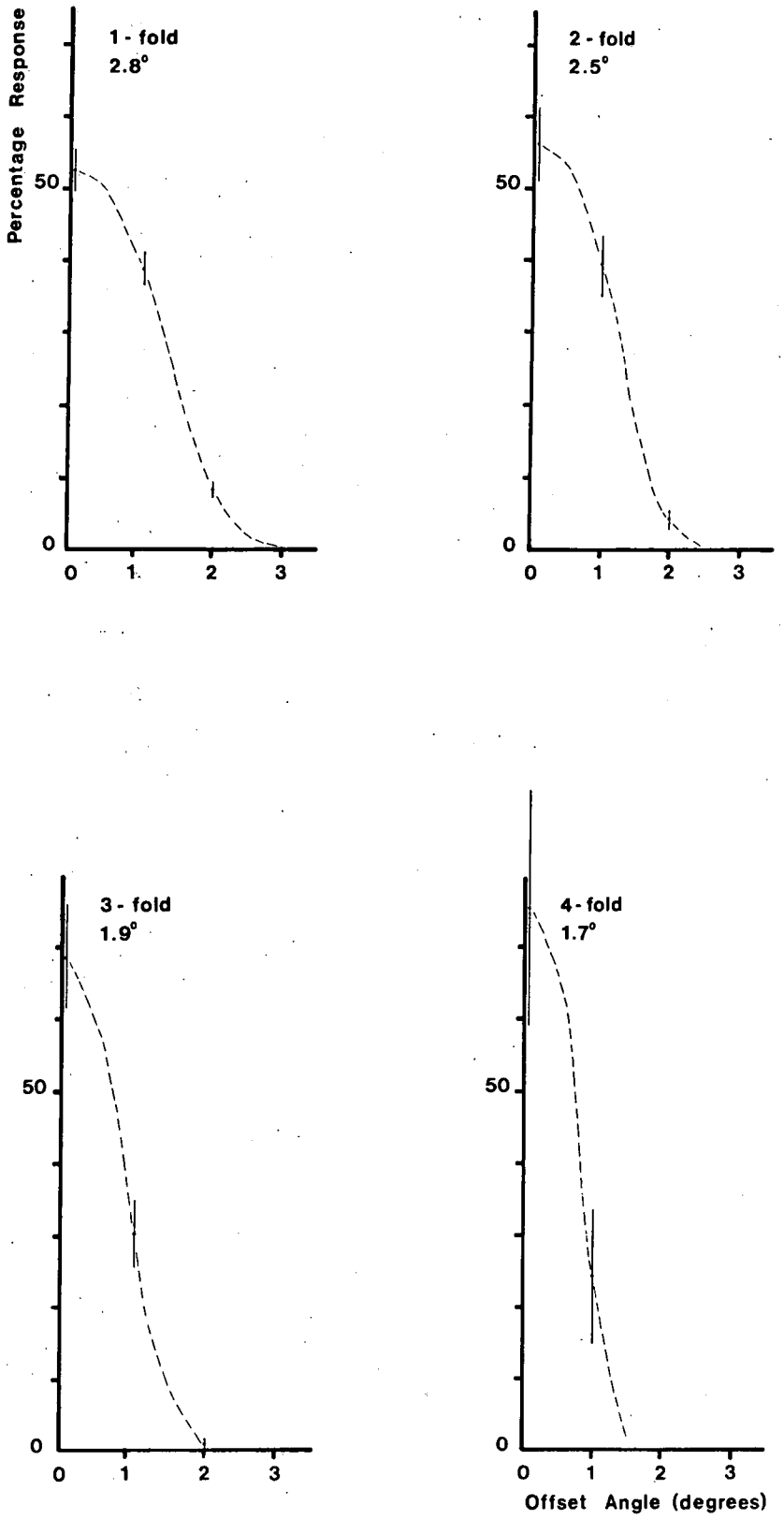

Figure 4.13 Aperture Functions for Vertically Injected Cascades Using an Observation Threshold of 70 Photons m^{-2}.

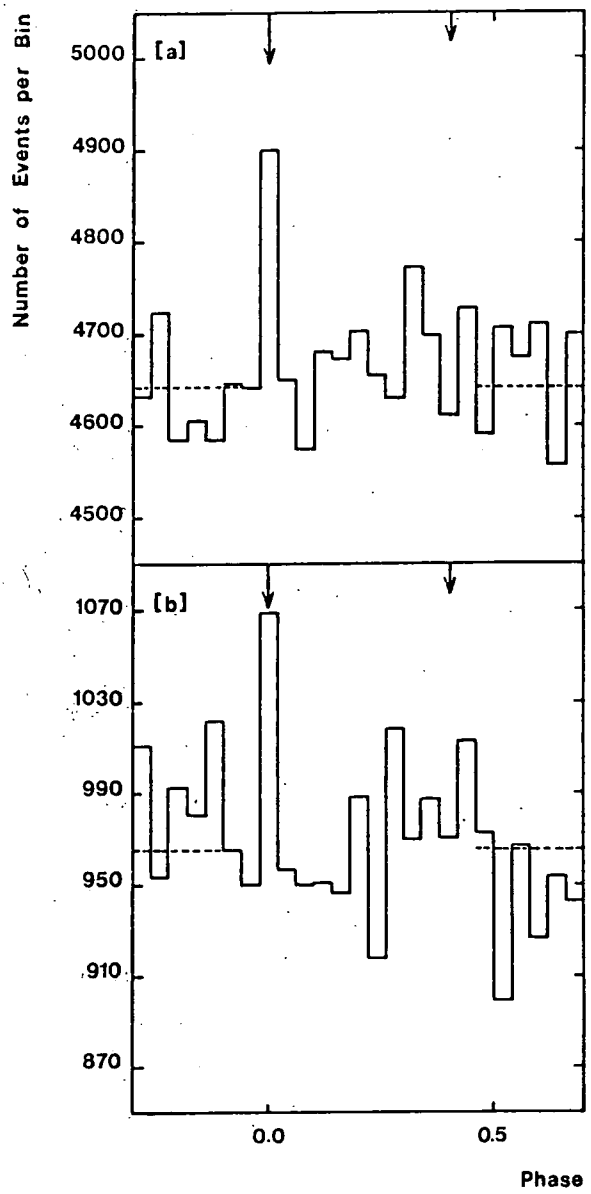

Figure 4.14 Light Curves for All Events Recorded from PSR0531 in November 1982 which Initiated [a] Onefold and [b] Twofold Telescope Responses.

was obtained by considering the aperture function in three dimensions and calculating the volume enclosed for both onefold and twofold responses. The total volume enclosed was considered to be proportional to the noise from the isotropic CR background, while the volume enclosed by the aperture function within 0.5° of the axis corresponds to the gamma ray signal. A comparison of the two S/N ratios so obtained leads to the prediction above.

This treatment makes several assumptions, however. The first is that the aperture function for protons will be the same as that obtained here for gamma rays; clearly if it were broader it is expected that the enhancement would be greater.

Secondly, only 1000 GeV gamma rays have been considered for this treatment. In reality, twofold responses will tend to result from higher energy gamma rays than onefolds, and any difference in the slopes of the spectra for gamma rays and the CR background would therefore affect this result.

A third assumption, mentioned in an earlier section, is that the telescopes are all of equal sensitivity, which is not the case in reality, and this too may have an effect.

Nevertheless the important fact is that the prediction from the simulations of an improvement in the S/N ratio is borne out by the observation of an established gamma ray source. It is expected from Figure 4.13 that a further enhancement would be obtained by considering threefold or fourfold telescope responses alone, but the number of these in the data recorded in 1982-1983 is too small to enable the detection of any significant effect.

4.6 A Single 'Typical' Gamma Ray Initiated Cascade Injected at 20°.

A single 1000 GeV cascade was produced using an injection angle of 20° to give an indication of the variation of shower characteristics between 10° and 35°, the lack of computing time precluding the production of a full set of 20 showers. The cascade selected was the one that most closely resembled the 'average' shower of the dataset at other injection angles, although it was not possible to find one which was truly representative in all respects.

The analyses described in sections 4.5.2 to 4.5.6 were repeated for this individual 20° simulated shower. The results support the previous ones, displaying similar trends, but their usefulnes is limited owing to their poor statistical value. Future plans include the production of a full set of 20° cascades.

4.7 Conclusions.

The most outstanding feature of the simulation results is the insight into the dependence of the telescope response on observation threshold. Figure 4.7 illustrates this, showing that with a sufficiently low detection threshold, worthwhile measurements could be made at much greater zenith angles than previously thought, and, in the case of the lowest thresholds, the count rate may be expected to actually increase with zenith angle.

Related to this is the unexpectedly high level of multiple-fold responses (for which fast timing techniques would obtain) at low thresholds, particularly at the greatest zenith angle, where they constitute ~60% of the signal (Figure 4.11c).

This clearly has important implications for an increased yield of any fast-timing analysis.

The improvement in our understanding of the behaviour of aperture functions is also highly significant. For a system with a geometric aperture of 1.7° and a threshold in the range 70-100 photons m^{-2} (as seems appropriate for the Dugway telescopes), the effective aperture has values of 2.5° FWHM for θ=0°, increasing to 2.6° FWHM at 10° zenith angle and developing an off-axis peak response at 35°. If true, this latter fact would suggest that for observation at large zenith angles (> ~40°), a source may appear as an excess in count rate before and after transit through the centre of the field of view.

With a much lower observation threshold (~40 photons m^{-2}), the aperture would be expected to reduce in width with increasing zenith angle (2.6°, 2.3° and 2.1° for zenith angles of 0°, 10° and 35° respectively), giving rise to an improvement in the S/N ratio. The evidence for improvement due to a narrowing of the aperture has already been noted in the analysis of data recorded on the Crab pulsar, with the observed enhancement of a positive effect when considering only twofold responses as opposed to broader aperture onefolds (Dowthwaite *et al*, 1984a).

Since the energy thresholds of the Dugway telescopes are above ~1000 GeV, simulated cascades at higher energies, say ~3000 GeV, would prove useful. It may prove possible to produce some showers these energies in the future, and this would enhance the value of the conclusions based on simulations.

CHAPTER 5.

SIMULATION OF THE RESPONSE OF THE WHIPPLE OBSERVATORY CAMERA.

A project has been underway since 1982 to use the 10 m diameter optical reflector at the Fred Whipple Observatory (FWO), at Mount Hopkins in Arizona, to record two-dimensional Cerenkov light images from small EAS. The technique employed was first suggested by Weekes and Turver (Weekes and Turver, 1977), and the preliminary design and expected performance of a camera based on the 10 m reflector was described by Weekes in 1981 (Weekes, 1981).

The potential use of the imaging technique lies in the determination of the arrival direction of the primary gamma ray or proton from an analysis of the isophotal contours of the light spot formed on the camera. The energy of the primary could be estimated by integrating the total light in the shower image. The accuracy of the technique will be limited by fluctuations in EAS development.

This is a collaboration involving workers from six centres. One of these, the Smithsonian Astrophysical Observatory, has already been mentioned as the site of the observations. The camera electronics is provided by a group at University College, Dublin. The imaging analysis is contributed to by groups from the University of Hawaii, Iowa State University and the University of Hong Kong. The University of Durham contribution consists of computer simulations of the response of the camera, which are the subject of this chapter. To begin with, however, the camera will be described briefly.

5.1 The Camera Description.

The camera comprises an array of 2" diameter PMTs mounted in the focal plane of a large (10 m diameter) reflector which is mounted on a computer-controlled alt-azimuth platform.

The 10 m reflector comprises 248 hexagonal, ground-glass elements, each 1 cm thick and 60 cm in diameter. These are front-aluminised with a silicon dioxide overcoating, giving a collecting area of approximately 75 m^2. The focal length is 7.3 m.

The camera head consists of 37 pixels (RCA 4518 PMTs) arranged as indicated in Figure 5.1 (the diagram shows an extra ring of PMTs as considered in the simulations, making a total of 61), with 0.5° between the centres. The full field of view of the camera is 3.5°.

The camera employs fast pulse amplifiers and triggers (LeCroy MVL100), with fast coincidence and master trigger generation. The pulse heights are recorded with QTC units, based on the Dugway experiment, with 8 bit resolution. Relative time is kept with a resolution of 1 μs, and absolute time to ± 0.05 ms. Individual channels are monitored by ratemeter, with rates set at between 0.1 and 1 kHz.

5.2 Operation of the Camera.

A range of selection requirements have been employed. Initially the system is triggered when 3 or more of the inner 7 PMTs register a coincidence; when this happens the signals from all pixels of the camera are recorded.

During a trial period in 1982-1983, using only 200 mirrors on the reflector, whose average reflectivity was 35%, the shower

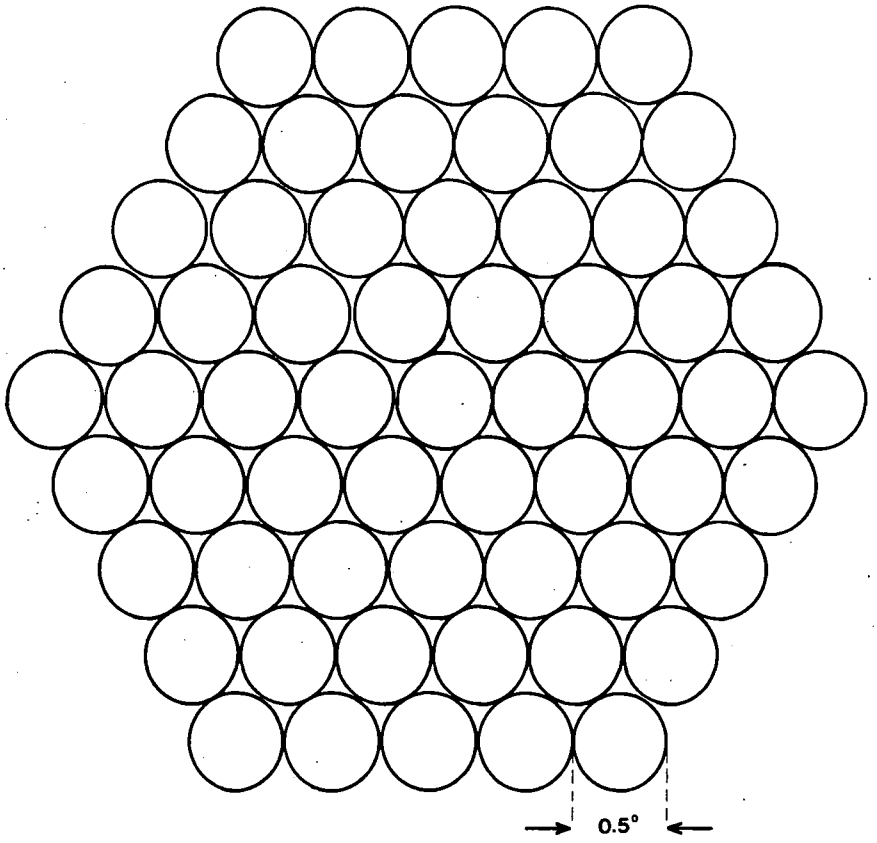

Figure 5.1 The FWO Imaging Camera Head, as Used in the Simulations.

detection rate at the zenith was 1-2 Hz. With a full complement of newly coated mirrors a fivefold improvement on this may be expected.

5.3 The Simulation Program.

The program used to simulate the response of the FWO camera is identical to that described in the preceeding chapter for the Dugway calculations, with different binning routines employed. The aim was to provide a guide to the interpretation of experimental results and to aid the development of image analysis routines to enhance the detection of gamma ray initiated Cerenkov light flashes.

5.3.1 The Binning Routines.

For these simulations 41 detectors of the FWO type were included in a cruciform pattern, centred on the position of core impact (0,0) as shown in Figure 5.2. These were positioned at intervals of 25 m out to 250 m along north, south, west and east directions, so that the variation of the size and shape of the Cerenkov light image with distance and direction from the origin could be investigated.

Each detector in this matrix had a camera head comprising 61 pixels, arranged as illustrated in Figure 5.1. The arrangement is identical to that used in the real camera, with the addition of an extra ring of PMTs to provide further information to aid the optimum use of simulation results.

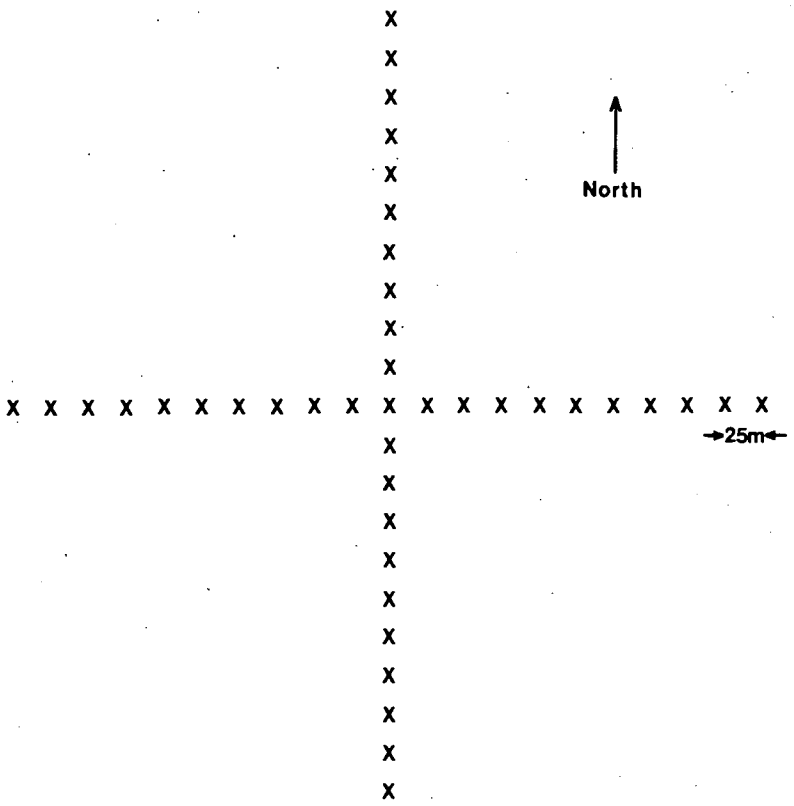

Figure 5.2 Binning Matrix.

5.4 The Whipple Observatory Simulation Database.

Gamma ray initiated showers were simulated for vertically incident gamma rays at three energies, these being 100 GeV, 300 GeV and 1000 GeV; the estimated threshold of the fully efficient camera lies within this range. A summary of the calculated cascades is given in Table 5.1.

As for the Dugway simulations, the information recorded falls into three main categories, the first two being common to both sets of calculations; these were described in Chapter 4 (section 4.4.1). The initial parameters used in the Mount Hopkins calculations are summarised in Table 5.2.

The third category here consists of the computed response of the FWO camera, in units of photo-electrons m^{-2}, as a function of displacement and direction from the point (0,0). This forms the main database for analysis.

In addition, software was written to perform analyses of the images of the type described in section 5.5.

5.4.1 The Response of the Array of Imaging Cameras.

Since the computer code employed for the electron-photon cascade was essentially identical, the FWO simulated showers share the same general characteristics as the Dugway ones, as described in Chapter 4 (section 4.5.1).

An example of the output from a 1000 GeV shower is given in Figures 5.3a,b,c,d and e. These show the response of each pixel in the camera head (in photo-electrons m^{-2}) for cameras positioned at (0,0) and at distances of 100 m from this point along all four axes. Detailed analysis of these results will not be given here,

Table 5.1

Energy(GeV)	Injection Angle(Zen)	No. of Events
1000	0	30
300	0	25
100	0	25

Table 5.2

Primary gamma ray energy = 1000, 300, 100 GeV

Injection angle Zenith = 0.0°

Azimuth = 0.0°

Injection altitude = 29600 m a.s.l.

Observation altitude = 2134 m a.s.l. (FWD)

Energy cut-off to ensure emission = 20.0 MeV

OUTPUT ALONG S-N AXIS, THROUGH ARRAY CENTRE

Output given in photo-electrons
Acceptance is Gaussian (FWHM = 0.25 degs, with cut-off at +/- 0.2 degs)
Detector located at position of core impact

14.44 0.23

4.37 2.04 1.09

20.78 6.88

2.77 46.04 11.03

7.37 102.42 161.70 2.46 1.94 2.81

14.49 39.32 46.78 8.10

3.29 10.28 2.16

Figure 5.3a Response of Imaging Camera to Simulated 1TeV Shower.

OUTPUT ALONG S–N AXIS, THROUGH ARRAY CENTRE

Output given in photo-electrons
Acceptance is Gaussian (FWHM = 0.25 degs, with cut-off at +/– 0.2 degs)
Detector located 100m north of position of core impact

1.60

8.72 0.19

3.03 0.91 2.87

0.20 1.04 0.59 1.98

112.04 10.25

93.90 16.57

1.17 2.13 54.74 20.99

3.89 31.25 2.09

3.99 21.83

Figure 5.3b Response of Imaging Camera to Simulated 1TeV Shower.

OUTPUT ALONG S–N AXIS, THROUGH ARRAY CENTRE

Output given in photo–electrons
Acceptance is Gaussian (FWHM = 0.25 degs, with cut–off at +/– 0.2 degs)
Detector located 100m south of position of core impact

0.41 4.37

1.08 1.42 14.25 22.09

18.21 102.79 32.75 12.67

1.03 197.99 1.79 13.92

Figure 5.3c Response of Imaging Camera to Simulated 1TeV Shower.

OUTPUT ALONG W-E AXIS, THROUGH ARRAY CENTRE

Output given in photo-electrons
Acceptance is Gaussian (FWHM = 0.25 degs, with cut-off at +/- 0.2 degs)
Detector located 100m west of position of core impact

1.95 1.68

11.21 2.53

9.26 5.34

1.76 41.06 1.23

56.08 26.07 13.12 10.30

0.87 41.54

0.48

Figure 5.3d Response of Imaging Camera to Simulated 1TeV Shower.

OUTPUT ALONG W–E AXIS, THROUGH ARRAY CENTRE

Output given in photo-electrons
Acceptance is Gaussian (FWHM = 0.25 degs, with cut-off at +/- 0.2 degs)
Detector located 100m east of position of core impact

0.70

24.12 5.78

1.24 3.75 12.30

35.27 1.32 202.23 37.85 0.61 0.43

0.28 11.80 310.26 5.66

4.15 0.44 22.90 18.90 0.70

10.61 29.87 0.47

12.70 2.94 16.44

Figure 5.3e Response of Imaging Camera to Simulated 1TeV Shower.

but it is noted that, as expected from the calculations for the Dugway experiment, the peak recorded photon density does not generally occur at (0,0). Examples of observed responses to real showers are presented in Figures 5.4a and b for comparison (Weekes, 1984, private communication).

The main difference between the images produced by real and simulated showers is that the former generally have a broader angular distribution of light than the latter, with only ~1% displaying the "tightness" of the calculated cascades. This is currently under investigation, but one possible explanation is that since over 99% of the data will be the result of proton initiated cascades it may be these which are giving rise to the broader images, the tighter ones being of gamma ray origin.

5.5 Gamma Ray Imaging Analysis.

Data analysis routines, including that developed by Stenger at the University of Hawaii (private communication), have been established at a number of collaborating institutions. It is important to subject the simulated showers to the same analysis as real data and the Hawaiian approach has been followed here. Porter (private communication) is also analysing the simulations in the same way as "data input" using the fitting routines developed at University College, Dublin.

To date little success in employing an analysis of either simulated or genuine images to enhance the detection of gamma rays has been reported. A possible cause for the failure to improve the S/N ratio, suggested by the computer simulations, is the uncertainty of ± ~0.5° in the difference between the primary gamma

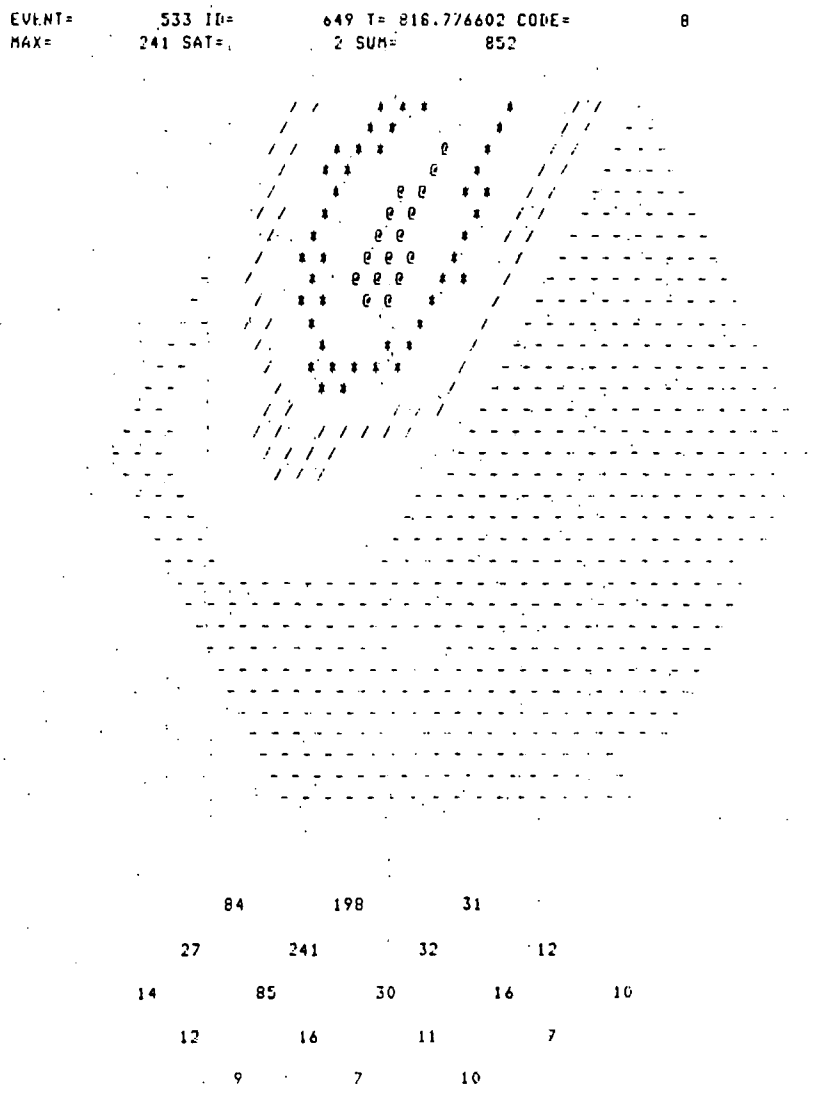

Figure 5.4a Observed Response of Imaging Camera to Real Shower.

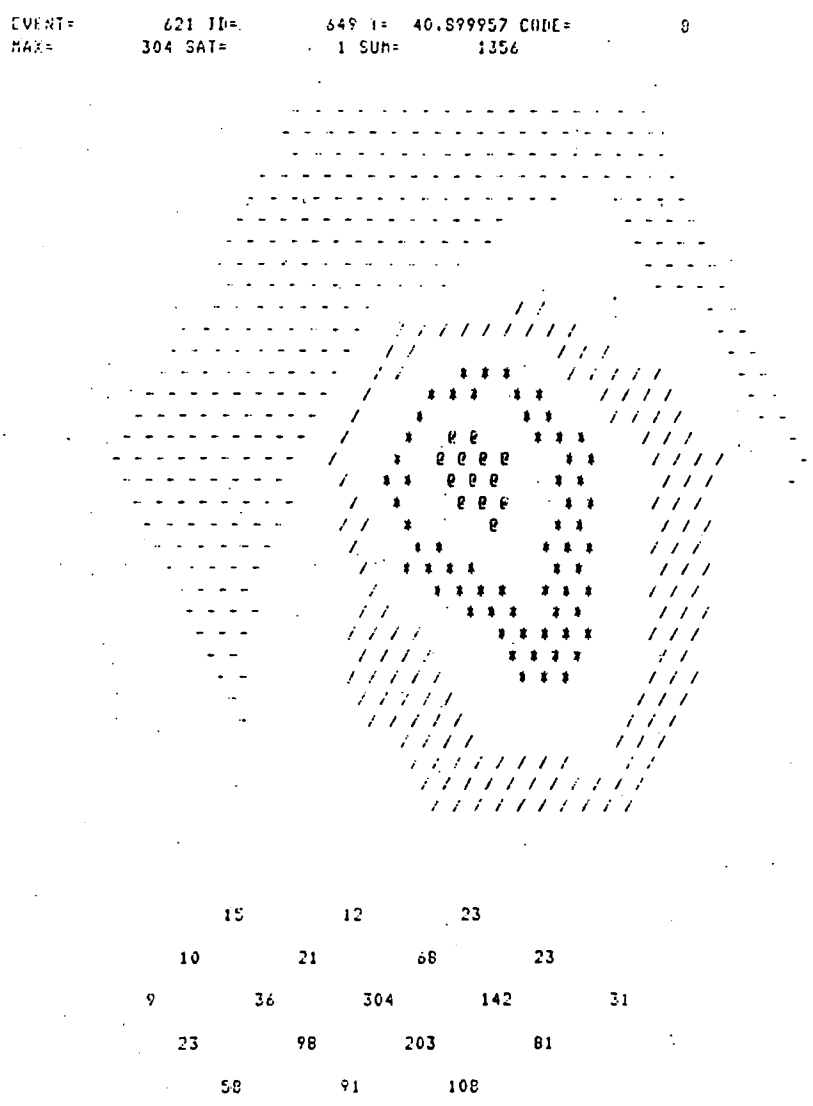
EVENT= 621 ID= 649 I= 40.899957 CODE= 0
MAX= 304 SAT= 1 SUM= 1356
15 12 23
10 21 68 23
9 36 304 142 31
23 98 203 81
58 91 108

Figure 5.4b

ray direction and that of the detected Cerenkov light cascade. The existence of this jitter on any direction derived from an analysis of the ellipticity of the image limits the S/N ratio improvement possible.

The origin of the jitter is at present unknown, but it seems likely that it arises near the beginning of the cascade development. For example, it may be due to early deflections of electrons and positrons by the Earth's geomagnetic field. Recent simulations of 300 GeV showers have been obtained with this field "switched off"; these have produced tighter images of the Cerenkov light with less jitter than before. This suggests that the effect of the geomagnetic field is but a minor part of the cause of the predicted jitter.

5.5.1 Image Reconstruction.

The first step in the image reconstruction process is to determine the centroid and shower axis from the PMT outputs. In the following treatment outlined by Stenger (private communication) equations X_i and Y_i are the coordinates in degrees of PMT_i, with the central PMT situated at the origin, and n_i is its output in photo-electrons. The coordinates of the centroid (X_c, Y_c) are

$$X_c = \frac{1}{N} \Sigma n_i X_i \qquad (5.1)$$

$$Y_c = \frac{1}{N} \Sigma n_i Y_i \qquad (5.2)$$

where

$$N = \Sigma n_i .$$

Having calculated the centroid position, the coordinates are translated to a frame of reference with the origin at this position (Figure 5.5).

Using these new coordinates (x,y), the principle axis (OX") is defined by

$$\theta = \frac{1}{2}\,\mathrm{atan}\left(\frac{2I_{xy}}{I_{yy}-I_{xx}}\right) \qquad (5.3)$$

where

$$I_{xx} = \Sigma n_i x_i^2 \qquad (5.4)$$

$$I_{yy} = \Sigma n_i y_i^2 \qquad (5.5)$$

$$I_{xy} = -\Sigma n_i x_i y_i. \qquad (5.6)$$

and a further coordinate transformation is made; the axis Ox is rotated so that it lies along OX". The shower direction can be either along OX", as shown in Figure 5.5, or at right angles to it. In order to establish which is the case, the second moments are calculated:

$$I''_{xx} = \Sigma n_i (x_i'')^2 \qquad (5.7)$$

$$I''_{yy} = \Sigma n_i (y_i'')^2 \qquad (5.8)$$

If $I''_{yy} > I''_{xx}$, the shower axis is taken to be along OY". Finally the shower coordinate system (x',y') is defined so that the positive x' direction is along the shower axis, in the direction of the longer tail; this is determined by choosing the sense of x' so that the third moment

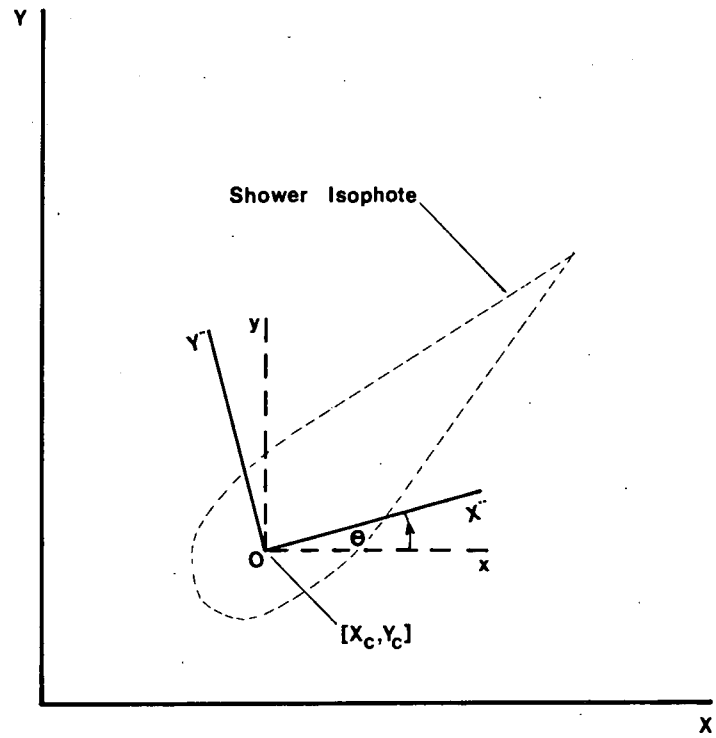

Figure 5.5 Frames of Reference Used in Image Analysis.

$$I'_{xxx} = \Sigma n_i (x_i')^3 \qquad (5.9)$$

is positive.

By this stage a reasonably good reconstruction has been obtained. Further software exists to improve the reconstructed image, in the form of least squares fitting routines, if required.

An example of the results of using this image reconstruction routine is given in Figure 5.6. This shows the image produced by a simulated 1000 GeV shower, with units of degrees along the axes, and PMT responses given in photo-electrons.

5.5.2 Image Analysis by the University of Hong Kong Group.

P.K. MacKeown of the University of Hong Kong has conducted an analysis of the simulation results (private communication), and a summary of the important conclusions is presented here. In this work it was assumed that only the central 19 PMTs were functioning in line with the initial state of the camera. In addition, in order for the camera to be considered to have triggered, it was required that at least 3 of the central 7 PMTs each detect >10 photo-electrons.

In Figure 5.7 the variation of the diplacement of the centroid of the reconstructed image from the centre of the camera with core distance (R_{core}) is plotted and indicates that the most central images are obtained for values of R_{core} around 50 m. Consistent with this is the plot in Figure 5.8 of total recorded photon density as a function of R_{core}, which peaks at 100 m.

A measure of the angular spread of the image is obtained by calculating the ratio of the signal recorded by the central 7 PMTs

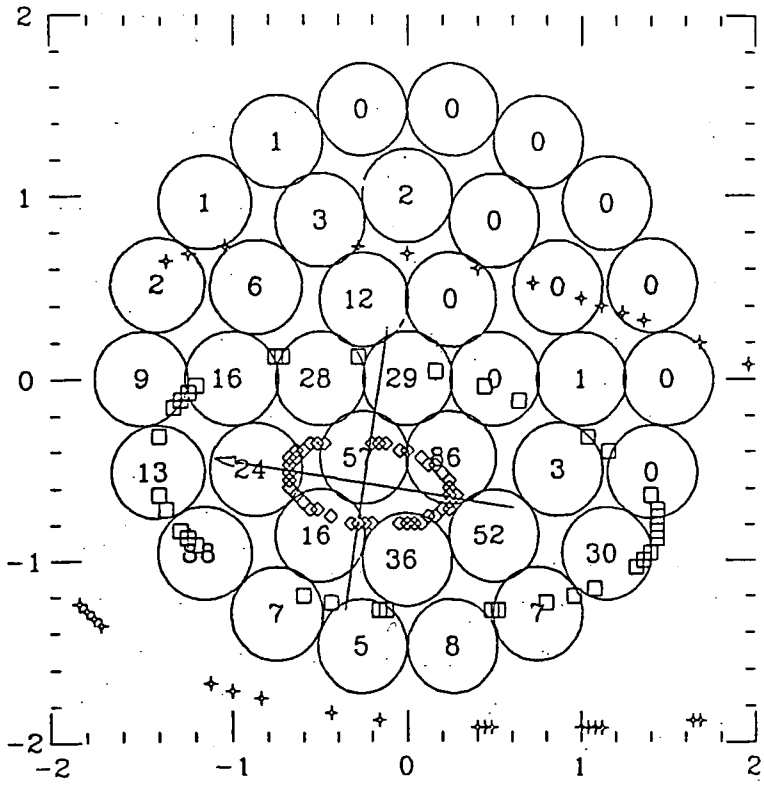

IMAGE PARAMETERS	
MODEL	6
IER	0
CHISQ	0.00
XO	−0.25
YO	−0.58
PEAK	88.00
WIDTH	0.71
LENGTH	0.86
AXIS	351.04
POWER	3.00
ENERGY	718.53
ZENITH	0.63
AZIMUTH	351.03
ASPECT	104.28
IMPACT	0.61

Figure 5.6 Reconstructed Image of Simulated Shower.

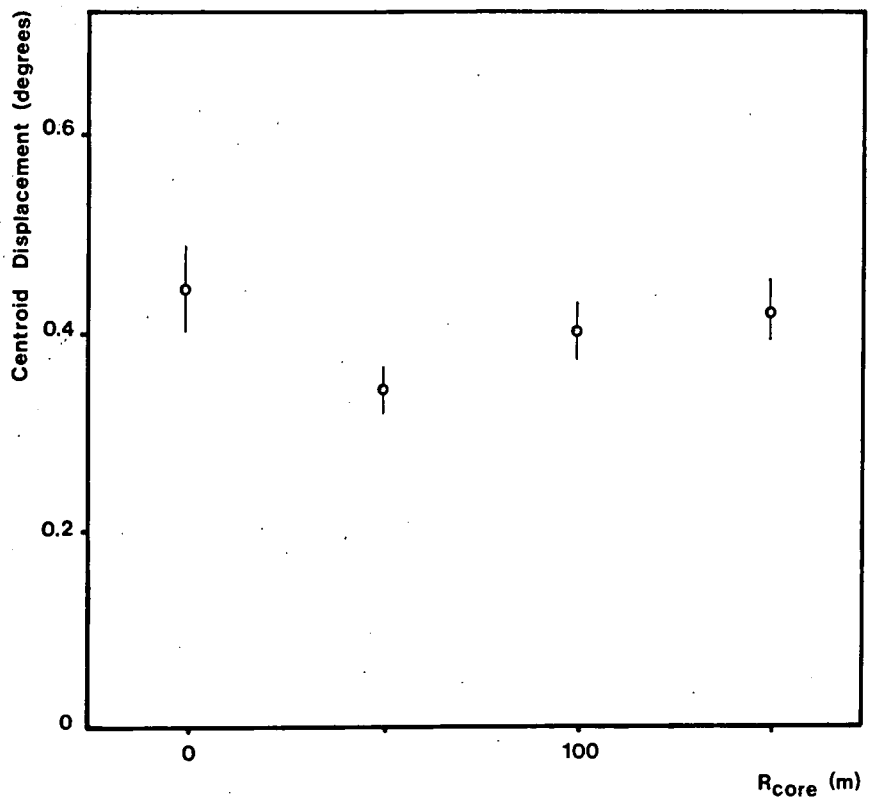

Figure 5.7 Variation of Centroid Displacement with Core Distance.

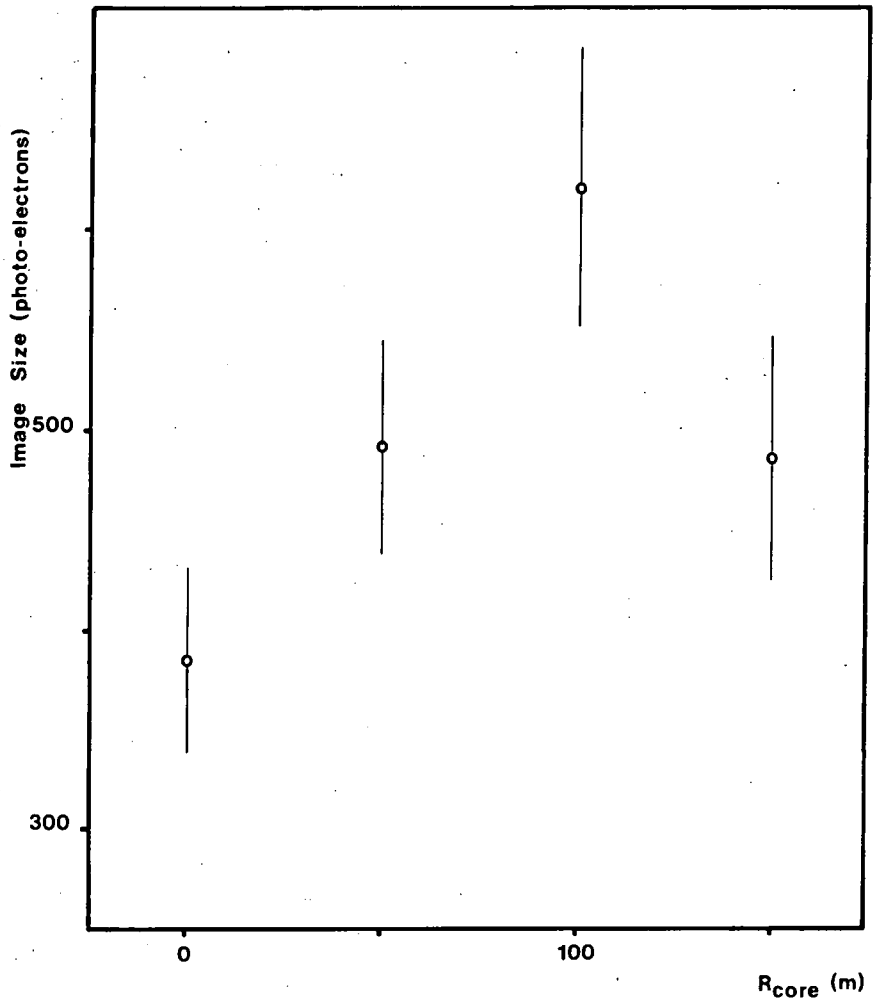

Figure 5.8 Variation of Image Size with Core Distance.

to that of the outer 12. The dependence of this quantity on R_{core} has been plotted in Figure 5.9, from which it may be seen that in general the broadest distributions occur for the smallest values of R_{core}; there is a modulation in this plot owing to the centroid moving out at large values of R_{core} resulting in less light falling on the inner PMTs.

Finally in Figure 5.10 the variation of detection efficiency is plotted against R_{core}. The steady reduction of this quantity as R_{core} increases shows that triggering is not just a function of the size of the light pool, which maximises at 100 m (Figure 5.8) but depends on the pattern of light in the camera.

5.6 Conclusions.

There is still much work to be done to understand fully both the simulations and, in turn, the real data. To this end further simulations are being produced. Included in these are calculations employing the same basic arrangement of the camera head but with the scale halved, to give PMT apertures of 0.2°, in order to obtain more detailed information on the angular distribution of light.

One important difference between calculated and real showers is in the angular spread of the image, with the latter tending to have broader images than the former (Weekes, 1984, private communication). One possible explanation based on the different shower developments of protons and gamma rays was given earlier. Clearly proton initiated simulated cascades are desirable, since if they do prove to be broader than the gamma ray ones it may be a very useful parameter to use to distinguish between gamma rays and CR.

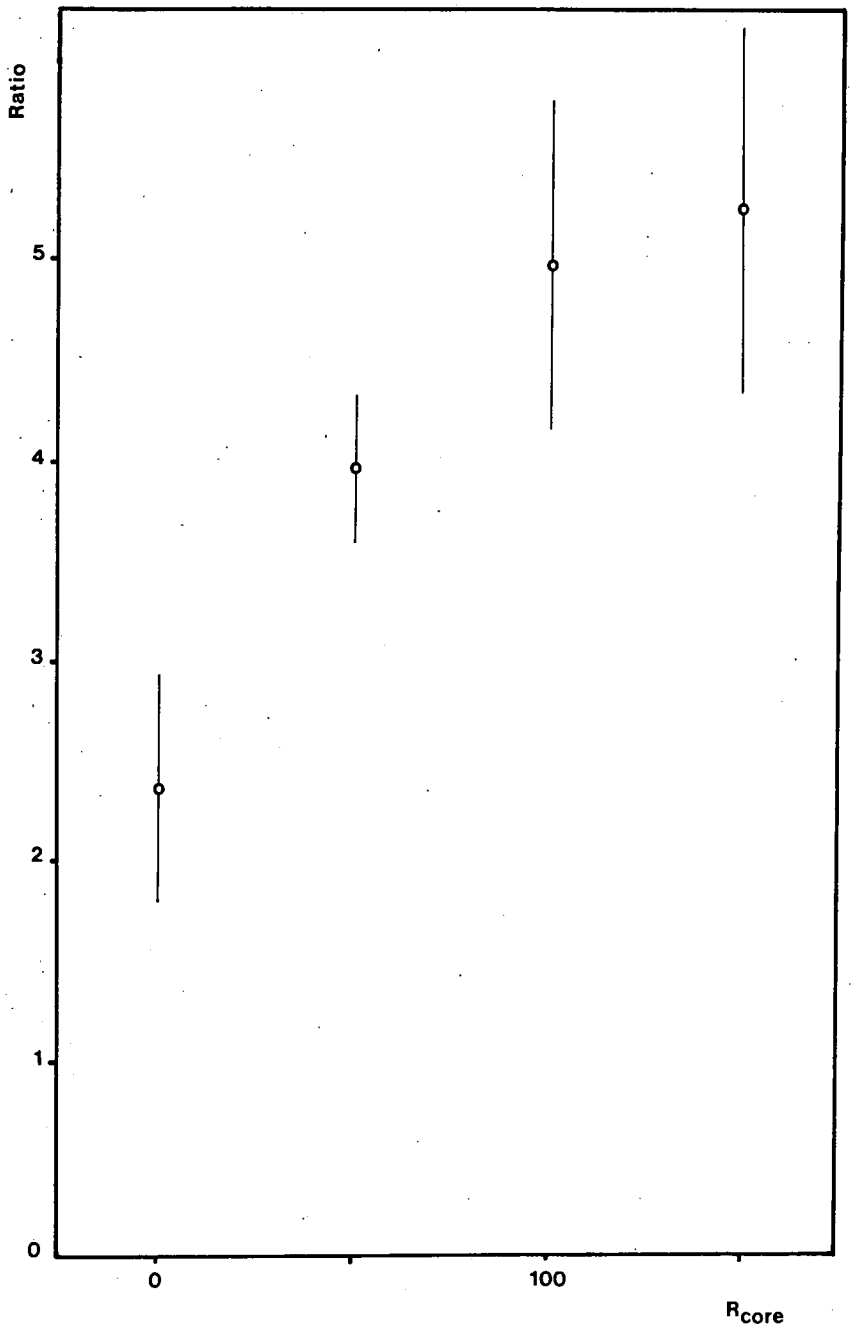

Figure 5.9 Variation of Angular Spread of Image with Core Distance.

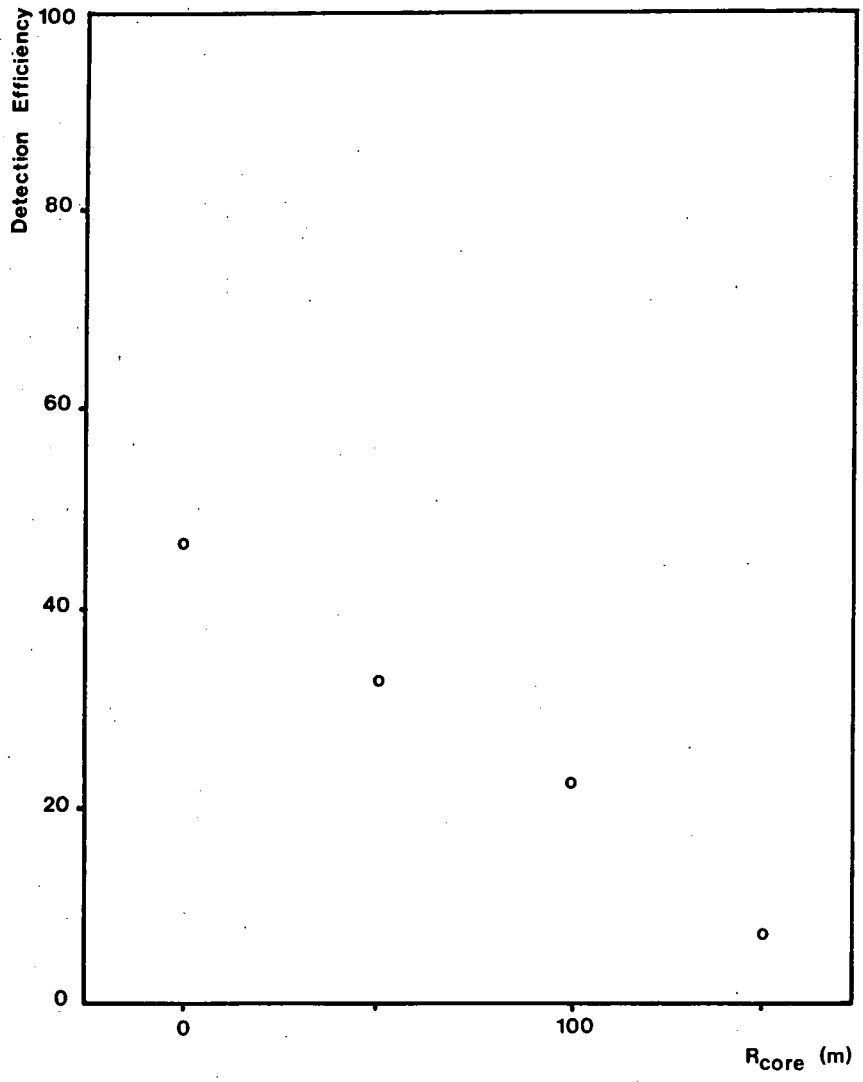

Figure 5.10 Variation of Detection Efficiency with Core Distance.

It has become clear from these simulations that determination of an accurate gamma ray direction from the shape and position of the image on the camera would not be expected to be successful. The peak signal generally is not predicted to occur at the core impact position, but displaced from it in a random direction, and the images themselves appear to be offset from the gamma ray direction by typically 0.5°, again in a random manner. Thus any particular image may be formed from a whole range of combinations of offset angle and core distance, and this does not seem to be resolvable. However, the ultimate test of the imaging technique is the detection of a source with an enhanced signal strength after "cutting" the data according to signal arrival direction data derived from the image.

CHAPTER 6.

THE ANALYSIS OF VHE GAMMA RAY DATA.

An overview of the analysis routines developed for the data recorded by the Dugway facility are described in this chapter. As noted previously, the data are recorded on 9-track magnetic tape. Before analysis of the data there are two preliminary operations to be carried out. The first is the translation of the stored information into a standard format, since, for reasons of efficiency the data are recorded in a compact format. The second step concerns the "look-ahead technique" described in the following section.

Subsequent sections describe the three principal categories of data analysis, which are count rate analysis, periodicity searches, and fast timing analysis to give within field of view selection.

6.1 The Look-Ahead Technique.

In Chapter 3 (section 3.11) an example of a typical section of data was given, and reference was made to the first two numbers in a record, n_1 and n_2 (Figure 3.10). These are labels which indicate the type of data stored, n_1 referring to the record held in the current line, and n_2 to that in the following line; this labelling is necessary since different types of record require differing formats. These numbers are inserted when the data is unpacked into the standard format to facilitate subsequent data analysis. The code employed is listed overleaf.

0 = housekeeping information

1 = record of array response to Cerenkov signal, auto mode

2 = record of array response to Cerenkov signal, SRQ mode

3 = unassigned

4 = time at which housekeeping taken

5 = detector pointing directions

6 = steering errors

7 = start of source record

8 = blocking information

9 = start of source message

10 = start of source target (R.A and DEC.)

(The start of source record indicates which detectors are on line, the source under observation, and the AGC ratio implemented.)

Thus when an analysis program reads the data file, these numbers are used to determine the format to be used. Generally, on the first occasion information is read from the file, just these two integers are extracted. The program then recognises what types of record are contained in the first and second lines, and is able to backspace and read the whole of the first line with the correct format. From that point on it always knows what type of data the next line will contain, and can choose the appropriate format with which to read it.

6.2 Count Rate Analysis.

This is carried out routinely on all the data obtained. The steps involved are listed below.

1. The Cerenkov pulses recorded each night are binned minute by minute.

2. A variable width sliding average of the data binned in (1) is taken. The usual width chosen is 10 bins (10 minutes).

3. The averaged data produced by (2) is plotted on a 10" plotter, to be used as a diary for the night's observation. This is annotated later with reference to the notes in the observers' log book.

4. A search for short (2-10 minute) bursts of activity is made using a maximum likelihood technique.

These processes were combined into a user-friendly package, described fully in section 6.5 and Appendix A.

6.2.1 Minute by Minute Binning.

A section of the binned data is presented in Figure 6.1. The first number is the time in seconds at which the 60 s bin begins; this is the time which has elapsed since the previous reset, and can be converted into absolute time. The second number is the zenith pointing direction of the array. The remaining columns indicate the number of array responses of each type ocurring during that minute, the type of array response being defined as follows.

Each type of array response is coded with a number, N, which indicates which telescopes were triggered by the Cerenkov pulse. N can take values between 1 and 15, there being this many possible array responses, and is calculated using the formula

$$N = 1xD_1 + 2xD_2 + 4xD_3 + 8xD_4$$

where

MINUTE BY MINUTE BINNING OF FILE 04.02

Time at start of bin (s)	Pointing direction zen azi	Array responses 1	2	12	3	13	23	123	4	14	24	124	34	134	234	1234
116224.126084	32.25 285.48	5	5	1	13	4	1	0	0	0	0	0	0	1	0	0
116284.126084	32.23 285.48	5	6	0	12	3	0	5	1	0	0	0	0	1	0	6
116344.126084	32.62 285.65	8	8	2	12	7	0	3	2	0	3	1	0	2	0	3
116404.126084	32.65 285.6	8	8	0	11	5	0	0	2	1	1	0	0	1	0	1
116464.126084	32.99 285.81	6	3	1	5	8	1	2	1	1	1	0	0	3	0	3
116524.126084	32.97 285.8	6	8	4	13	6	0	4	4	1	3	0	0	1	0	0
116584.126084	33.36 285.97	5	8	0	13	5	0	0	1	0	1	0	0	0	0	2
116644.126084	33.39 286.	1	8	0	17	6	1	2	2	0	1	2	0	2	0	1
116704.126084	33.72 286.14	3	9	1	9	4	0	0	0	0	0	0	0	4	0	3
116764.126084	33.70 286.2	3	7	0	10	0	0	1	0	1	0	0	1	1	0	1
116824.126084	34.09 286.30	3	3	1	12	4	0	3	0	0	0	2	0	0	0	3
116884.126084	34.12 286.4	5	11	0	17	2	1	1	0	2	1	0	0	0	0	2
116944.126084	34.46 286.47	5	7	0	12	3	1	1	1	0	0	0	0	1	0	2
117004.126084	34.43 286.47	4	7	1	8	3	0	2	0	0	0	1	0	0	0	0
117064.126084	34.83 286.63	6	10	0	14	6	1	0	1	0	1	0	0	1	0	1
117124.126084	34.85 286.6	5	9	2	11	2	0	3	2	1	1	0	0	2	0	1
117184.126084	35.19 286.80	3	6	1	9	1	0	0	1	1	0	1	1	2	0	0
117244.126084	35.17 286.8	3	5	1	9	6	0	1	2	0	0	1	1	2	0	3
117304.126084	35.56 286.96	2	4	0	11	3	0	3	2	0	0	1	0	1	1	1
117364.126084	35.59 287.	4	10	0	8	6	0	0	1	0	0	2	0	0	0	1
117424.126084	35.93 287.13	4	5	0	9	4	1	1	0	0	0	1	0	0	0	1
117484.126084	35.90 287.2	5	4	2	11	5	0	3	0	0	2	0	0	0	0	3
117544.126084	36.29 287.30	3	4	1	15	4	0	0	2	0	0	0	0	1	0	3
117604.126084	36.32 287.4	2	3	0	7	7	0	0	1	1	0	1	0	0	0	1
117664.126084	36.66 287.47	5	11	3	11	7	0	0	0	1	0	0	0	0	1	1
117724.126084	36.63 287.47	6	10	1	7	2	0	1	2	0	1	1	0	2	0	5
117784.126084	37.02 287.64	3	6	2	8	6	1	0	2	0	0	0	0	1	0	3
117844.126084	37.05 287.6	5	9	0	12	5	0	0	3	0	0	0	0	1	0	3
117904.126084	37.39 287.81	3	6	0	10	3	0	3	0	0	1	0	0	1	0	2
117964.126084	37.37 287.8	3	5	1	10	4	1	0	0	0	0	0	0	0	0	1
118024.126084	37.75 287.98	4	8	1	11	3	2	1	1	0	1	0	0	0	0	1

Figure 6.1 Sample of Binned Data (bin width = 60s).

D_i = 1, if detector i triggered

= 0, otherwise.

Thus the value of N unambiguously indicates which detectors were triggered.

6.2.2 The Sliding Average.

To illustrate the use of the diary of the night's observations a section of the plotter output is presented in Figure 6.2. The units of the vertical axis are counts while those of the horizontal axis are minutes.

There are eight quantities plotted, these being the number of array responses registered by each detector in conjunction with any other, the number of twofold detector coincidences, the combined number of threefold and fourfold coincidences, the number of responses in which detector 3 alone was triggered and the total count rate. (The reason for selecting detector 3 alone as one of the plots is that it is the most sensitive detector and is therefore the most likely to register any effect.)

6.2.3 The Maximum Likelihood Technique.

The basic idea of the drift scan technique is to search the data for an excess in counts during a period when the detector was pointing on-source by comparing with data recorded during an off-source period; the "ON" and "OFF" periods should be recorded as close together in time as possible. (Where appropriate, data recorded in the continuous tracking mode may be treated in a similar way as discussed later in this section.) The problem is to

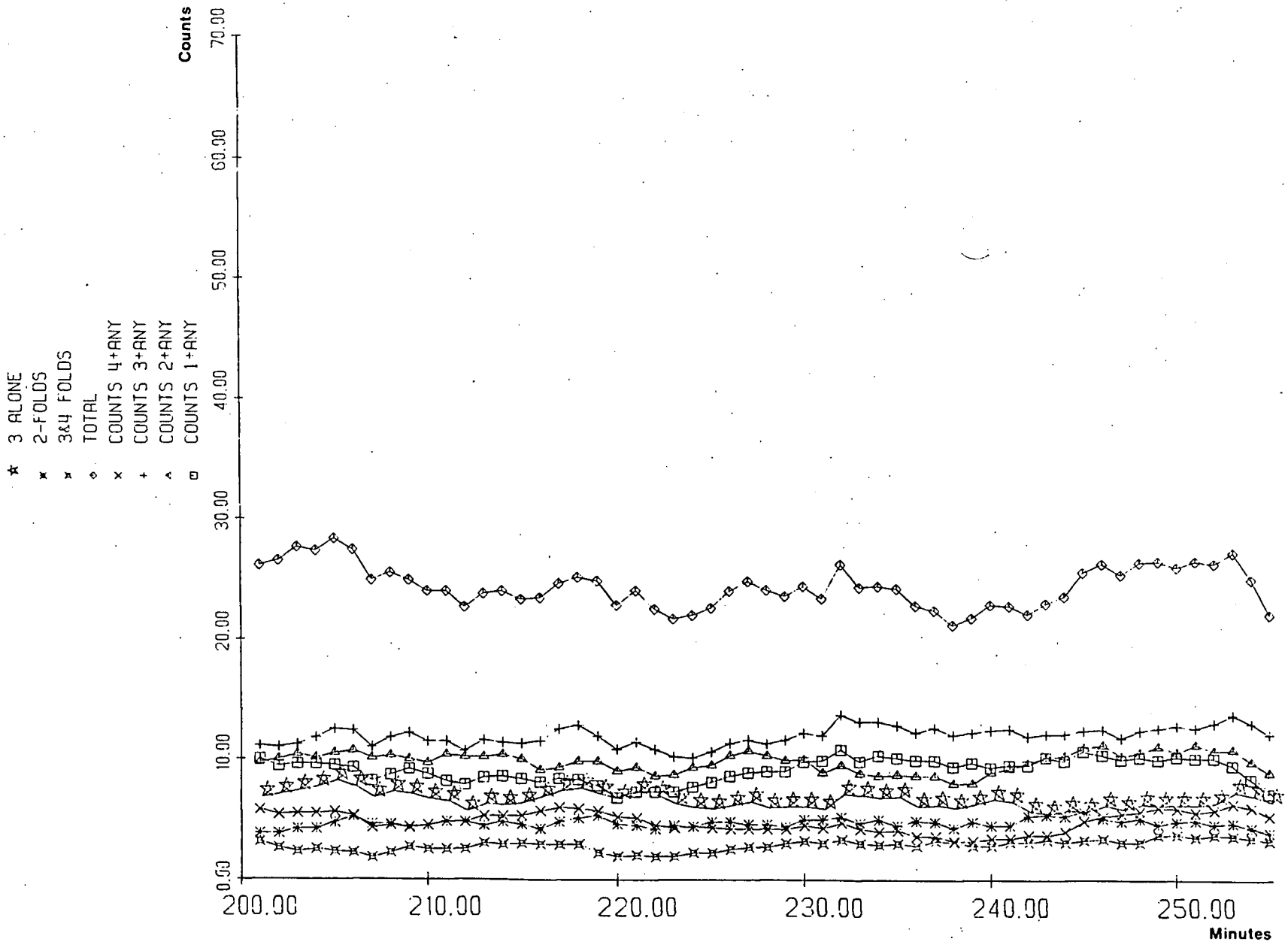

Figure 6.2 Minute by Minute Count Rate During 55 Minutes of Observation on 16 July 1982.

find a reliable way of measuring any excess and assigning a level of significance to it.

This problem has been discussed in detail by Hearn (Hearn, 1969) and O'Mongain (O'Mongain, 1973), who used a function giving the relative likelihood (λ) of an observed fluctuation being due to a source contribution:

$$\lambda = \max\left[\frac{P(N/S)}{P(N/S=0)} \right]$$

where the Ps are conditional probabilities. This function, however, requires an exact knowledge of the background counting rate. When both the source and background rates are unknown, as they are here, a reasonable test statistic to use (Orford, private communication) is the maximum likelihood ratio, l, given by

$$l = \frac{L_{max}(N \,/\, S=0)}{L_{max}(N \,/\, S)} \qquad (6.1)$$

where L is the likelihood of observing N counts when the source strength is S. The quantity l, therefore, corresponds to the probability that any observed effect is simply a random fluctuation in the background noise.

For a drift scan equation (6.1) can be rewritten as

$$l = \left[\frac{(N+B)}{N(1+a)} \right]^B \left[\frac{a(N+B)}{B(1+a)} \right]^N \qquad (6.2)$$

where 'a' is the ratio of off-source to on-source time, N is the

number of counts observed on-source and B that observed off-source.

It can be shown that the maximum likelihood estimate of the source strength S is simply the observed excess (Batschelet, 1981, pp. 303-305, for example) given by the expression

$$\langle S \rangle = N - \frac{B}{a} \qquad (6.3)$$

and the error in $\langle S \rangle$ is obtained by relaxing the value of 1 to S+ and S- which have 1 σ deviations from $\langle S \rangle$.

The technique may also be applied to tracking data in order to search for short bursts of activity by sliding a variable width (typically 2-10 minutes) "on-source" time through the data, and using the 10 minutes before and after this as the "off-source" time.

Generally the technique gives similar results to most current methods of treating this problem for small excesses of signal over background, but for other cases it is more conservative in ascribing the significance of detected signals.

6.3 Periodicity Analysis.

Data recorded during observations of suspected or known pulsars is subjected to searches for periodicity. The first step in this analysis is the translation of the event times from the LAB frame of reference into that of the barycentre of the solar system. A brief outline of this operation is given in the following section.

6.3.1 Translation of Event Times to the Barycentre.

The frequency of arrival of pulses at a detector is affected by the velocity of the observatory in the direction of the source, due to the Doppler effect. This depends on both the spin of the Earth and its orbital motion around the Sun. Therefore before the measured event arrival times may be subjected to searches for periodicity this effect must be corrected for. The correction is carried out in three stages.

1. The event times are translated to a point at the centre of the Earth to remove the effect of its spin. This requires accurate knowledge of the geographical coordinates of the Observatory.

2. The second translation is to the Solar System barycentre which removes the effect of the Earth's orbital motion. For this correction the absolute time of the measurement must be known precisely in order to deduce the position of the Earth in its orbit around the Sun (Chapter 3, section 3.9.2).

3. The final correction is to take into account relativistic effects on Earth-based clocks as the Earth orbits the Sun.

6.3.2 Searches for Periodicity.

The absence of any reliable light curves for observations at the high energies at which this experiment operates makes it impossible to search for periodicities in the data by the preferred method of correlating the signal arrival times with such curves. The procedure followed by other workers at these energies is to

examine how the signal arrival times are distributed in phase when unfolded with a trial period; from Poincare's theorem it is expected that a uniform phase distribution will be obtained if there is no periodicity in the data, that is if the pulse arrival times are purely random; this is the null hypothesis.

Normally a binned phase distribution, is used, and this is tested for uniformity (that is, lack of periodicity) by searching for excesses in one or more bins using, for example, Pearson's χ^2 test. This method of testing the uniformity of the distribution suffers from the fact that arbitrary choices have to be made with respect to the binning, which can lead to inconsistent results. The test for uniformity used in this experiment is the Rayleigh test (Mardia, 1972), which avoids the problems caused by binning, and this is described in the following section.

6.3.3 The Rayleigh Test for Uniformity of a Phase Distribution.

The Rayleigh test is well established as a measure of the uniformity of data obtained from measurements of cyclic phenomena (Batschelet, 1981). Its application in this experiment is now described.

Using a trial period the phase of each signal arrival time is calculated and a vector of unit length is assigned to each (in the absence of absolute phase information the phases may be calculated relative to some arbitrary zero point, such as that of the first detected pulse in the time series). The resultant vector, R, is calculated, normalised to give a value between 0 and 1, and tested for significance. If R differs significantly from zero the null

hypothesis (no periodicity) is rejected.

In general, for applications of the technique with sample sizes of 200 or less the vector R is tested for significance using standard tables (*ibid.* p. 334) but for larger samples, such as those obtained in this experiment, the test statistic $2NR^2$ is used, where N is the sample size.

The details of this procedure are as follows.

1. The phase of each event time t_i is calculated using

$$\theta_i = 2\pi f t_i$$

where $f = 1/T$. In the case of periodicity changing with a known first and second derivative this is modified to

$$\theta_i = 2\pi \left[f t_i + \frac{1}{2} \frac{df}{dt} t_i^2 + \frac{1}{6} \frac{d^2 f}{dt^2} t_i^3 \right]$$

2. The resultant vector, R, is calculated using the equation

$$R = (C^2 + S^2)^{0.5}$$

where

$$C = \frac{1}{n} \Sigma \cos(\theta_i)$$

and

$$S = \frac{1}{n} \Sigma \sin(\theta_i)$$

3. Finally, the probability of the obtained value of $nR(T)^2$ occurring by chance is calculated either from the χ^2 distribution for 2 degrees of freedom, which is $\exp(-nR^2)$, or more accurately:

$$\text{Prob.}(nR^2>k) = e^{-k}\left[1 + \frac{(2k+k^2)}{4n} - \frac{(24k-132k^2+76k^3-9k^4)}{228n^2}\right]$$

6.3.4 Checking the Technique.

This procedure for searching for perodicity in the data has been tested using a pseudo-random time series (with a randomly injected periodic component) corresponding to a detection system with a count rate of ~15 minute^{-1}; the periodic component, when present, was at a level of 8% of the total signal. The results are presented in Figure 6.3 (Gibson et al, 1982a) where the probability of no periodicity is plotted as a function of trial period (sweeping around the expected period in this way is a safety measure to check for a periodic signal occurring in only part of the data, or for errors in the ephemeris or its application). In the first case ([a]) the periodic signal was present throughout the sample, and the recovered periodicity is the correct one. In the second example ([b]) the periodic component is only present during the first 10% of the sample, resulting in the recovery of a period which is displaced from that expected by ~1 sampling interval.

6.4 Fast Timing Analysis.

Following the detection of an event by three or more detectors in the array, the direction of the source may be calculated from the relative times of arrival of the pulse at each

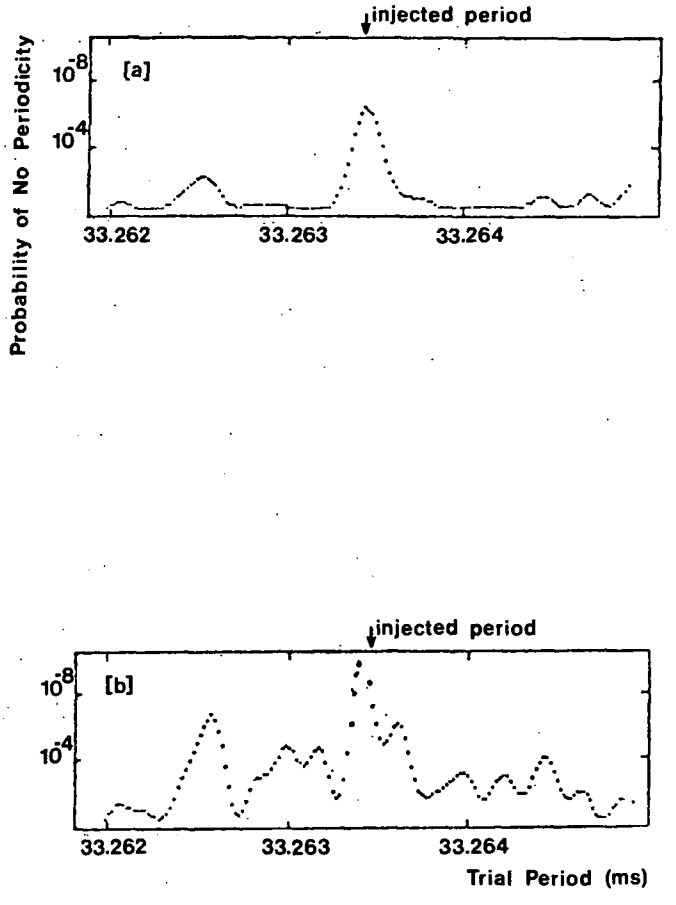

Figure 6.3 Probability of Uniformity of Phase for Simulated Results.

as follows.

Consider three detectors at positions (x_o,y_o,z_o), (x_1,y_1,z_1) and (x_2,y_2,z_2) receiving a pulse at times t_o, t_1 and t_2 respectively. From simple geometry it can be shown that:

$$cT_i = Z_i\cos\theta + \sin\theta(Y_i\cos\phi + X_i\sin\phi)$$

where

$$T_i = (t_i - t_o)$$
$$X_i = (x_i - x_o)$$
$$Y_i = (y_i - y_o)$$
$$Z_i = (z_i - z_o)$$

and θ and ϕ are zenith and azimuth directions respectively.

Thus it is possible to write down two simultaneous equations, for the cases i=1 and i=2, which when solved yield the following equations for θ and ϕ:

$$\cos^2\theta\,[(Y_1Z_2-Y_2Z_1)^2 + (X_2Y_1-X_1Y_2)^2 + (X_1Z_2-X_2Z_1)^2]$$
$$+2c\cos\theta\,[(X_2T_1-X_1T_2)(X_1Z_2-X_2Z_1) + (Y_2T_1-Y_1T_2)(Y_1Z_2-Y_2Z_1)]$$
$$+ c^2\,[(Y_1T_2-Y_2T_1)^2 + (X_2T_1-X_1T_2)^2]$$
$$- (X_2Y_1-X_1Y_2)^2 = 0 \qquad (6.4)$$

$$\cos\phi = \frac{c(X_2T_1-X_1T_2) + \cos\theta\,(X_1Z_2-X_2Z_1)}{\sin\theta(X_2Y_1-X_1Y_2)} \qquad (6.5)$$

From equation 6.4 there are two possible values for θ, corresponding to downward and upward moving showers; clearly only

the solution referring to the former is of interest.

Finally, the coordinates (θ,ϕ) may be translated into right ascension and declination using standard formulae.

6.4.1 Results of the Technique.

In order for the technique to be used reliably this procedure must be carried out on a large number of threefold events. Unfortunately, the rate of such events is too low at present for the results to be considered significant.

There are, however, sufficient twofold events recorded for the technique to be used in a modified form. Naturally with only two detector responses it is not possible to define a specific direction, but rather a line on the sky, corresponding to the locus of all points from which the signal could have arrived to produce the measured time difference between the two detectors. In practise, this line becomes a strip of width approximately 1° owing to a combination of experimental errors, and the jitter on the arrival direction of the Cerenkov light relative to that of the primary gamma ray.

The result of combining a large number of responses from a particular pair of detectors is a series of parallel lines across the field of view, with the greatest density of lines occuring at or near to the centre; these lines, therefore, map out a measure of the aperture function of the detector.

It follows that "on-source" data should yield tighter distributions in angle than "off-source" data, since the presence of a gamma ray source at the centre of the field of view is expected to result in proportionately more twofolds arising from

this direction. As mentioned earlier (section 6.2.3), these two types of data may be obtained either by directing the telescopes away from the source for part of the observation (the DS technique, used for study of d.c. sources), or by tracking a variable source continuously (the TR technique) and distinguishing between periods of strong and weak emission.

The technique has been used recently in its latter form to analyse bursts of emission recorded during TR measurements of the Crab Pulsar; the results (Dowthwaite *et al*, 1984) indicate significantly smaller angular spread for data recorded during the bursts than in quiet periods, confirming the usefulness of fast timing analysis as independent corroboration of the detection of a gamma ray source.

6.5 The Package for Routine Data Handling.

This package was designed to provide an effective means of producing the large quantities of paper output involved in the routine data scrutiny; the scope of the package does not extend to periodicity analysis or fast timing analysis. A principal requirement was that the package be accessible to people lacking intimate knowledge of the computer system. The computer used initially for this work is NUMAC (Northumbrian Universities Multiple Access Computer), an IBM 370/168 using the Michigan Time Sharing (MTS) operating system. All data analysis routines are now in the process of being transferred to the Starlink node at Durham, which uses a VAX 11/750. Starlink offers several advantages over NUMAC, including a more flexible operating system, a more modern FORTRAN compiler (FORTRAN 77, as opposed to FORTRAN 66), and

greater user convenience regarding tape handling, since the tapes and tape-drives are all at Durham rather than Newcastle.

6.5.1 Overview of the Package.

A detailed description of the program with flow diagrams is given in Appendix A. Briefly, it is a 'menu-driven' package with eight main options available. These range from simple items, such as viewing a tape file at the terminal, to more complicated ones, like scanning a night's data for bursts of activity. The full list is presented below.

1. Displaying a tape file on the VDU.
2. Dumping a tape file to the printer.
3. Dumping a tape file to a disc file.
4. Binning data from a tape file, minute by minute.
5. Binning data from a disc file, minute by minute.
6. Taking a variable width sliding average of data binned by (4) or (5).
7. Plotting data averaged by (6).
8. Scanning the data for bursts using the maximum likelihood technique.

The program is highly "user-friendly". Having selected one of the supplied options the user is prompted for all further information required to carry out the processing, such as names of tapes and files and other option parameters; all system commands are generated by the program to prevent corruption of the database owing to errors on the part of the user. For the benefit of the

more experienced user the program incorporates a command structure to speed the analysis process without compromising any of the safety measures.

With regard to the future, provision has been made for the extension of the range of options if required.

CHAPTER 7.

RESULTS OF OBSERVATIONS OF TWO GAMMA RAY SOURCES.

The observing schedule for 1981 and 1982 was dominated by two sources. One of these (PSR 0531, the Crab Pulsar) was known to be a strongly emitting pulsar at lower energies with a well-defined period, but although measurements had been made at VHE gamma ray energies previously, none were of high statistical significance. The other source (Cygnus X-3) was, and remains, something of an enigma. It is a variable source observed over a very wide range of wavelengths, with at least one periodic component. It is the only source of its kind so far recorded, and is the subject of much theoretical discussion. As the experiment has progressed the catalogue of observed sources has expanded, to include about 12 objects including Hercules X-1 and PSR1937, the millisecond pulsar.

In this chapter results based on data collected over two seasons of observation are presented. The first section deals with measurements of Cygnus X-3, which has already been detected at radio, optical, infra-red and X-ray wavelengths (Gregory, 1972; Weekes and Geary, 1982; Mason *et al*, 1976; Elsner *et al*,1980) in addition to the gamma ray region. Those observations at infra-red and X-ray wavelengths have clearly shown the characteristic 4.8 hour periodicity first reported in 1972. Observations at low gamma ray energies (~100 MeV) have been somewhat contradictory. High fluxes were reported by Galper following balloon measurements between 1972 and 1976 (Galper *et al*, 1976). The SAS-2 observations made during this period, in 1973, showed a signal at a lower flux

value than the balloon measurements, apparently modulated with a 4.8 hour period (Lamb *et al*, 1977), but the later observations by the COS B satellite (Strong, 1982) failed to reproduce this result. Observations at high energies, close to those detectable by the Dugway telescopes (>1000 GeV), have been made previously at three observatories, all suggesting the existance of a 4.8 hour periodic signal, with the maximum coinciding with the X-ray maximum (Neshpor *et al*, 1979; Danaher *et al*, 1981; Lamb *et al*, 1981).

The results presented here, based on by far the largest data set, confirm the existence of a 4.8 hour periodic signal at gamma ray energies (>1000 GeV), and go further to provide details of the temporal form of the bursts of emission and give some indication of a long term (34 day) variation of the emission.

In the second section results of observations of PSR0531 (the Crab Pulsar) are presented. Most previous observations of this object in the VHE gamma ray region have recorded pulsed emission with the expected periodicity, but there has been disagreement in the values obtained for the time averaged fluxes (Grindlay *et al*, 1976, Jennings *et al*, 1974, Erickson *et al*, 1976, Gupta *et al*, 1978) and there have been suggestions of long term variability of the emission at these energies over periods of days or months. Strong evidence for bursts of VHE pulsed gamma ray emission on a much shorter time scale (~15 minutes) has been found in the data recorded by the Dugway system. This short duration may be an explanation of the previous apparently discordant results for the time averaged fluxes.

7.1 Cygnus X-3.

The results presented here are based on 263 hours of observation in 1981 and 1982. The data were recorded in both DS (July-October 1981) and TR (July-November 1982) mode, and so the methods employed to analyse them differ slightly, although the basic technique, discussed in the preceeding chapter, remains the same.

7.1.1 4.8 Hour Periodicity.

(A) DS Data.

It proved convenient to use a DS duration of 36 minutes since this enabled observations to be made at eight equally spaced phases in the established 4.8 hour X-ray period, while ensuring that data were taken over a sufficiently long interval to allow application of the DS technique (see below) taking into account the time required for steering the array at the beginning of each scan (several minutes).

The technique employed to analyse DS data followed the established procedure of splitting the data into three 10 minute sections, one centred about the time of transit of the object through the centre of the field of view and the others symmetrically placed on either side of this. The central section was therefore designated as ON source data, and the two outer sections as OFF source, these being averaged to take account of possible variations in the background count rate.

Only DS data taken under clear sky conditions were used in this analysis, since the presence of cloud could lead to unpredictable variations in the background count rate. A total of

76 DS recorded in 1981 were used (containing 43921 recorded Cerenkov pulses) 48 of which had phases chosen to include the 0.625 X-ray phase, the remaining 28 (recorded in October 1981) having phases displaced by +0.03 from the earlier observations. This was done as the final step of a programme to cover those phases at which initially no data was taken, that is, those occurring when the telescopes were off source.

The scans were combined according to their phases in the 4.8 hour X-ray period, and the ratio ON/OFF calculated for each phase (Figure 7.1, Dowthwaite *et al*, 1983). An excess in the count rate is observed around X-ray phase 0.625/0.655, for which the ratio ON/OFF was 1.076 ± 0.031. Following the procedure outlined in Chapter 6 (section 6.2.3) the maximum likelihood estimate of the source strength is 124.5 counts with upper and lower limits of 175.5 and 73.9. The same calculation for 1981 data integrated over all phases produces a value for the ratio of 1.00 ± 0.01, indicating that most of the emission from the object occurs at phase 0.625/0.655.

This result is significant at the 2.4 standard deviation (σ) level, and assuming that the emission occurs throughout the ON period it indicates that the peak gamma ray flux has a lower limit of 7.6% of the background flux; given the threshold at which the system operates this corresponds to an integral peak flux of at least 2.6×10^{-10} $cm^{-2}s^{-1}$ at this phase. The absence of any evidence for excess emission at the phases either side of 0.625/0.655 would seem to indicate that the duration of the emission is no longer than 36 minutes, This result does not conflict with those of previous experiments having similar fields

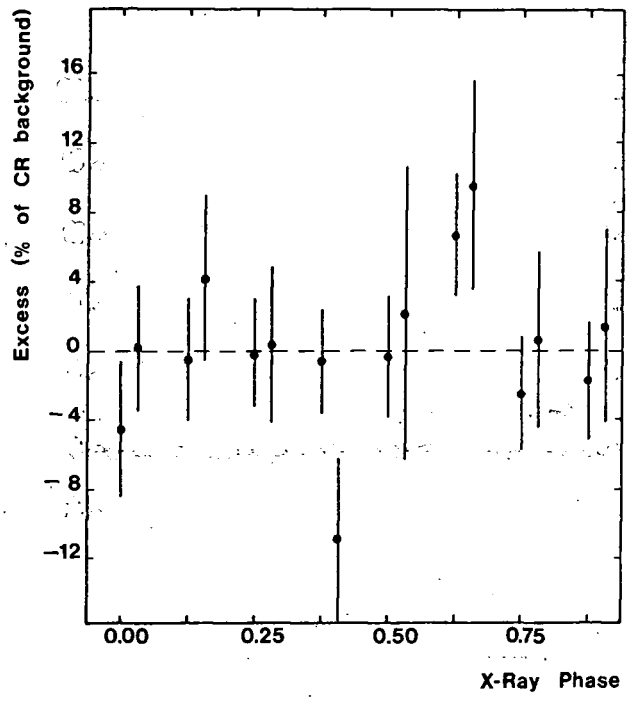

Figure 7.1 Excess Counts ON/OFF Source for the Aggregate Response of Four Telescopes during DS Measurements in 1981 Plotted as Function of Phase in the 4.8h X-Ray Period.

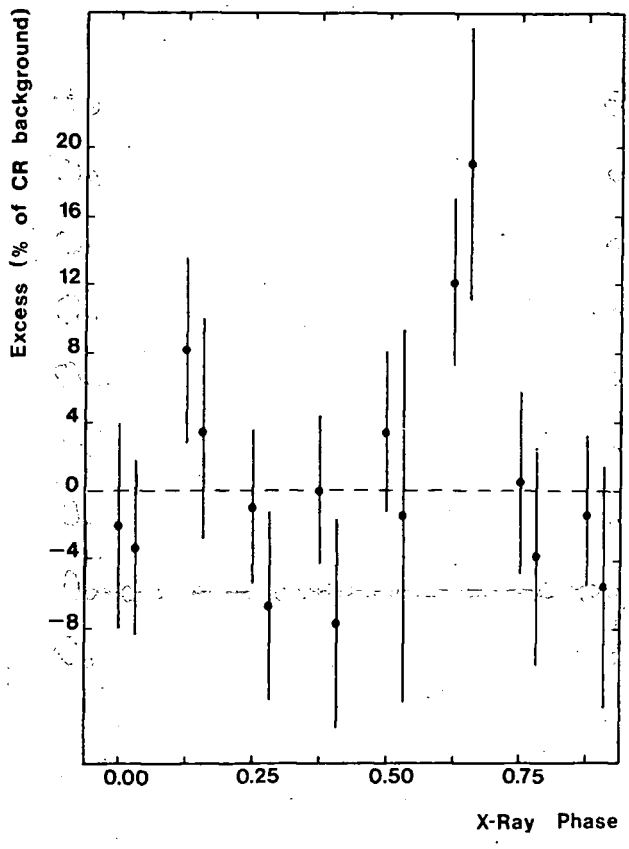

Figure 7.2 Excess Counts ON/OFF Source for the Low Energy Threshold Telescopes during DS Measurements in 1981, Plotted as Function of Phase in the 4.8h X-Ray Period.

of view; Neshpor reported a 5% signal lasting for about 10-15 minutes (Neshpor *et al*, 1979), Danaher one of 20% lasting for less than 30 minutes (Danaher *et al*, 1981), and Lamb one of 6% lasting for about 60 minutes (Lamb *et al*, 1981), all of these occurring at similar X-ray phases.

During the 1981 observing season, one of the telescopes had a significantly lower threshold than the others, and this has been found to contribute most of the observed effect. In Figure 7.2 the ratio ON/OFF at all phases is plotted again for this telescope alone (Dowthwaite *et al*, 1983); the excess obtained is 14%, a result which is significant at the 3.35 σ level. This supports the suggestion by Vladimirsky (Vladimirsky *et al*, 1973) that the gamma ray energy spectrum may be steeper than the cosmic ray spectrum at these energies.

(B) TR Data.

The tracking observations made in 1982 resulted in the detection of 78520 Cerenkov pulses. To enable the TR data to be compared (and combined) with the DS data recorded in 1981 similar analysis techniques were employed; the 10 minute section around each of eight equally spaced phases in turn was used as ON source data, and the corresponding 10 minute sections before and after as OFF source data. Since the source is always in the field of view this treatment relies on the assumption, based on the 1981 results, that the activity is confined to a 10-15 minute period. The choice of phases was made to include X-ray phase 0.625, the region of activity in the 1981 measurements.

A potential additional problem with the application of DS

analysis techniques to TR data is the variation in background count rate over the period of a "scan" due to changing zenith angle, but careful study of this variation over the range of zenith angles employed has eliminated the possibility of this having a significant effect on the results (Dowthwaite *et al*, 1983).

As expected following the 1981 result, the ratio ON/OFF for all data integrated over all phases was found to be 1.00 ± 0.01. As mentioned earlier in this thesis the number of telescopes with low energy thresholds was increased to two at the start of the 1982 observing season, and analysis of the data recorded by these two alone yields a positive effect at phase 0.625 similar to that obtained in 1981, with VHE gamma ray emission measured at 6.8% of the background count rate, a result significant at the 2.7 σ level (Figure 7.3). With hindsight, this pseudo DS technique probably only gives a lower limit to the flux, owing to the possible absence of a true OFF source measurement.

Finally, combining the data recorded by low energy threshold detectors over both seasons yields an excess at phase 0.625 at the 4.05 σ level; this corresponds to a flux of about 3×10^{-10} cm^{-2}s^{-1} at an energy threshold of 1000 GeV.

7.1.2 34 Day Periodicity.

Following X-ray measurements of Cygnus X-3 Molteni has suggested a long term variability of emission of 34 days (Molteni *et al*, 1980). An investigation has been made to determine whether this is manifested at VHE gamma ray wavelengths. In Figure 7.4 the percentage excess at all phase 0.625 observations are plotted according to their phases in the 34.1 day period, and there is some

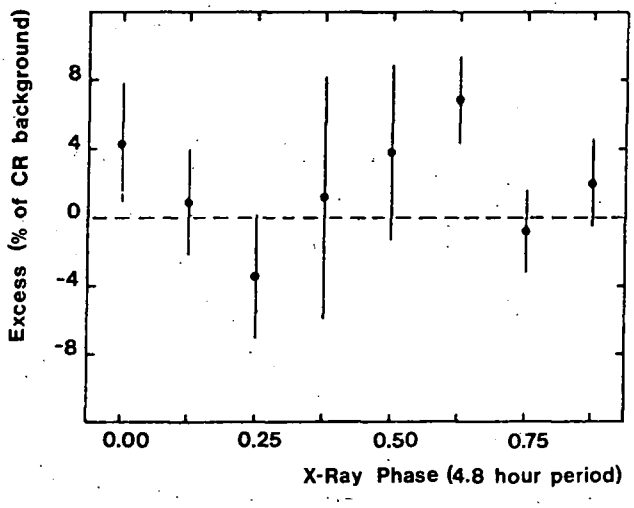

Figure 7.3 Excess Counts Detected by Low Energy Threshold Telescopes, Plotted as Function of Phase in the 4.8 h X-Ray Period.

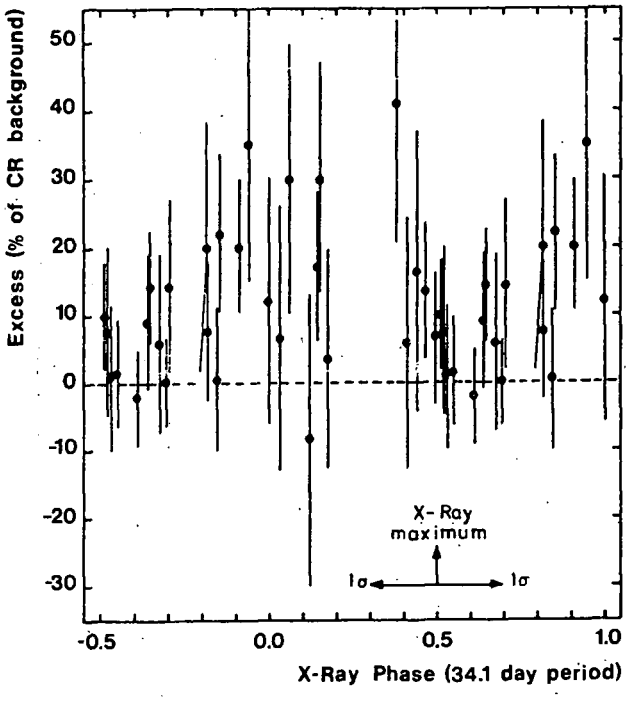

Figure 7.4 Excess Counts at Phase 0.625 in the 4.8 h X-Ray Period, Plotted as Function of Phase in the 34 d X-Ray Period.

indication of such a long term variability, although the maximum is offset from that obtained for X-rays by ~7 days; the X-ray and gamma ray light curves would coincide if a period of 33.91 days was chosen, and this would not conflict with the X-ray data recorded in 1977-1978.

7.1.3 Structure of the Bursts of Emission.

It has already been stated that the emission appears to be confined to a period of about 10 minutes around phase 0.625. It is of interest to investigate the uniformity of the emission over this period, and to this end the data from the five observations displaying the most significant excesses at phase 0.625 in 1982 were summed (Figure 7.5); the diagram shows the minute centred upon phase 0.625. The activity appears to be concentrated in two 3-4 minute bursts, separated by 3 minutes; during these bursts the gamma ray flux is 50% of the CR background.

7.1.4 Energy Spectrum of Gamma Rays.

As mentioned previously, the varying sensitivities of the telescopes allows an estimate to be made of the slope of the spectrum around 1000-2500 GeV (the data used for this purpose were those recorded at X-ray phase 0.625). The result suggests a slope for VHE gamma rays which is steeper than the proton spectrum at these energies (1.60) by 0.8 ± 0.5.

7.2 Crab Pulsar PSR0531.

The data upon which these results are based was collected during 34 hours of observation of PSR0531 between 25 September and

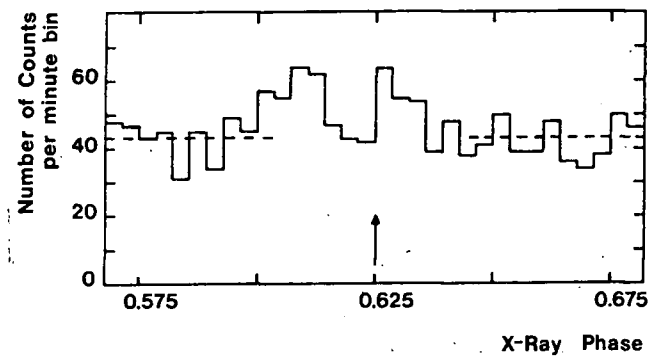

Figure 7.5 Accumulated Count Rate for Low Energy Telescopes During Five Intervals of Tracking Cygnus X-3 in 1982.

2 November 1981. They were recorded in the TR mode, and without the use of stabilising procedures described in Chapter 3 (section 3.5.1), which have the disadvantage of raising the detection threshold energy, in order to achieve as high a rate of shower detection as possible. (Subsequent experience has indicated that the advantage of low threshold when observing in this way is outweighed by the disadvantages from loss of stability, and all the TR data taken in 1982 were obtained using the stabilising procedures.)

7.2.1 Preliminary Analysis.

Following the procedure outlined in Chapter 6 (section 6.3.1), the times of arrival of the Cerenkov flashes recorded in 1981 were reduced to the Solar System barycentre, and then unfolded using an ephemeris derived from contemporary radio observations (A.G.Lyne, private communication):

period = 0.033263833076 s

derivative = 36.416 ns day^{-1}

epoch = 2444910.5 .

Initially, each night's observation was taken as a complete data-set, and the data were searched, without success for evidence of periodicity using the Rayleigh test (Chapter 6, section 6.3.3).

7.2.2 The Effects of 23 and 31 October 1981.

In view of the possibility that any periodic component may occur in only part of the data, the procedure of sweeping around

the expected period (as discussed in Chapter 6, section 6.3.4) was adopted. This resulted in the detection of a strong effect on 23 October 1981 at a period displaced by one Fourier harmonic from that of the ephemeris.

In order to place this effect in the same Fourier harmonic as the ephemeris period the data was divided into 15 minute sections and the procedure employed to search for non-uniformity in the earlier, larger dataset repeated. One of these sections yielded an effect with a probability of chance occurrence of $<10^{-6}$, despite the increase in the number of degrees of freedom from 1, in the case of the whole 34 hours being treated as one data set, to 130. In addition, the same treatment of data recorded on 31 October revealed a similar but less significant effect in one section, with a chance probability of $\sim 10^{-4}$.

The diagrams in Figure 7.7 (Gibson *et al*, 1982a) were derived by sliding a section of fixed length (15 minutes) through the data in 2 minute increments and calculating the probability of no periodicity for each 15 minute dataset, following the procedure above. This allowed the times of the two outbursts to be specified more accurately. The peak on 23 October has a chance probability of 4×10^{-9}, with 34 ± 5 % of the recorded responses being periodic; this corresponds to an integral flux of $(2 \pm 0.3) \times 10^{-10}$ cm^{-2}s^{-2} for the 15 minute burst. The threshold energy depends on the zenith angle at which the data are taken and for this observation was 3000 GeV.

7.2.3 The Light Curve.

The light curves derived from the bursts of 23 and 31 October

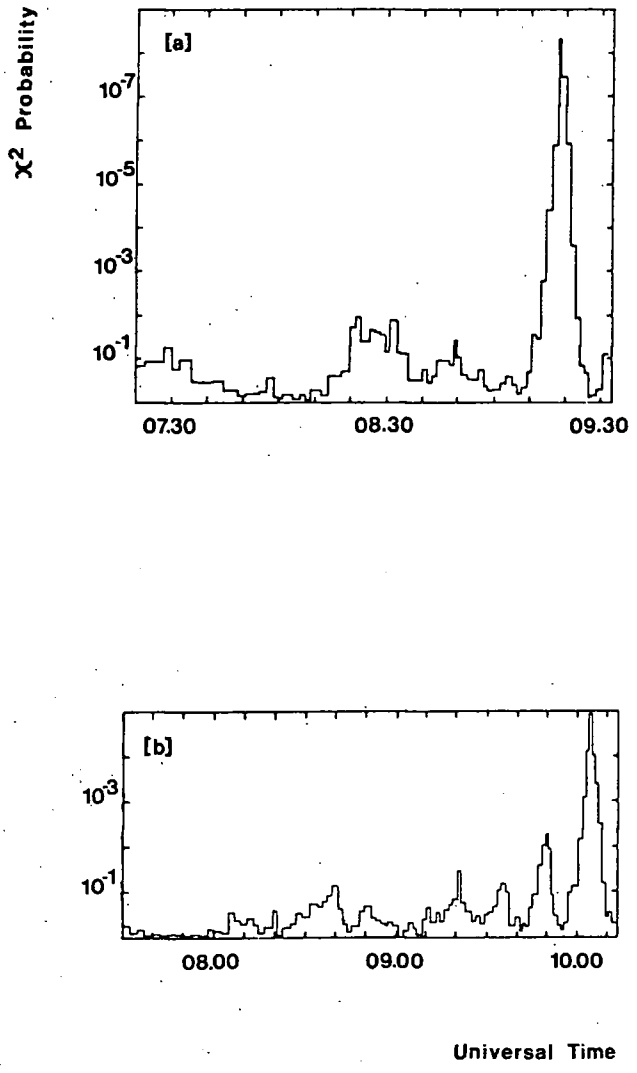

Figure 7.6 Probability of No Periodicity at the Radio Period for Data in 15 Minute Intervals During Observations on [a] 23 October 1981 and [b] 31 October 1981.

are presented in Figure 7.7 (Gibson *et al*, 1982b). In both, a single pulse is seen, with similar shape and long duration of 6 ms FWHM. This contrasts with the characteristic signature of main pulse and interpulse observed at radio, optical and X-ray wavelengths, but there is no reason to suppose that this light curve should be repeated at the much higher energies at which our measurements were made. The absence of contemporaneous absolute phase information made it impossible to determine the absolute phase at which the peak in VHE gamma ray emission occurs.

7.3 Recent Developments in the Analysis of Data from PSR 0531.

7.3.1 The 1981 Outbursts.

A more precise contemporary radio ephemeris incorporating absolute phase information was made available in late 1982 (A.G. Lyne, private communication) and this has been used to re-examine the two outbursts recorded in 1981. The results, to be published in the near future, indicate that the largest (October 23) occurred at the same phase as the radio main pulse. There is a slight change in shape of the light curve compared with that obtained previously (Figure 7.7a) which results from the use of a more appropriate ephemeris, and there is now a possible peak at the expected position of the interpulse.

The burst of 31 October 1981 had a light curve with a single peak of ~10 ms width (Figure 7.7b), which apparently occurred about 13 ms before the radio main pulse.

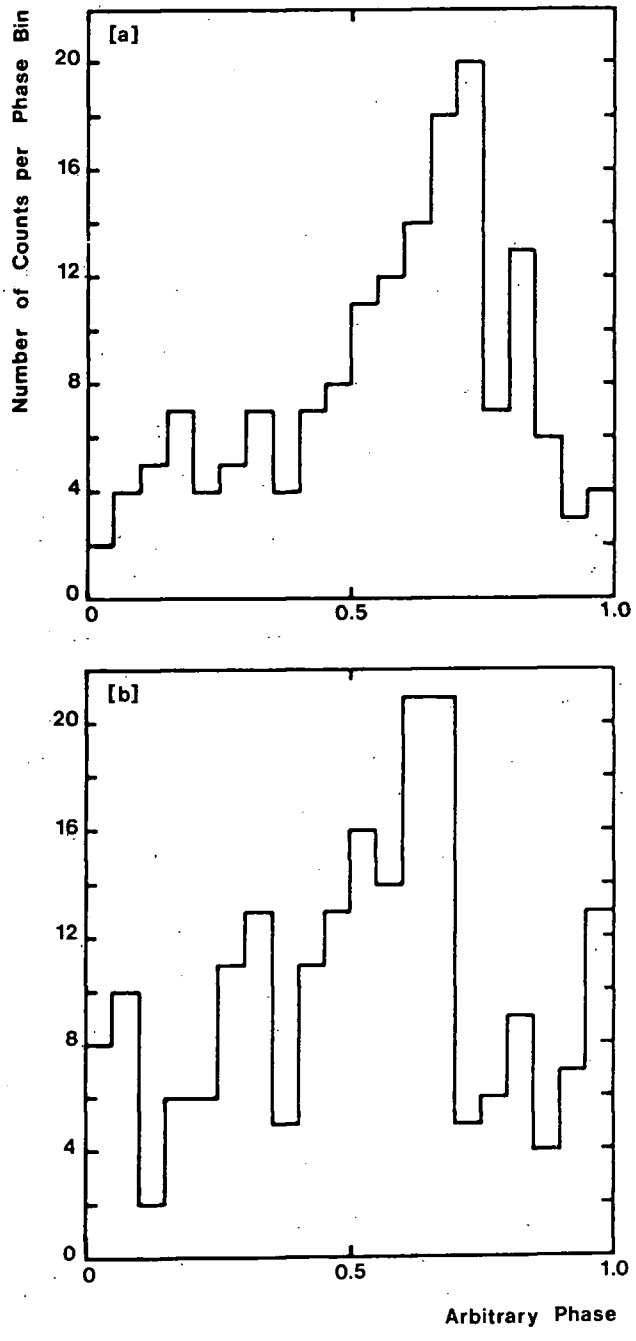

Figure 7.7 Light Curves for Periods of Activity on [a] 23 October and [b] 31 October 1981.

7.3.2 Observations in 1982 and 1983.

Further observations of PSR 0531 were made between September 1982 and November 1983. The sensitivity of the array had been improved as mentioned in Chapter 4 (section 4.5.3), and these measurements were taken using the stabilising procedures omitted during the 1981 observations of this source. Data on 156342 events were recorded in the TR mode over a total of about 103 hours.

Following the same analysis procedure as before, no further evidence for sporadic activity on a timescale of minutes has been found which was as strong as the 1981 effects. There does, however, appear to be evidence for emission occurring throughout the 103 hours of data taken in 1982-1983 (Dowthwaite *et al.*, 1984a).

CHAPTER 8.

DISCUSSION OF RESULTS.

In this chapter the results described in Chapter 7 are discussed. In the case of Cygnus X-3 the various models which have been proposed to incorporate the results of observations at all wavelengths are reviewed in the light of the steep VHE gamma ray spectum indicated by the present work. Measurements of the Crab pulsar have detected periods of transient pulsed emission (in 1981) and also steady, low-level, pulsed emission (in 1982-1983), the latter giving rise to a light curve with a narrow peak at the same phase as the radio main pulse. The implications of these results are discussed, and evidence is presented which indicates that the energy spectrum for gamma rays for this object steepens above 100 GeV.

8.1 Cygnus X-3.

The results reported in the preceding chapter are in general agreement with those of other workers regarding the variations in emission from Cygnus X-3 over periods of 4.8 hours and 34 days. With respect to the former, the phase of the peak coincides approximately with those of earlier measurements, but its duration is much shorter. X-ray emissions from this source have a light curve which is approximately sinusoidal, but since it is unlikely that the same mechanisms are responsible for the two emissions, similar light curves would not necessarily be expected. However, the light curves derived for VHE gamma rays in other experiments have also indicated a longer duration for the emission than that

measured here, with Lamb reporting emission lasting for about an hour during contemporaneous observations (Lamb *et al*, 1981).

The peak in the 34 day light curve is displaced by ~7 days from that derived from the X-ray results of Molteni (Molteni*et al*, 1980), but when the uncertainties involved in bringing the X-ray result forward over 5 years are taken into consideration, the result is quite close.

The energy spectrum of radiation from Cygnus X-3 is shown in Figure 8.1, with the result from the present experiment included. The value plotted is the time averaged VHE gamma ray flux above 1300 GeV, with the peak fluxes for this and earlier measurements being shown inset on this diagram. This result is in accordance with earlier gamma ray results and the recent air shower result (Samorski and Stamm, 1983) confirming the importance of the energy carried by gamma rays emitted by Cygnus X-3.

8.1.1 Models for Cygnus X-3.

An attempt to incorporate previous results, at X-ray and infrared wavelengths, in a model for Cygnus X-3 was made by Milgrom, with limited success (Milgrom, 1976), in which it was suggested that the source consisted of the usual X-ray binary system surrounded by a spherical shell of gas. Following the detection of gamma rays above 35 MeV with a 4.8 hour periodicity by the SAS-2 observations (Lamb *et al*, 1977), Milgrom and Pines (Milgrom and Pines, 1978) proposed a model which introduced a rapidly rotating (period ~10 ms) pulsar into the cocooned binary model, but this did not explain the emission of VHE gamma rays.

More recently, Vestrand and Eichler have considered a pulsar

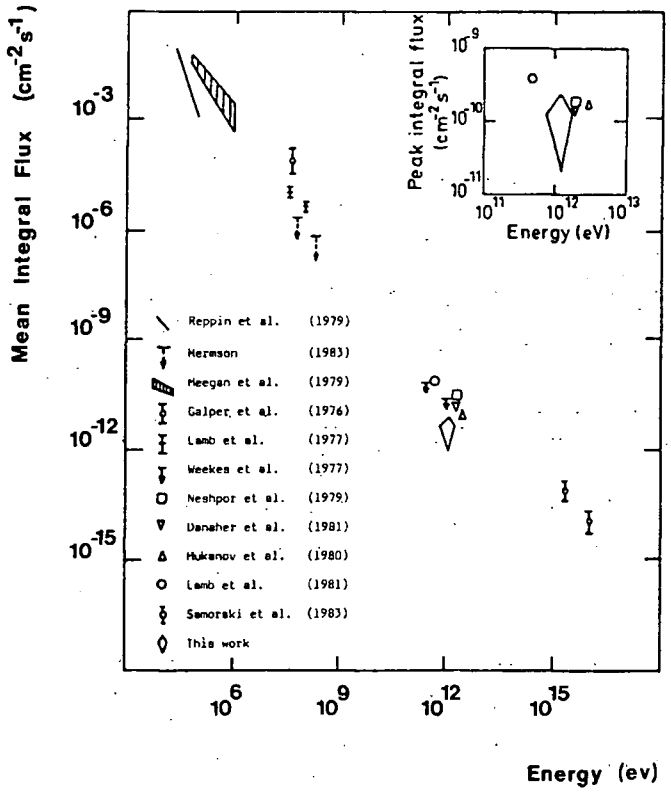

Figure 8.1 Energy Spectrum of Radiation from Cygnus X-3 in VHE Gamma Rays at X-Ray Phase 0.625.

model incorporating direct particle interaction, in which CR accelerated from the pulsar strike the atmosphere of the stellar companion resulting in the emission of gamma rays (Vestrand and Eichler, 1982). This would explain the production of the twin peaks reported by some observers (Neshpor *et al*, 1980), but the short outbursts reported here are not expected from the pulsar-driven model because, owing to Alfven scattering, the beam is not expected to be so well collimated as to produce gamma ray bursts on such a short timescale.

This short term variability has lead Grindlay to propose a non-aligned rotator model for Cygnus X-3 (Grindlay, 1982b), which follows from models suggested for SS433 (which is apparently similar in that it exhibits twin peaks of emission within a period of 13 days, modulated by a long term variability of about 160 days), and offers an alternative to the pulsar-driven models with an accretion-driven model.

In this model, the source is a binary system, with a compact star in orbit around a much more massive companion, which is surrounded by a cocoon of gas: owing to its spin, the companion and its cocoon take the form of an oblate spheroid. The compact object is surrounded by an accretion disc of matter drawn from its companion, which powers the jets of electrons emitted along the magnetic field lines at its poles. These electrons, which may be accelerated up to relativistic energies, are then scattered by the inverse Compton process off starlight emitted by the companion, producing gamma rays.

The observed periodicities are explained as follows. The spin axis of the companion is misaligned with the orbital angular

momentum vector of the compact object, which leads to enhanced accretion onto the disc occurring twice per orbit owing to the doubly-periodic modulation of the Roche lobe radius of the companion. This, it is suggested, may account for the peaks in the emission of Cygnus X-3 at phases 0.125 and 0.625, (although in our data only the peak at phase 0.625 was observed with significance). In addition, the quadrupole moment of the companion star feels a torque from the disk, owing to its misalignment, which causes its spin axis to precess, further modulating the supply of gas to the accretion disc and hence the emission of VHE gamma rays; this may account for the established long term modulation of SS433 (period ~164 days) and similarly the suggested 34 day periodicity of Cygnus X-3.

In conclusion, the possible detection of a 34 day modulation of the peak gamma ray flux, in addition to the 4.8 hour period, is consistent with an accretion-driven model incorporating a misaligned binary system, similar to the one proposed for SS433. On the other hand, a firm indication of emission in the form of two short bursts may favour a pulsar-driven model although the definitive test for such models remains the detection of pulsed VHE gamma rays.

8.2 Crab Pulsar (PSR0531).

Extensive measurements of gamma rays from PSR0531 have been made at lower energies (100-1000 MeV) using the COS-B satellite (Wills *et al*, 1982). These provided evidence for a narrow main pulse, a broader interpulse of variable strength and weak emission in the intermediate region. At higher energies (100-1000 GeV) the

atmospheric Cerenkov technique has been employed by a number of workers, reviewed by Porter and Weekes (Porter and Weekes, 1978). There has been no agreement about the shape of the light curve, nor have the reported features borne any consistent phase relationship with emission at other wavelengths.

An important aspect of the present results of observations of the Crab pulsar lies in the detection of pulsed emission of VHE gamma rays occurring in short (~15 minutes duration) bursts. To determine whether showers occurring during the burst had different properties from those detected at other times, the records have been examined in detail.

Taking the burst of 23 October 1981, and dividing the showers into two groups, that is, those occurring during a 20% phase interval at the peak of the light curve and the rest, it was found that the latter were similar in all respects to showers occurring immediately after the burst, whereas the former was rich in double telescope responses: the χ^2 chance probability was 1%. The number of three and four telescope responses recorded was too small for a similar enhancement to be found with any statistical significance, and for the same reason, the strength of the burst on 31 October 1981 was insufficient to permit similar analysis.

A different approach was used to analyse the 1982 data. The simulation results in Chapter 4 (section 4.5.6) indicate that in general, at observation thresholds appropriate to the Dugway array, aperture functions for twofold responses are narrower than those for single-folds. The arguments presented in that chapter indicate that this narrowing of the aperture function should be beneficial to the detection of gamma rays from the source against the CR

background, and the experimental evidence in support of this using 1982 data was given there (Figure 4.14). This is also consistent with the above analysis of the 1981 outbursts.

8.2.1 The Light Curve.

As mentioned in the preceding chapter, the light curves obtained for the 1981 outbusts from the Crab pulsar at VHE gamma ray wavelengths are different from the established curves measured at radio, optical and X-ray wavelengths in having a single long pulse. At much lower gamma ray energies (< 1 GeV) the Caravane collaboration reported a light curve with a main and an interpulse of a few milliseconds duration based on early observations, but in later measurements the interpulse was seen to decrease in amplitude (Wills, 1981).

On the other hand, the light curves obtained for data in 1982-1983 are similar to those observations at lower energies, displaying the characteristic narrow pulse at the phase of the radio main pulse. This would seem to suggest a difference between the mechanism for continuous emission and that for the 1981 outbursts.

8.2.2 Summary of Observations of PSR0531.

The data obtained on PSR0531 over three seasons of observations has given evidence for two modes of emission. The outbursts in 1981 demonstrate the existence of a sporadic component, while the data in 1982-1983 has clearly indicated the presence of steady, low-level, periodic emission.

The light curves obtained for the latter show a narrow peak

at the phase of the radio main pulse, with some evidence for emission at the same other phases as those suggested by lower energy measurements. As noted by Grindlay (Grindlay, 1982b) this suggests that there is close coupling between the VHE gamma ray and radio emission. In addition, because of the large absorption cross-section for TeV photons to pair produce, either on the pulsar magnetic field or in photon-photon scattering, they must arise from regions near the pulsar light cylinder, and this fact, together with the present results, indicates that the radio emission should also arise from this region. The broader pulses obtained for the transient emission indicate perhaps a different production mechanism. It is suggested that the existence of strong sporadic bursts of transient emission may account for the previous apparently discordant results.

CHAPTER 9.

FUTURE WORK.

The performance of the University of Durham facility at Dugway was improved continuously from its establishment in the Spring and Summer of 1981 until its closure in late 1984; at that time its sensitivity was arguably as great as that of any other experiment in the field. In excess of 1000 hours of data were obtained covering ten possible sources; the results from the two discussed in this thesis have been published along with results from Hercules X-1 (Dowthwaite *et al*, 1984b) and M31 (Dowthwaite *et al*, 1984c), while analysis of the others continues.

The ultimate performance of this observatory, however, was limited by the equipment available, in particular the reflectivities and foci of the mirrors. As discussed in Chapter 3, the focal length of these ex-searchlight mirrors is unsuitable for the requirements of this experiment, which made necessary their deployment in a Cassegrain formation. The extra reflection this involves, together with the often poor quality of the mirror surfaces and focus, results in loss of light.

Clearly what is required is a purpose built VHE gamma ray telescope, the only one to date being the 60 m^2 dish at the Smithsonian Astrophysical Observatory at Mount Hopkins. The development of a further such telescope is underway, and is described briefly in the following section.

9.1 The Second Generation VHE Gamma Ray Telescope.

The new telescope will have two flux collectors, each made up

of 49 small (60 cm diameter) circular mirrors, giving an effective area of ~18 m^2. The focal length of the composite mirrors will be 2.5 m, an appropriate value for efficient detection of gamma rays against the proton background.

The light detector will consist initially of a group of seven 3" PMTs mounted at the prime focus of each collector; it is hoped to increase this to nineteen PMTs per collector in the future. Each PMT has a field diameter of ~1.8°, giving a total field area of 12.6 square degrees for the initial arrangement, rising to ~50 square degrees for the full complement of nineteen PMTs.

The flux collectors are to be supported on an alt-azimuth mount similar to that used in the current experiment. The steering and pointing system, and data recording electronics will be of broadly similar specification to those in the current experiment, but using commercial instead of home-built electronics (LeCroy Instruments CAMAC modules) for improved serviceability.

9.1.1 The Improved Performance of the New Telescope.

The energy threshold of the new telescope is expected to be lower than the present ones (~300 GeV as opposed to >1000 GeV) owing to the ten-fold increase in collector area. The count rate per pair of PMTs (one in each reflector) in coincidence is expected to rise to ~200 counts $minute^{-1}$.

The new component mirrors have been tested both in the laboratory and at Dugway, and have better imaging properties than the searchlight reflectors, in addition to their more appropriate focal length as mentioned earlier. The worst of the four detectors in Dugway was re-mirrored using three matrices of these new

mirrors, with the result that the threshold dropped to ~800 GeV, and the S/N ratio was improved by almost 100% owing to the appropriate choice of aperture.

9.1.2 Modes of Operation.

There are at present two main modes of operation planned for the new telescope.

The first of these combines the best features of both DS and TR modes in the current experiment. The potential source will be tracked, and the on-axis PMTs will register the ON-source counts, while the surrounding off-axis PMTs will respond to off-source counts. Thus the background is measured without any time being spent off-source.

The second mode is as a survey instrument. In this case each pair of PMTs, one from each collector, monitoring the same part of sky acts as a separate telescope operating in the DS mode. With the full complement of nineteen PMTs, this has the effect of nineteen separate 2° aperture detectors viewing adjacent parts of the sky, giving simultaneous coverage of an area of ~50 square degrees.

9.1.3 Proposed Deployment.

The initial commissioning of the new instrument is currently being carried out at Durham; final deployment is planned for Narrabri, Australia in 1986.

9.2 Computer Simulations.

The computer simulations have proved very useful to both the Dugway experiment and that at Mount Hopkins. The following sections

give details of new work currently underway and plans for future calculations in connection with these experiments, and with the new telescope described in section 9.1.

9.2.1 The Dugway Array.

Since the gamma ray observatory at Dugway was shut down towards the end of 1984, priority for further calculations of the response of this type of detector has shifted to the new instrument. There are, however, some calculations remaining which would prove useful.

The first is the production of a full set (20) of 20° cascades to determine more reliably the behaviour of the array between 10° and 35° than was possible from the one average event so far obtained.

In addition, some higher energy cascades would be extremely valuable; a suitable energy would be 3000 GeV. It will only be possible to produce a small number of these owing to the limitations of available computer time mentioned earlier.

It may also prove useful to reanalyse the current database taking into account the differing sensitivities of the detectors in the real array. This will have a bearing on the performance of the array in terms of one, two, three and fourfold events.

9.2.2 The FWO Imaging Camera.

The simulations of the response of the FWO imaging camera have been useful in developing the analysis programmes for use on real data, and also in the mode of operation of the instrument. Initially the idea was to determine the direction of an incoming

gamma ray from the shape and density distribution of the recorded image. The simulations, if correct, indicate that since a particular image could be obtained from a whole range of different combinations of direction and distance of core impact from the telescope, this is unlikely to work in its proposed form.

Future work, already underway, includes the extension of the data set to include cascades at non-vertical injection angles, and repeating the work completed so far using a reduced PMT acceptance of 0.25° for greater resolution.

9.2.3 The New Instrument.

One important area for future work is the modification of the Dugway binning routines to simulate the response of the new instrument, particularly with regard to deciding precisely what aperture would be most effective, since this parameter is more readily adjustable than was the case previously, and a final value has not been selected. Given the lower threshold energy at which the new instrument is expected to operate, a greater number of relevant calculations should be possible since less computer time is required.

9.3 The Future of VHE Gamma Ray Astronomy Using the Atmospheric Cerenkov Technique.

The field of VHE gamma ray astronomy has expanded rapidly during the last five years, and observations are currently being made at some fifteen centres; these include the Fred Whipple Observatory in Arizona, the Crimean Observatory, the TIFR at Ootacamund, the University of Wisconsin, the observatory at

Potchefstroom, South Africa and the observatory in Hawaii. As the majority of these are in the Northern Hemisphere, the planned Southern Hemisphere deployment of the new Durham instrument will provide data on sources such as the Vela pulsar and Centaurus A which have had relatively little coverage so far.

APPENDIX A.

THE PACKAGE FOR ROUTINE DATA ANALYSIS.

A set of flow diagrams is provided in Figures A.1-A.3 to illustrate the logic of the program. The general overview is provided in Figure A.2 which is supplemented by Figures A.2a and A.2b.

A.1 Tape Handling.

The NUMAC system for tape handling is operated by system commands entered at the terminal. In this package all the necessary commands are formulated by the program; the user is expected to supply no more than the name of the tape, and the file number, and the program does the rest. This ensures that the correct tape control commands are issued and that there is no possibility of the stored data being corrupted; it is not possible to write to a tape mounted by the package even when the program has been terminated. Figure A.2b illustrates this aspect of the program.

A.2 Output File Handling.

In order to eliminate user errors, all output files are created by the program. To make this possible, a convention for naming files was clearly necessary.

The first stage in the routine data handling, the minute by minute binning, uses the data tape as source; thereafter disc files are used. The output from the minute by minute binning routine is stored on disc using names of the form 01.13; the first pair of digits refers to the tape from which the data was taken, in this

Start of Sequence

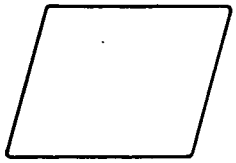

Input / Output

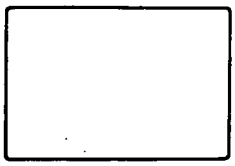

Processing

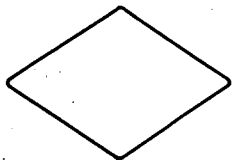

Program Decision

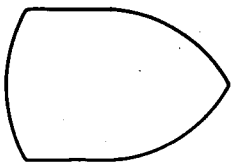

Display

Off-Page Connector

Figure A.1 Key to Flow Diagrams.

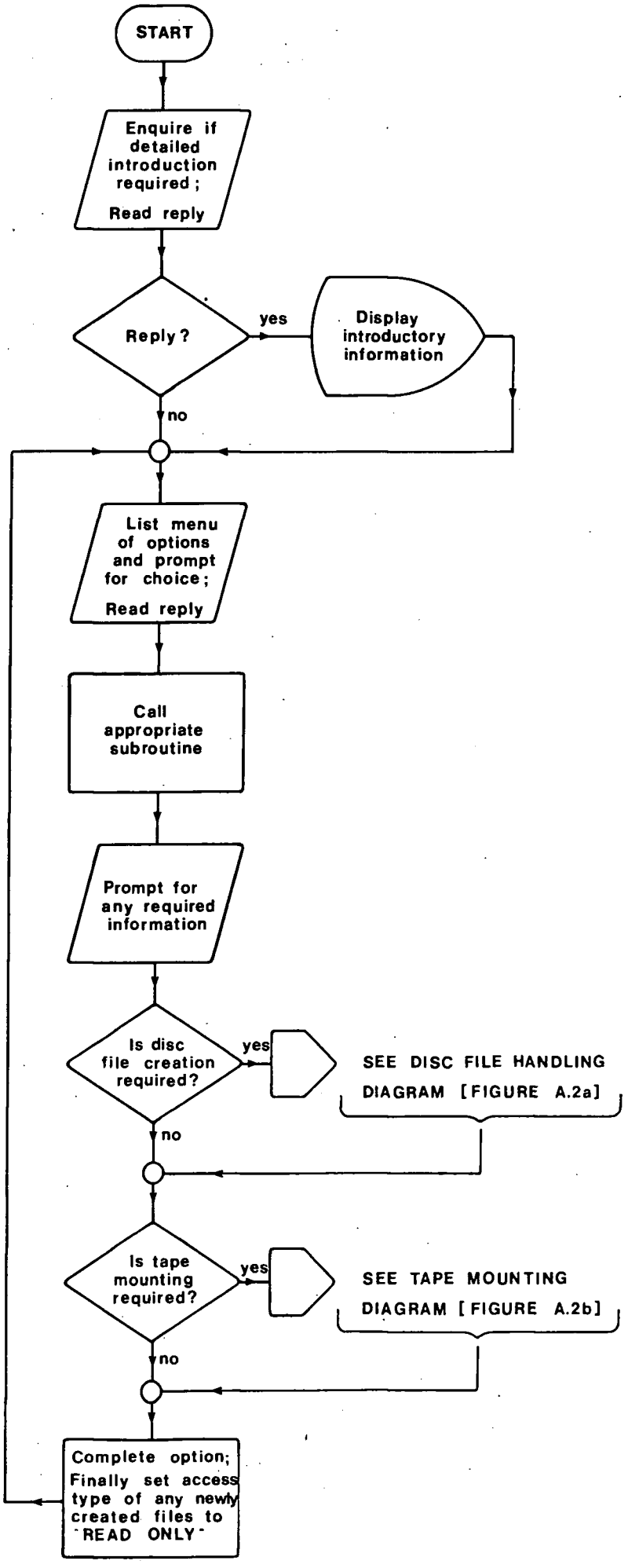

Figure A.2 General Overview of Program Logic.

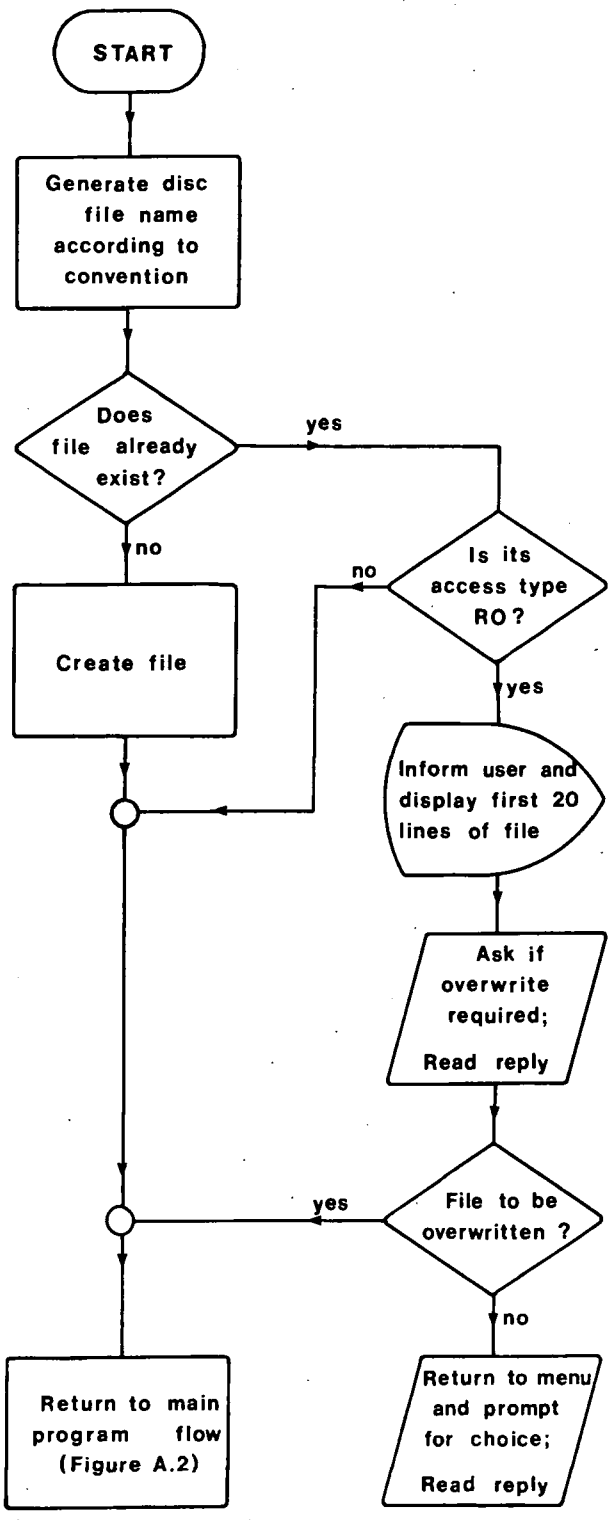

Figure A.2a Disc File Handling.

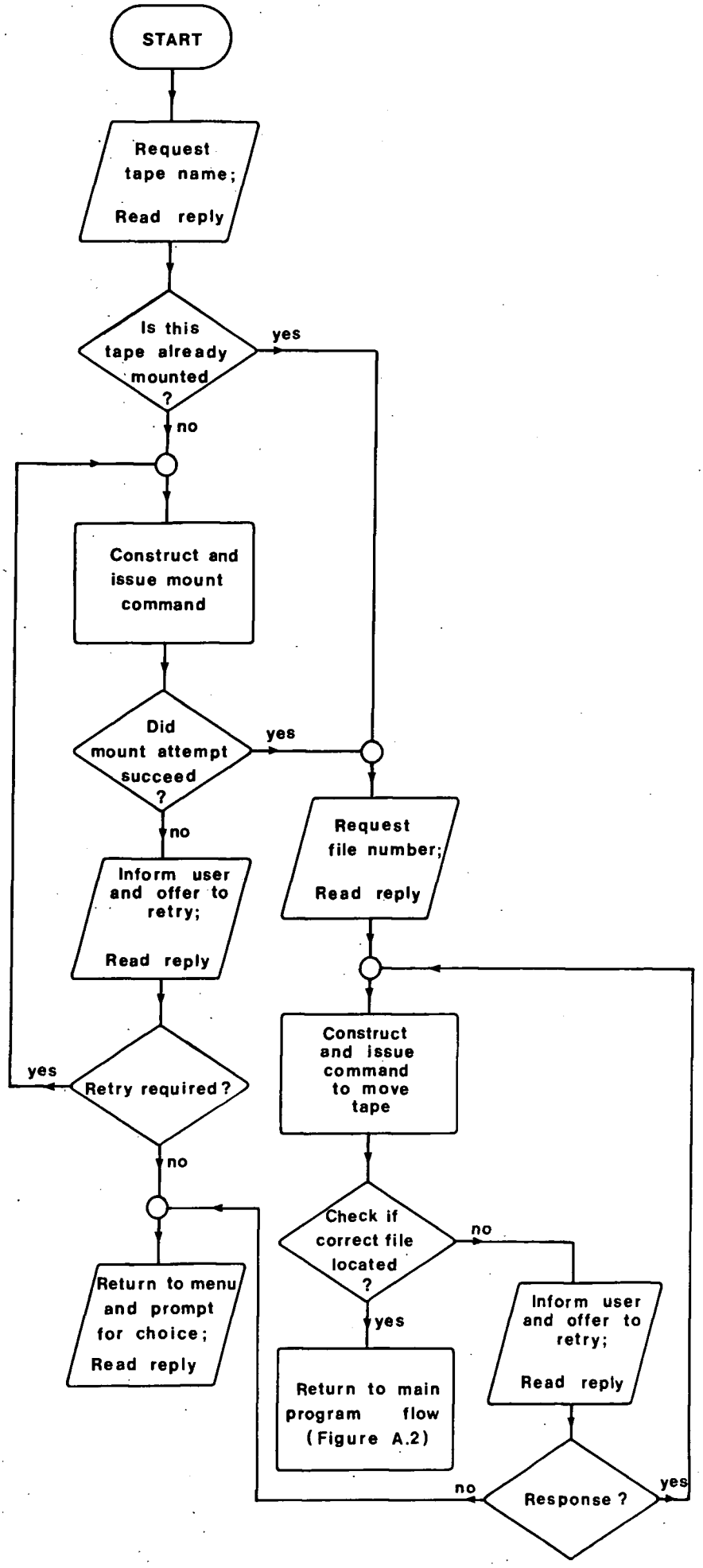

Figure A.2b Tape Mounting.

case it would be tape DUG001, while the second pair corresponds to the file number on that tape used for the analysis, in this example '13'.

Successive analysis routines, using file 01.13 as input, would have names such as S1001.13, the prefix S10 indicating that the file contained sliding average data using a 10-minute width. Prefixes of similar form are used for the other options.

When the program has finished writing to such a file it sends the appropriate MTS command to set its access type to READ ONLY (RO); this prevents the file being inadvertantly overwritten.

Once the program has generated the appropriate file name for output, before attempting to create the file it first checks to see if a file of that name already exists. If it does, and if its access type is RO, a warning is sent to the user to the effect that the analysis about to be embarked upon has probably already been done. The user may then look at the file in question and decide if he wishes to overwrite it. If the file exists but is not restricted to RO access, it means that the program was interrupted while writing to it on a previous occasion, and the analysis was therefore not completed, so no action is taken to prevent overwriting. The flow diagram provided in Figure A.2a illustrates the action of this section of the program.

A.3 The Facility for Extra Commands.

To make the package more versatile, a command structure was incorporated. The commands provided are CANCEL, MTS, QUIT, HELP, MENU, COMMANDS, MOUNT and DISMOUNT, which are explained below with the aid of flow diagrams (Figures A.4a and A.4b). These can be used

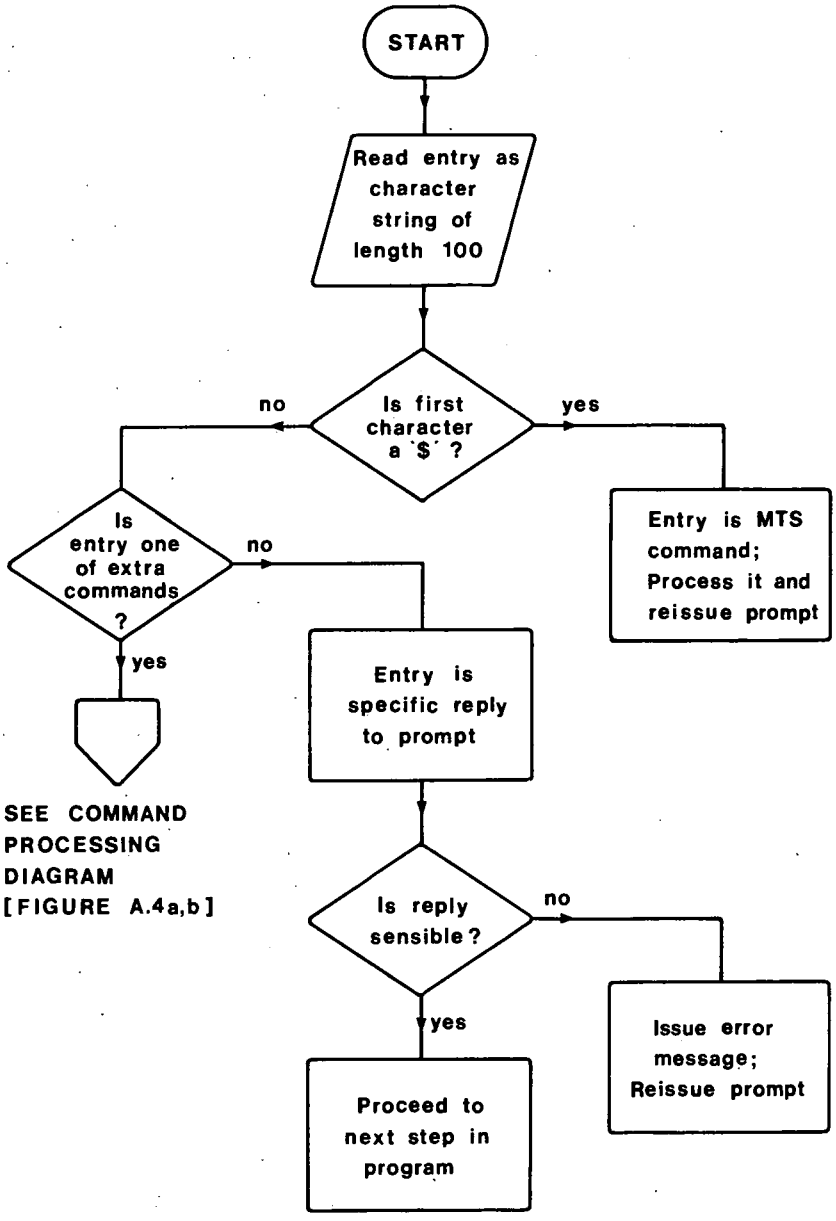

Figure A.3 Entry Processing.

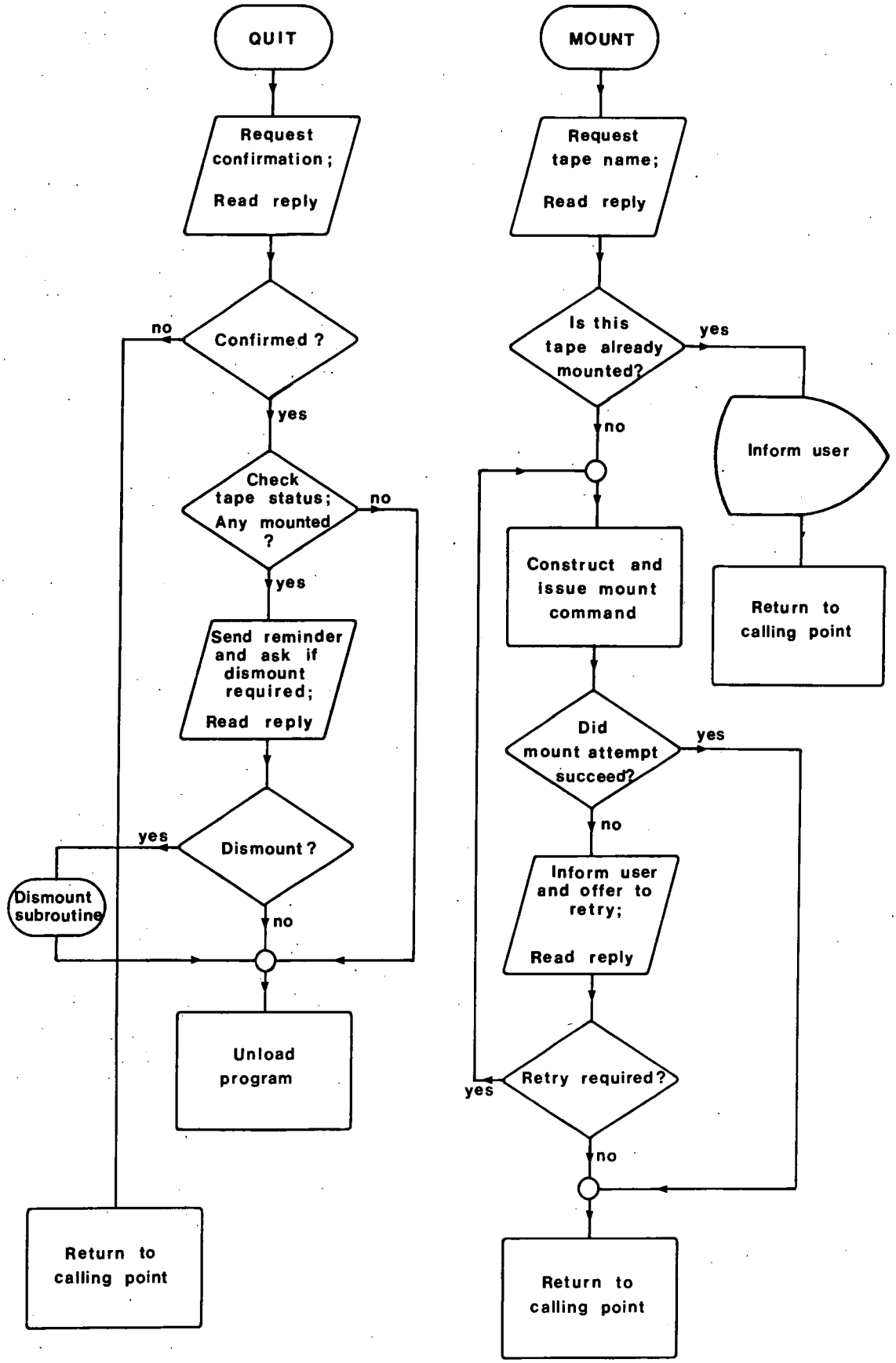

Figure A.4a Command Processing.

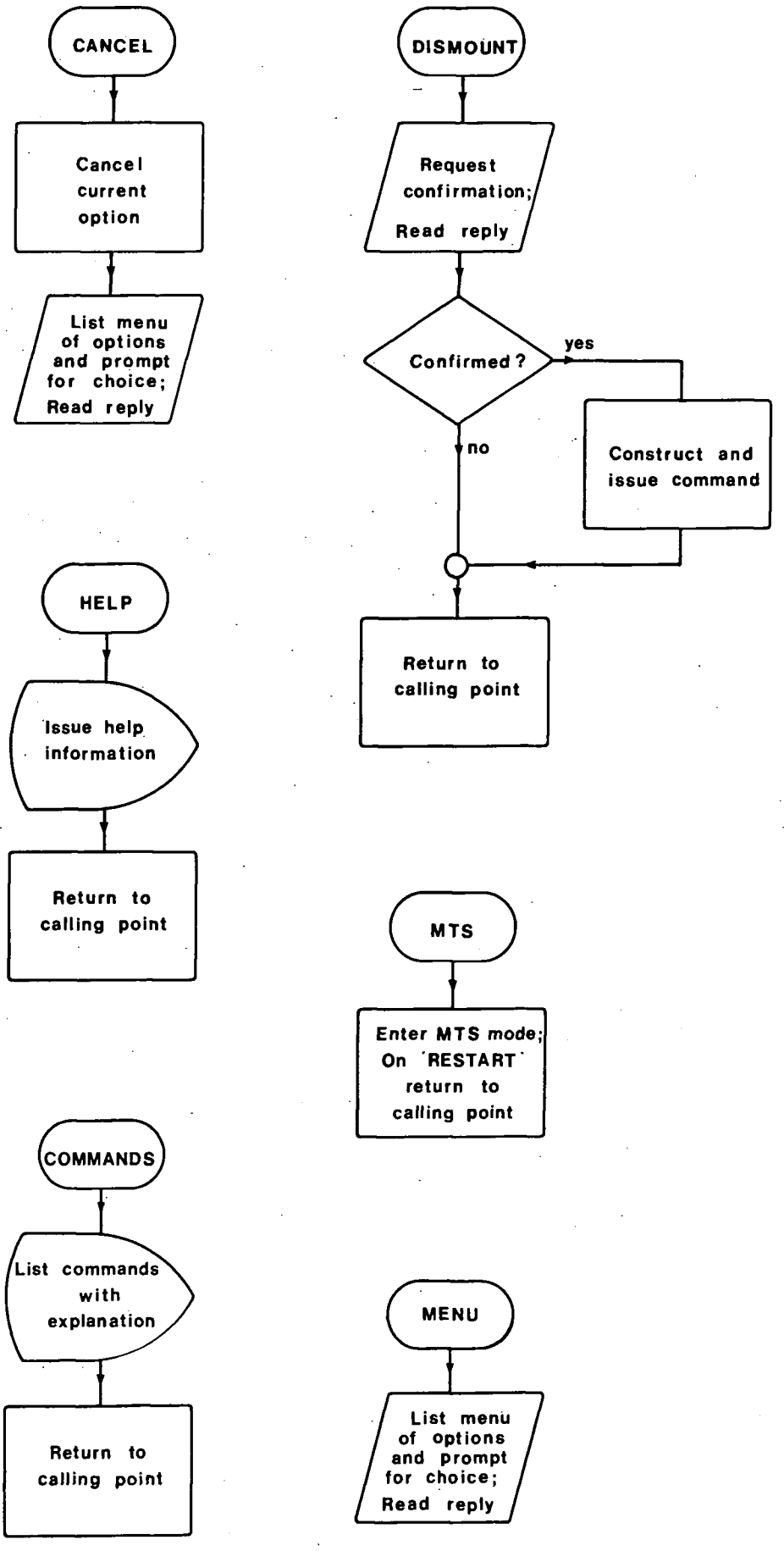

Figure A.4b Command Processing.

whenever the program is expecting input, signified in the flow diagrams by the boxes labelled (2) in Figure A.1. The sequence of operations carried out to process all such entries to the terminal is illustrated in Figure A.3.

1. CANCEL

This command is used to terminate a particular course of action and return to the menu. It may be used, for example, if the user, having selected a particular option, decides that one of the parameters the program has prompted for has been entered incorrectly.

2. MTS

This allows the user to leave the program temporarily (it remains loaded) and enter MTS mode (normal terminal mode), where normal commands may be issued. Entering RESTART returns control to the program.

Also, single MTS commands may be issued without leaving the program by prefixing them with $. As can be seen from Figure A.3 the program initially reads any entry to the terminal as a single character string and checks the first character before any other action is taken; if it is '$' the entire string is passed to the system as an MTS command. Control is then immediately returned to the program unless the action of the MTS command does not permit this.

3. QUIT

This command is issued to terminate the program. Before this happens, however, a check is made to see if the user currently has a tape mounted. If this is the case, a reminder is issued, and the

program offers to dismount the tape.

4. HELP

As the name implies, this provides assistance to the user who is unfamiliar with the program.

5. MENU

The action of this is similar to that of CANCEL in that the program is routed to the menu. It may be used when the program is initiated, for example, in order to circumvent the introductory section.

6. COMMANDS

This produces a list of the available commands, with explanation.

7. MOUNT

This allows the user to mount a tape without selecting one of the menu options. The tape is still mounted in such a way as to prevent the user from writing to it.

8. DISMOUNT

This is used to dismount tapes which have been mounted either by, or using, the program; tapes mounted independantly are ignored.

REFERENCES.

Batschelet E. (1981) Circular Statistics in Biology, Academic Press, London.

Blackett P.M.S. (1948) Emission Spectra of the Night Sky and Aurorae, Rep. Gassiot Committee of the Roy. Soc., Lond., 34.

Browning R. and Turver K.E. (1977) Nuovo Cimento, 38A, 223.

Catz Ph., Maze R., Gawin J., Przasnycki M., Wdowczyk J. and Zawadski A. (1970) Proc. 11th Int. Cosmic Ray Conference, Budapest, 3, 39.

Cerenkov P.A. (1934) Dokl. Akad. Nauk. SSSR, 2, 451.

Chudakov A.E., Dadykin V.L., Zatespin V.I. and Nesterova N.M. (1965) Trans. Consultants Bureau, 26, 99.

Chudakov A.E., Zatespin V.I., Nesterova N.M. and Dadykin V.L. (1962) J. Phys. Soc. Japan, Supplement A III, 106.

Cocconi G. (1954) Phys. Rev., 93, 646.

Danaher S., Fegan D.J., Porter N.A. and Weekes T.C. (1980) R. Soc. Discussion Meeting: Gamma Ray Astronomy (Phil. Trans. R. Soc. Lond., A301, 637).

Danaher S., Fegan D.J., Porter N.A. and Weekes T.C. (1981) Nature, 289, 568.

Dowthwaite J.C., Gibson A.I., Harrison A.B., Kirkman I.W., Lotts A.P., MacRae J.H., Orford K.J., Turver K.E. and Walmsley M. (1983) Astron. Astrophys., 126, 1.

Dowthwaite J.C., Harrison A.B., Kirkman I.W., MacRae J.H., McComb T.J., Orford K.J., Turver K.E. and Walmsley M. (1984a) Ap. J., 286, L35.

Dowthwaite J.C., Harrison A.B., Kirkman I.W., MacRae J.H., Orford K.J., Turver K.E. and Walmsley M. (1984b) Nature, 309, 691.

Dowthwaite J.C., Harrison A.B., Kirkman I.W., MacRae J.H., Orford K.J., Turver K.E. and Walmsley M (1984c) Astron. Astrophys., 136, L14.

Elsner R.F., Ghosh P., Darbro W., Weiskopf M.C., Sutherland P.G. and Grindlay J.E. (1980) Ap. J., 239, 335.

Eltermann L. (1968) Air Force Cambridge Res. Labs., ref: AFC RL-68-0153.

Erber T. (1966) Rev. Mod. Phys., 38, 626.

Erickson R.A., Fickle R.K. and Lamb R.C. (1976) Ap. J., 209, 592.

Fazio G.G. (1967) Ann. Rev. Astron. Astrophys., 5, 481.

Fegan D.J., McBreen B., O'Mongain E., Porter N.A. and Slevin P.J. (1968) Canad. Jour. Phys., 46, S433.

Frank I.M. and Tamm Ig. (1937) Dokl. Akad. Nauk. SSSR, 14(3), 109.

Fruin J.H., Jelley J.V., Long C.D., Porter N.A. and Weekes T.C. (1964) Phys. Rev. Lett., 10, 176.

Galbraith W. and Jelley J.V. (1953) Nature, 171, 349.

Galper A.M., Kirillov-Ugiriumov V.G., Kurochkin A.V., Leikov P.G., Luchkov B.I. and Yurkin Yu.T. (1976) Pisma v. Astron. Zh., 2, 524.

Gibson A.I., Harrison A.B., Kirkman I.W., Lotts A.P., MacRae J.H., Orford K.J. and Turver K.E. (1981) Proc. 17th Int. Conf. Cosmic Rays, 8, 38.

Gibson A.I., Harrison A.B., Kirkman I.W., Lotts A.P., MacRae J.H., Orford K.J., Turver K.E. and Walmsley M. (1982a) Proc. of Int. Workshop on VHE Gamma Ray Astron., TIFR, Bombay, 97.

Gibson A.I., Harrison A.B., Kirkman I.W., Lotts A.P., MacRae J.H., Orford K.J., Turver K.E. and Walmsley M. (1982b) Nature, 296, 833.

Gould R.J. and Schreder G.P. (1966) Phys. Rev. Lett., 16, 252.

Gregory P.C. (1972) Nature, 239, 439.

Greisen K. (1956) Prog. in Elementary Particles and Cosmic Ray Phys., North Holland, 3, 3.

Grindlay J.E. (1971) S.A.O., Special Report No. 334.

Grindlay J.E. (1982a) Proc. of Int. Workshop on VHE Gamma Ray Astron., TIFR, Bombay, 257.

Grindlay J.E. (1982b) Proc. of Int. Workshop on VHE Gamma Ray Astron., TIFR, Bombay, 178.

Grindlay J.E., Helmken H.F. and Weekes T.C. (1974) Proc. 9th Eslab Symposium, E.S.R.O., Frascati, 301.

Grindlay J.E., Helmken H.F. and Weekes T.C. (1976) Ap. J., 209, 592.

Grindlay J.E., Helmken H.F., Weekes T.C., Fazio G.G. and Boley F. (1973) Proc. 13th Int. Conf. Cosmic Rays, Denver, 1, 36.

Grindlay J.E., Helmken H.F., Hanbury Brown R., Davies J. and Allen L. (1975a) Ap. J. Lett., 197, L9.

Grindlay J.E., Helmken H.F., Hanbury Brown R., Davies J. and Allen L. (1975b) Ap. J., 201, 82.

Gupta S.K., Ramana Murthy P.V., Sreekantan B.V. and Tonwar S.C. (1977) Proc. 15th Int. Cosmic Ray Conf., Plovdiv, 1, 114.

Gupta S.K., Ramana Murthy P.V., Sreekantan B.V. and Tonwar S.C. (1978) Ap. J., 221, 268.

Hearn D.R. (1969) Nucl. Inst. and Meth., 70, 200.

Helmken H.F., Grindlay J.E. and Weekes T.C. (1975) Proc. 14th Int. Conf. Cosmic Rays, Munich, 1, 123.

Horowitz P., Papaliolios C. and Carelton N.P. (1972) Ap. J., 172, 151.

Jelley J.V. (1958) Cerenkov Radiation and its Applications, Pergammon Press, London.

Jelley J.V. (1966) Phys. Rev. Lett., 16, 479.

Jennings D.M., White G., Porter N.A., O'Mongain E., Fegan D.J. and White J. (1974) Nouvo Cimento, 20, 71.

Kniffen D.A., Fichtel C.E., Hartman R.C., Lamb R.C. and Thompson D.J. (1977) Recent Advances in Gamma Ray Astronomy, E.S.A. Frascati, 45.

Lamb R.C., Fichtel C.E., Hartman R.C., Kniffen D.A. and Thompson D.J. (1977) Ap. J., 212, L63.

Lamb R.C., Godfrey C.P., Wheaton W.A. and Tumer T. (1981) Nature, 296, 543.

Long C.D., McBreen B., Porter N.A. and Weekes T.C. (1965) Proc. 9th Int. Conf. Cosmic Rays, Lond., 1, 318.

Longair M.S. (1981) High Energy Astrophysics, Cambridge University Press, 56.

Mardia K.V. (1972) Statistics of Directional Data, Academic, New York.

Mason K.O., Becklin F.F., Blankenship L., Brown R.L., Elias T., Hjellming R.M., Mathews S.K., Murdin P.G., Neugebauer G., Sanford P.W. and Willner S.P. (1976) Ap. J., 207, 78.

McComb T.J.L. and Turver K.E. (1981) Proc. 17th Int. Conf. Cosmic Rays, Paris, 6, 130.

Milgrom M. (1976) Astron. Astrophys., 51, 215.

Milgrom M. and Pines D. (1978) Ap. J., 220, 272.

Molteni D., Rapisardi M., Robba N.R. and Scarsi L. (1980) Astron. Astrophys., 87, 88.

Mukanov J.B., Nesterova N.M., Stepanian A.A. and Fomin V.P. (1979) Proc. 16th Int. Cosmic Ray Conf., Kyoto, 1, 143.

Neshpor Yu.I., Stepanian A.A., Fomin V.P., Gerasimov S.A., Vladimirsky B.M. and Zyskin Yu.L. (1979) Astropys. Space Sci., 61, 349.

Neshpor Yu.I, Zyskin Yu.L., Mukanov J.B., Stepanian A.A. and Fomin V.P. (1980) R. Soc. Discussion Meeting: Gamma Ray Astronomy (Phil. Trans. R. Soc. Lond., A301, 633).

O'Mongain E. (1973) Nature, 241, 376.

Ogelman H., Ayasli S. and Hacinliyar A. (1976) Proc. Gamma Ray Symposium, Goddard, 118.

Porter N.A. (1973) Nuovo Cimento Lett., 8, 481.

Porter N.A., Delaney T., Helmken H.F. and Weekes T.C. (1976) Nuovo Cimento, 32B, 514.

Porter N.A., Delaney T. and Weekes T.C. (1974) Proc. 9th Eslab Symposium, E.S.R.O., Frascati, 295.

Porter N.A. and Weekes T.C. (1978) S.A.O. Spec. Rep. No. 381.

Protheroe R.J. and Turver K.E. (1979) Nuovo Cimento, 51A, 277.

Rieke G. (1969) Proc. 11th Int. Conf. Cosmic Rays, Budapest (Acta. Phys. Acad. Sci. Hung., 29, Suppl. 3, 601 (1970).).

Rossi B. and Greisen K. (1941) Rev. Mod. Phys., 13(4), 240.

Samorski M. and Stamm W. (1983) Ap. J. Lett., 268, L17.

Scarsi L., Bennet K., Bignami G.F., Boella G., Buccheri R., Hermsen W., Koch L., Mayer-Hasselwander H.A., Paul J.A., Pfefferman E., Stiglitz R., Swanenburg B.N., Taylor B.G. and Wills R.D. (1977) Recent Advances in Gamma Ray Astronomy, E.S.A., Frascati, 3.

Smith G.J. and Turver K.E. (1973) J. Phys. A, 6, L121.

Stecker F.W. (1971) Cosmic Gamma Rays, NASA, SP, 249.

Strong A.W. (1982) Proc. of Int Workshop on VHE Gamma Ray Astron., TIFR, Bombay, 141.

Tornabene H.S. and Cusimano F.J. (1968) Canad. J. Phys., 46, S581.

Toyoda Y., Suga K., Murikami K., Hasegawa H., Shibata S., Domingo V., Escobar I., Kamata K., Bradt H., Clark G. and LaPoint M. (1965) Proc. 9th Int. Conf. Cosmic Rays, London, 708.

Van der Klis M. and Bonnet-Bidaud J.M. (1981) Astron. Astrophys., 95, L5.

Vestrand W. and Eichler D. (1982) Ap. J., 251, 112.

Vladimirski B.M., Stapanian, A.A. and Fomin V.P. (1973). Proc. 13th Int. Conf. Cosmic Rays, Denver, 1, 456.

Weekes T.C. (1981) Proc. 17th Int. Conf. Cosmic Rays, 8, 34.

Weekes T.C. and Geary J.C. (1982) Publ. Astron. Soc. Pacific, 94, 708.

Weekes T.C. and Rieke G.H. (1974) Proc. 9th Eslab Symposium, E.S.R.O., Frascati, 287.

Weekes T.C. and Turver K.E. (1977) 12th Eslab Symposium, E.S.R.O., Frascati.

Wills R.D. (1981) Phil. Trans. R. Soc. A301, 537.

Wills R.D., Bennett K., Bignami G.F., Buccheri R., Caraveo P.A., Hermsen W., Kanbach G., Masnou J.L., Mayer-Hasselwander H.A., Paul J.A. and Sacco B. (1982) Nature, 296, 723.

ACKNOWLEDGEMENTS

I wish to thank Professor A.W. Wolfendale F.R.S. for provision of the facilities of the Physics Department of the University of Durham. I am also indebted to my supervisor, Dr. K.E. Turver, for his continual encouragement and advice.

I thank my colleagues John Dowthwaite, Ian Gibson, Andrew Harrison, Ian Kirkman, Alan Lotts, Lowry McComb, Keith Orford and Mark Walmsley for their company and many useful discussions.

I also wish to thank the staff of the Computing Unit of the University of Durham for the provision of computing facilities, and the University itself for the provision of a Research Studentship.